High-precision weak gravitational lensing predictions with the MillenniumTNG simulations

Fulvio Ferlito

München 2025

High-precision weak gravitational lensing predictions with the MillenniumTNG simulations

Fulvio Ferlito

Dissertation
an der Fakultät für Physik
der Ludwig–Maximilians–Universität
München

vorgelegt von
Fulvio Ferlito
aus Palermo, Italy

München, den 10.06.2025

Erstgutachter: Prof. Dr. Volker Springel
Zweitgutachter: Prof. Dr. Klaus Dolag
Tag der mündlichen Prüfung: 24.07.2025

Dedicated to my mom.

Contents

List of Figures

List of Tables

Zusammenfassung

Der Gravitationslinseneffekt, das heißt die Ablenkung des Lichts durch Masseninhomogenitäten entlang der Sichtlinie, hat sich zu einem wichtigen Werkzeug für die Untersuchung der Eigenschaften unseres Universums entwickelt. Im Bereich des so genannten "schwachen Gravitationslinseneffekts" führt dieses Phänomen zu leichten, kohärenten Verzerrungen der Bilder entfernter Galaxien und bietet eine leistungsstarke Methode zur Untersuchung der zugrunde liegenden gesamten Materieverteilung, unabhängig von ihrer leuchtenden Komponente.

Himmelsdurchmusterungen des schwachen Gravitationslinseneffekts, basierend etwa auf der *Hyper Suprime-Cam*, dem *Dark Energy Survey* und dem *Kilo-Degree Survey*, haben im letzten Jahrzehnt bereits wichtige Hinweise auf den Wert der kosmologischen Parameter, sowie Einblicke in die Natur der dunklen Materie und der dunklen Energie geliefert. Die kosmologischen Himmelsdurchmusterungen der nächsten Generation, wie *Euclid*, das *Large Synoptic Survey Telescope* oder *Roman* werden voraussichtlich hochpräzise Daten mit einer noch nie dagewesenen Himmelsabdeckung, Winkelauflösung und Rotverschiebungstiefe liefern. Daher besteht ein Bedarf an ebenso präzisen numerischen Vorhersagen.

Diese Arbeit stellt eine Reihe von umfassenden numerischen Experimenten vor, die auf dem MillenniumTNG (MTNG)-Projekt basieren, einem hoch modernen Satz von kosmologischen Simulationen, die das große Volumen der Millennium-Simulation mit dem realistischen, physikalisch motivierten Galaxienentstehungsmodell von IllustrisTNG kombinieren. Durch die Nutzung des reichhaltigen Datensatzes von MillenniumTNG zielt diese Arbeit darauf ab, die Auswirkungen einiger der wichtigsten physikalischen und numerischen Systematiken, die im Zusammenhang mit dem schwachen Gravitationslinseneffekt wichtig sind, zu quantifizieren und zu charakterisieren.

Im ersten Teil dieser Arbeit untersuche ich, wie sich die baryonische Physik und massenbehaftete Neutrinos auf die Beobachtungsdaten der schwachen Gravitationslinsen auswirken, indem ich Simulationen mit vollständiger Physik mit ihren Gegenstücken, die nur dunkle Materie berechnen, vergleiche. Außerdem evaluiere ich eine Varianzunterdrückungstechnik, die die Rechenkosten ohne Präzisionsverlust reduziert. Meine Ergebnisse bestätigen, dass sowohl Baryonen als auch Neutrinos einen signifikanten Einfluss auf die Gravitationslinsen-Statistiken haben, was die Notwendigkeit einer detaillierten physikalischen Modellierung in zukünftigen Bemühungen um Präzisionskosmologie unterstreicht. Diese Ergebnisse stimmen gut mit anderen führenden Simulationen überein, was die Robustheit der derzei-

tigen Modellierungsansätze unterstreicht.

Im dritten und letzten Teil der Arbeit befasse ich mich mit der intrinsischen Ausrichtung (IA) von Galaxien, einer wichtigen astrophysikalischen Verunreinigung von Messungen des schwachen Gravitationslinseneffekts. Unter Verwendung des nahtlosen Lichtkegels der hydrodynamischen Simulation von MTNG konstruiere ich einen realistischen Galaxienkatalog und berechne sowohl die intrinsische als auch die linseninduzierte Scherung für alle Galaxien. Dies ermöglicht eine detaillierte, nicht-lineare Bewertung der Auswirkungen von IA auf verschiedene Scherungsmessgrößen. Insbesondere untersuche ich, wie sich IA auf die gängigen Linsen-Statistiken auswirken kann, wobei ich mich auf die Abhängigkeit dieser Auswirkungen von der Rotverschiebung und der stellaren Masse der Galaxien konzentriere. Meine Erkenntnisse unterstreichen die Bedeutung einer präzisen IA-Modellierung für künftige Himmelsdurchmusterungen mit schwachen Gravitationslinsen und zeigen, dass dieser simulationsbasierte Ansatz die bisher genaueste und robusteste Modellierung von IA bietet.

Insgesamt trägt diese Arbeit zur Vorbereitung auf kosmologische Himmelsdurchmusterungen der nächsten Generation bei, indem sie hochpräzise simulationsbasierte Vorhersagen liefert, die kritische physikalische und numerische Systematiken berücksichtigen.

Abstract

Gravitational lensing, i.e. the deflection of light caused by mass inhomogeneities along the line of sight, has emerged as a key probe to investigate the properties of our Universe. In the weak regime, known as weak lensing (WL), this phenomenon leads to subtle coherent distortions in the shapes of distant galaxies, offering a powerful method to investigate the underlying total matter distribution, independent of its luminous component.

WL surveys of the previous decade like the Hyper Suprime-Cam, the Dark Energy Survey and the Kilo-Degree Survey have already yielded important constraints on the cosmological parameters as well as insights into the nature of dark matter and dark energy. Next generation cosmological surveys such as Euclid, the Large Synoptic Survey Telescope, and Roman, are expected to deliver high-precision lensing data featuring unprecedented sky coverage, angular resolution, and redshift depths. Consequently, the demand for equally precise numerical predictions has become essential.

This thesis presents a comprehensive set of numerical experiments based on the MillenniumTNG (MTNG) project, a state-of-the-art suite of cosmological simulations that combines the large volume of the Millennium Simulation with the high-fidelity physically-motivated galaxy formation model of IllustrisTNG. By leveraging the rich dataset produced by MillenniumTNG, this work aims to quantify and characterize the impact of some of the most relevant physical and numerical systematics inherent in popular weak lensing statistics.

In the first part of this thesis, I investigate how baryonic physics and massive neutrinos affect weak lensing observables by comparing full-physics simulations with their dark-matter-only counterparts. I also evaluate a variance suppression technique that reduces costs without a loss in precision. My findings confirm that both baryons and neutrinos have a significant impact on lensing statistics, underscoring the need for detailed physical modeling in upcoming precision cosmology efforts. These results align well with other leading simulations, supporting the robustness of current modeling approaches.

In the second part, I test the robustness of the Born approximation, a common approach used in numerical WL. To do so, I develop DORIAN, a full-sky ray-tracing code which features nonuniform fast Fourier transform, a novel interpolation technique that is both faster and more accurate than traditional approaches. By applying this code to the MillenniumTNG simulations, I investigate non-Gaussian effects that arise beyond the Born approximation. The resulting differences in lensing statistics are examined in detail,

providing guidance for when simplified modeling may or may not be adequate for precision cosmology.

In the third and final part of the thesis, I address the intrinsic alignment (IA) of galaxies, a key astrophysical contaminant in WL measurements. Using the seamless lightcone output from the MTNG hydrodynamical simulation, I construct a realistic mock galaxy catalogue and calculate both intrinsic and lensing-induced shear for all galaxies. This allows for a detailed, non-linear assessment of IA impacts on various shear observables. In particular, I study how IA can affect popular lensing statistics, focusing on the dependence of this impact on redshift and galaxy stellar mass. These insights highlight the importance of precise IA modeling for future weak lensing surveys, and demonstrate that this simulation-based approach offers the most accurate and robust modeling of IA to date.

Overall, this thesis contributes to the preparation for next-generation cosmological surveys by providing high-precision simulation-based predictions that account for critical physical and numerical systematics.

Chapter 1

Introduction

Cosmological observations show that the majority of the present-day energy density of the Universe is composed of two mysterious "dark" components, with $\approx 70\%$ made up of Dark Energy, modeled as a cosmological constant, and $\approx 25\%$ of Dark Matter; with only the remaining $\approx 5\%$ being ordinary (baryonic) matter. Understanding the physical nature of these two dark entities is one of the major challenges of modern cosmology. One valuable cosmological probe that can help us to shed light on the dark sector is weak gravitational lensing, whose upcoming generation of surveys will be characterised by unprecedented angular resolution and sky coverage. To fully exploit these rich and complex data far into the non-linear regime, it is crucial to provide high-fidelity numerical predictions. Throughout this Thesis, I will present my work: a series of weak lensing numerical experiments based on the MillenniumTNG simulations, a suite able to combine cosmological volume with state-of-the-art galaxy formation sub-grid modeling from IllustrisTNG. Such experiments aim at assessing, with high fidelity, the impact of a variety of factors on popular weak lensing statistics. These include physical systematics like the impact of baryons, the presence of massive neutrinos, and the intrinsic alignment of galaxies, as well as numerical aspects such as ray-tracing, angular resolution, mass resolution, and paired and fixed initial conditions.

The rest of this introductory chapter is organized as follows. In Section 1.1 I present an overview of the standard model of cosmology, from its assumptions and formalism up to its most recent tensions. In Section 1.2, I introduce the physical phenomenon of gravitational lensing, focusing on weak lensing and its employment as a powerful cosmological probe. Finally, in Section 1.3, I outline the primary motivations underlying this thesis and summarize the structure and content of the main body of work.

1.1 The standard model of cosmology

Cosmology is the branch of physics that studies the fundamental properties and large-scale evolution of the Universe. The foundation of modern cosmological theory lies in Einstein's General Relativity, which, in combination with the Cosmological Principle, naturally leads to the Friedmann equations. These equations describe how the Universe expands over time

as a function of its intrinsic curvature and its components, typically modeled as perfect fluids. In this chapter, I will introduce some essential cosmological quantities and concepts, as well as give an overview of the standard model of cosmology and some of its main critical points.

1.1.1 From basic principles to the Friedmann equations

A fundamental assumption on which standard cosmological theory relies states that:

The Universe is homogeneous and isotropic at sufficiently large scales.

This is known as *Cosmological Principle*, and is supported by a variety of observational evidence, with one of the most important being the Cosmic Microwave Background (CMB, Penzias & Wilson, 1965).

Another fundamental assumption is that at sufficiently large scales, the Universe is governed predominantly by gravity, which is described by General Relativity (GR, Einstein, 1915) as the manifestation of spacetime curvature. Requiring the Cosmological Principle to hold brings to a description of spacetime known as Friedmann–Lemaître–Robertson–Walker (FLRW) metric, which line-element is given by:

$$\mathrm{d}s^2 = a^2(t)\mathrm{d}\boldsymbol{x}^2 - c^2\mathrm{d}t^2. \tag{1.1}$$

Where c is the speed of light, $\boldsymbol{x} = (x_1, x_2, x_3)$ is a vector representing the three spatial dimensions, and $a(t)$ is the *scale factor*, a parameter with the dimension of length that encodes the expansion of the universe, conventionally normalized to $a_0 = 1$ at present time. Once the metric is defined, we want to obtain the dynamical equations of motion to describe the time evolution of $a(t)$, the only dynamical quantity appearing in the metric. To do so, we start by considering the Einstein equations, which, as can be shown, in the FLRW metric, assume the following form:

$$G_{\mu\nu} + \Lambda g_{\mu\nu} = \frac{8\pi G}{c^4} T_{\mu\nu}, \tag{1.2}$$

where

$$G_{\mu\nu} \equiv R_{\mu\nu} - \frac{1}{2} g_{\mu\nu} R. \tag{1.3}$$

Here, $G_{\mu\nu}$ is the Einstein tensor, $g_{\mu\nu}$ is the metric tensor, $R_{\mu\nu}$ and R the Ricci tensor and scalar respectively, and Λ is the cosmological constant. T^{μ}_{ν} is the energy-momentum tensor, which in the FLRW spacetime, T^{μ}_{ν} takes the perfect fluid form:

$$T^{\mu}_{\nu} = (\rho + P) u^{\mu} u_{\nu} + P \delta^{\mu}_{\nu}, \tag{1.4}$$

where ρ and P are the energy and pressure densities, $u^{\mu} = (-1, 0, 0, 0)$ is the four-velocity in comoving coordinates, and δ^{μ}_{ν} is the Kronecker delta. Finally, equations 1.1 and 1.2

can be combined together to give the desired cosmological dynamics equations, known as Friedmann equations:

$$H^2 = \frac{8\pi G}{3}\rho - \frac{Kc^2}{a^2} + \frac{\Lambda c^2}{3}, \tag{1.5}$$

$$\frac{\ddot{a}}{a} = -\frac{4\pi G}{3}(\rho + \frac{3P}{c^2}) + \frac{\Lambda c^2}{3}. \tag{1.6}$$

Here we have introduced the Hubble parameter $H \equiv \dot{a}/a$, describing the expansion rate of the Universe is expanding at a certain cosmic time; and K, the curvature constant, describing the intrinsic geometry of the Universe: $K = +1, -1, 0$ corresponds respectively to *closed*, *open* and *flat* geometries. In the above equations, the single and double dots represent the first and second time derivatives, respectively.

1.1.2 Components of the Universe

The homogeneous Universe under consideration consists of multiple components, each of which can be effectively treated as a perfect fluid characterized by its own equation of state:

$$w \equiv \frac{P}{\rho}. \tag{1.7}$$

To describe the dynamics of a Universe composed of multiple components, we must account for the individual contributions to the total energy density and pressure from each i-th component. In this case, the Friedmann equations take the following form:

$$H^2 = \frac{8\pi G}{3}\sum_i \rho_i - \frac{K}{a^2}, \tag{1.8}$$

$$\frac{\ddot{a}}{a} = -\frac{4\pi G}{3}\sum_i (\rho_i + 3P_i). \tag{1.9}$$

For ordinary matter, both pressure P and energy density ρ are strictly positive quantities, therefore, we expect the condition $w \geq 0$ to be satisfied. From statistical mechanics, one finds $w = 1/3$ for radiation and other relativistic species, and $w = 0$ for non-relativistic (cold) matter. Furthermore, it is interesting to note that the cosmological constant can be accounted for in the above equations as a fluid component with negative pressure and equation of state $w = -1$. In this context, the cosmological constant can be interpreted as a particular kind of *dark energy*, a family of exotic fluids characterized by $w < -1/3$. Finally, we introduce an important quantity associated with each species, the *dimensionless density parameter*, defined for a generic component I as:

$$\Omega_I \equiv \frac{8\pi G\rho_I}{3H^2} = \frac{\rho_I}{\rho_{\rm crit}}, \tag{1.10}$$

where $\rho_{\rm crit} = 3H^2/(8\pi G)$ is the so-called *critical density*.

1.1.3 The ΛCDM model and its tensions

In the past few decades, a concordance cosmological model known as Lambda-Cold Dark Matter (ΛCDM) has emerged as the standard framework for describing the large-scale structure and evolution of the Universe. As the name suggests, the two pillars of this model are the cosmological constant Λ, a form of dark energy which drives the accelerated expansion of the Universe, and cold dark matter (CDM), a form of non-relativistic matter that only interacts with gravity. As mentioned at the beginning of this chapter, Λ and CDM are the main constituents of the present-day Universe, making up respectively for $\approx 70\%$ and $\approx 25\%$ of its energy budget.

The ΛCDM model is supported by a wide range of observational evidence: among the earliest and most striking indicators for a non-zero cosmological constant were the luminosity-distance measurements of Type Ia supernovae, which revealed a late-time accelerated expansion of the Universe (Riess et al., 1998; Perlmutter et al., 1999). Complementary and independent confirmation of the ΛCDM model comes from the precise measurements of the temperature anisotropies in the CMB(Planck Collaboration et al., 2020), which not only corroborate the accelerated expansion but also point to the existence of CDM. Additional support for dark matter comes, amongst other things, from galactic rotation curves (Rubin et al., 1980), the dynamics of galaxy clusters (Zwicky, 1933), and weak gravitational lensing measurements (Clowe et al., 2006), all of which exhibit gravitational effects that cannot be explained by visible matter alone.

Despite its remarkable success in describing a wide range of cosmological observations, the ΛCDM model faces several challenges and open questions that have motivated continued theoretical and observational examination.

From a theoretical perspective, the cosmological constant gives rise to at least two main conceptual problems. The first is the *fine-tuning problem* (Weinberg, 1989), which stems from the discrepancy of 121 orders of magnitude between the observed value of Λ and the one predicted by quantum field theory. The second is the *coincidence problem*(see e.g., Dyson, 1998), which asks why the energy densities of matter and dark energy are of the same order of magnitude precisely today, given their significantly different time evolution.

On the observational side, tensions have emerged in recent years between high- and low-redshift cosmological probes. One of the most prominent among these is the so-called *Hubble tension*, a statistically significant discrepancy between the value of the Hubble constant H_0 inferred from the CMB observations assuming ΛCDM (Planck Collaboration et al., 2020), and the value obtained from local measurements using standard candles such as Cepheids and Type Ia supernovae (Riess et al., 2019, 2021). Current estimates place this tension at the $\sim 5\sigma$ level (Riess et al., 2022).

Another notable discrepancy is the so-called S_8 *tension*, which refers to differences in the measured amplitude of matter clustering. Specifically, weak lensing surveys tend to infer a lower clustering amplitude compared to that derived from CMB measurements under the assumption of the standard ΛCDM model. I will describe this tension in more detail in Section 1.2.3, after having introduced the phenomenon of weak gravitational lensing in the next section.

1.2 Weak gravitational lensing

After providing an overview of the standard cosmological model and its associated tensions, I now introduce the physical phenomenon of gravitational lensing, with an emphasis on weak lensing and its use as a powerful probe in modern cosmology.

1.2.1 Overview

As already intuited by Newton, light is deflected by the gravity of massive objects (Newton, 1704). However, it was not until the 1919 solar eclipse that the deflection of starlight by the Sun's gravitational field was observed, confirming predictions from Einstein's General Theory of Relativity (Dyson et al., 1920). These results, in addition to constituting a milestone in the acceptance of Einstein's theory of gravity over Newton's (Eddington, 1920), initiated a new branch of astrophysics: gravitational lensing. This term, probably popularized by Lodge (1919), encompasses a wide range of light deflection phenomena that can be mainly grouped into the following three families.

We have *strong lensing* when a massive object in the foreground produces multiple highly distorted or magnified images of a background source. It was theoretically considered by Einstein and Zwicky (Einstein, 1936; Zwicky, 1937a,b), who also recognized its potential for probing mass distributions and distant galaxies. The first observational evidence arrived with the discovery of multiply imaged quasars (Walsh et al., 1979; Weymann et al., 1980) and giant arcs in galaxy clusters (Lynds & Petrosian, 1986; Soucail et al., 1987).

We have *microlensing* when light deflection by compact objects, such as stars, planets, and black holes, causes magnification without image multiplicity. It was first detected through variability in lensed quasars (Irwin et al., 1989; Vanderriest et al., 1989). Among other remarkable applications, microlensing has constrained the dark matter content in galactic halos (Tisserand et al., 2007) and enabled the detection of exoplanets (Bond et al., 2004; Beaulieu et al., 2006), with many new of them being discovered in this way each year (Mroz & Poleski, 2023).

Last but not least, the vast majority of galaxy images we observe, are neither subject to strong lensing nor to microlensing, but experience a subtle and coherent shear due to the gravitational influence of the large-scale structure, an effect known as *weak lensing* (hereafter WL, for reviews see e.g., Bartelmann & Schneider, 2001; Hoekstra & Jain, 2008; Kilbinger, 2015; Mandelbaum, 2018; Prat & Bacon, 2025). Such effect, not easy to identify in individual images, can be statistically extracted from large ensembles of sources, offering a unique and powerful way to probe the mass distribution in the Universe (Kaiser, 1992). The first detection of WL came from observations around galaxy clusters (Tyson et al., 1990), followed by statistical measurements around galaxies (Brainerd et al., 1996) and finally the detection of lensing by the large-scale structure of the Universe (Bacon et al., 2000; Kaiser et al., 2000; Van Waerbeke et al., 2000).

1.2.2 Stage III surveys and popular statistics

Over the past two decades, WL has shown its potential in constraining cosmological parameters and for investigating the nature of the dark sector of the Universe. It has, in fact, become a standard probe in modern cosmology, especially with the advent of the so-called Stage-III surveys conducted in recent years, which include the Kilo-Degree Survey (KiDS, Hildebrandt et al., 2016; Heymans et al., 2021; Wright et al., 2024), the Dark Energy Survey (DES, Abbott et al., 2022; Bechtol et al., 2025), and the Hyper Suprime-Cam (HSC, Hikage et al., 2019; Aihara et al., 2022). These are characterised by a sky coverage of $\approx$ 4,143, 137, and 777 deg^2, and source galaxy number densities of $\approx$ 5.9, 17, and 6.2 arcmin^{-2}, respectively. Each of them thus occupies a distinct position in the trade-off between survey area and source density.

Among the current landscape of WL statistics, the most widely used is the so-called "3×2pt" statistic (see e.g., Abbott et al., 2018). This combines three two-point correlation functions: galaxy clustering, WL galaxy shear, and the galaxy-shear cross-correlation. Additionally, higher-order WL statistics have gained popularity and shown their efficacy for extracting complementary cosmological information. Some examples include: one-point PDF (Liu & Madhavacheril, 2019; Boyle et al., 2021), counts of peaks and/or minima (Martinet et al., 2018; Coulton et al., 2020; Davies et al., 2022; Marques et al., 2024), Minkowski functionals (Grewal et al., 2022), voids (Davies et al., 2021; Boschetti et al., 2023), bispectrum (Rizzato et al., 2019), trispectrum (Munshi et al., 2022), aperture mass statistic (Schmalzing & Gorski, 1998; Martinet et al., 2021), three-point correlation function (Takada & Jain, 2003), and integrated three-point correlation function (Halder et al., 2023).

1.2.3 Selected current WL constraints

Recent results from Stage-III WL surveys have converged on a consistent but rather puzzling picture. Each survey, using the 3×2pt or other statistics, has yielded tight constraints on the parameter $S_8 \equiv \sigma_8\sqrt{\Omega_m/0.3}$, which combines the root-mean-square fluctuation of the matter density field on $8h^{-1}$ Mpc scales (σ_8) and the total matter density parameter (Ω_m). For example, DES Year 3 data reports $S_8 = 0.776^{+0.017}_{-0.017}$ (Abbott et al., 2022), KiDS-1000 finds $S_8 = 0.766^{+0.020}_{-0.014}$ (Heymans et al., 2021), and HSC finds $S_8 = 0.775^{+0.043}_{-0.038}$ (Sugiyama et al., 2023). These results show remarkable internal consistency, despite the different survey strategies and analysis pipelines.

However, as already mentioned in Section 1.1.3, when compared to CMB constraints from Planck (Planck Collaboration et al., 2020), which report $S_8 = 0.834\pm0.016$, a mild but persistent discrepancy emerges. This so-called S_8 *tension* can be visualized in Figure 1.1, where cosmological constraints from the 3×2pt statistics of Stage-III WL surveys are shown together with the ones from Planck. As one can see, this tension is now observed at the $\sim$ 2–3σ level, depending on the exact datasets and combinations used. Several explanations have been proposed, including unaccounted-for systematics in either WL or CMB analyses, or indications of new physics such as modified gravity or evolving dark energy. While not

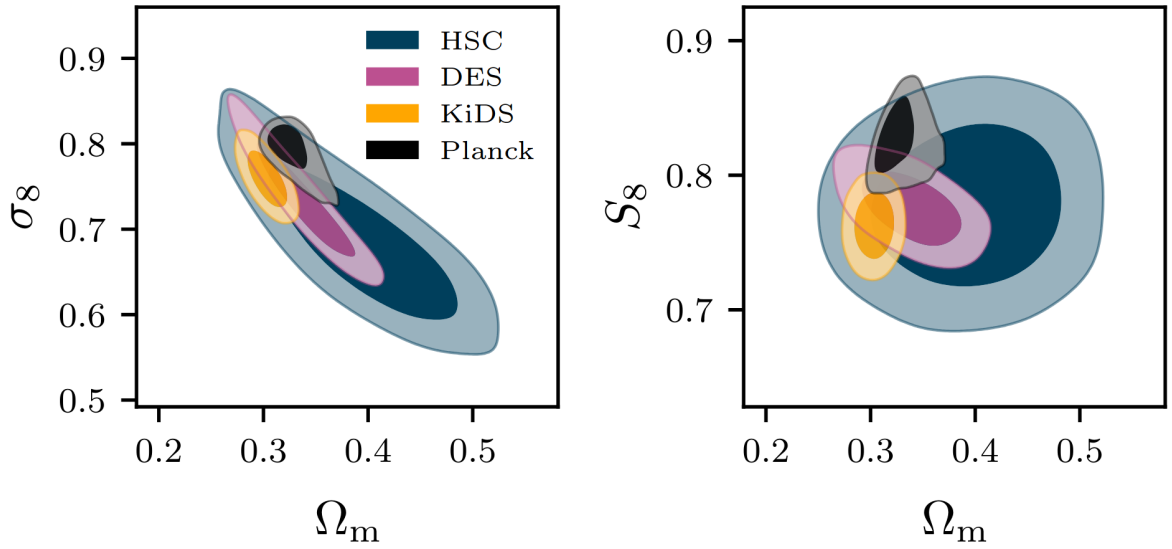

Figure 1.1: Cosmological constraints from the 3×2pt analyses of DES Y3 (Abbott et al., 2022), KiDS-1000 (Heymans et al., 2021), and HSC Y3 (Sugiyama et al., 2023), compared to early Universe measurements from the Planck satellite (Planck Collaboration et al., 2020), all within the framework of the ΛCDM model. This figure is taken from Prat & Bacon (2025).

yet definitive, this tension has become one of the key puzzles in contemporary cosmology and motivates both improvements in analysis and modeling, as well as the next generation of surveys.

1.2.4 Stage IV surveys

Looking ahead, Stage-IV surveys such as Euclid (Amendola et al., 2018; Euclid Collaboration et al., 2025) and LSST (LSST Science Collaboration et al., 2009), will feature a much bigger sky coverage of ≈ 15,000 and 18,000 deg^2, and increased source galaxy number densities of ≈ 30, and 37 arcmin^{-2}, respectively. This will significantly enhance the richness of WL datasets and promise more precise measurements. To fully exploit the scientific potential of present and future WL surveys, it is crucial to provide highly accurate theoretical predictions for the aforementioned statistics. This becomes increasingly challenging as observations probe the non-linear regime, where analytic frameworks break down and physical systematic uncertainties become significant. A non-exhaustive list of the main known physical systematics includes: uncertainties in baryonic physics (White, 2004; Jing et al., 2006), massive neutrinos (Kitching et al., 2008), source clustering (Bernardeau, 1998), and the intrinsic alignment of galaxies (Heavens et al., 2000).

1.2.5 Simulations

In this context, numerical simulations are the main tool for investigating the non-linear regime of WL, offering a powerful way to identify potential systematics in observations.

Motivated by this, several numerical methodologies for studying WL have been developed in the last decades. Among these are ray-tracing algorithms (e.g., Hilbert et al., 2009), production of full-sky maps (e.g., Fabbian et al., 2018; Hadzhiyska et al., 2023), on-the-fly computation (e.g., Barreira et al., 2016), and Hamiltonian-based algorithms (Zhou et al., 2024). Numerical codes implementing some of these approaches have been compared in Hilbert et al. (2020), which found them to produce consistent results provided certain resolution requirements are met.

Irrespective of the specific algorithm, upcoming observations will require WL simulations with very high angular resolution that go beyond modeling based on CDM and purely gravitational interactions alone. This is why there is now increasing interest in WL predictions from high-fidelity cosmological simulations that include galaxy formation and additional components. Some recent studies along these lines include Osato et al. (2021), Coulton et al. (2020), and Gouin et al. (2019), which focus on the impact of baryonic physics; Fong et al. (2019) and Liu et al. (2018), who study the impact of massive neutrinos; and Lee et al. (2025), who investigates the impact of the intrinsic alignment of galaxies. Their results suggest that all of these physical systematics must be included when interpreting data from upcoming stage-IV surveys.

1.3 This Thesis

In this thesis, making use of the MTNG suite of cosmological galaxy formation simulations, introduced in Section 3.2.1, I perform state-of-the-art numerical experiments to investigate some of the main criticalities and systematics of WL as a high-precision cosmological probe. This thesis is organized as follows. In Chapter 2, I provide fundamentals of weak lensing formalism and an overview of its measurement from observations. In Chapter 3, I focus on the impact of physical systematics like baryonic physics and massive neutrinos, as well as more technical aspects of WL simulations like angular resolution, mass resolution, and the employment of paired and fixed initial conditions. In Chapter 4, I develop a novel ray-tracing code for WL simulations, and make use of such code to investigate the impact of the Born approximation versus ray-tracing in WL simulations. In Chapter 5, I produce a mock galaxy catalogue starting from the lightcone particle output of MTNG, and use it in combination with my ray-tracing code to study the impact of the intrinsic alignment of galaxies on WL. Finally, in Chapter 6, I summarize the results of this thesis and present future prospects.

Chapter 2

Weak lensing formalism and methods

In this chapter, I present the mathematical formalism of weak lensing, as well as an overview of its practical measurement from observations.

2.1 Weak lensing theory

In this section, I outline the fundamentals of the WL formalism and then focus on the Born approximation and higher-order corrections.

2.1.1 Fundamentals

Let us assume a FRLW universe, introduced in Section 1.1.1. In the presence of weak scalar inhomogeneous perturbations expressed in terms of the Newtonian gravitational potential Φ, and the absence of anisotropic stress, the two Bardeen potentials are equal. Under these conditions, equation 1.1 assumes the following form:

$$\mathrm{d}s^2 = -\left(1+\frac{2\Phi}{c^2}\right)c^2\mathrm{d}t^2 + a^2(t)\left(1-\frac{2\Phi}{c^2}\right)\mathrm{d}\boldsymbol{x}^2\,. \tag{2.1}$$

We now introduce the lens equation from geometric optics which, as schematized in Figure 2.1, relates the observed angular position $\boldsymbol{\theta}$ to the true angular position $\boldsymbol{\beta}$ of a ray of light that, encountering a lens (or a system of lenses), is deflected by an angle $\boldsymbol{\alpha}$:

$$\boldsymbol{\beta} = \boldsymbol{\theta} - \boldsymbol{\alpha}\,. \tag{2.2}$$

In the context of gravitational lensing, matter acts as a lens, thus leading to the gravitational lens equation, which tells us that the observed position of a light ray starting from redshift z_s will depend on the surrounding matter field during its travel to the observer. Starting from equation 2.1, the deflection angle can be computed and written explicitly:

$$\boldsymbol{\beta}(\boldsymbol{\theta}, z_\mathrm{s}) = \boldsymbol{\theta} - \frac{2}{\mathrm{c}^2}\int_0^{\chi_\mathrm{s}} \mathrm{d}\chi_\mathrm{d}\frac{f_\mathrm{ds}}{f_\mathrm{d}f_\mathrm{s}}\nabla_{\boldsymbol{\beta}}\Phi(\boldsymbol{\beta}(\boldsymbol{\theta},\chi_\mathrm{d}),\chi_\mathrm{d},z_\mathrm{d})\,, \tag{2.3}$$

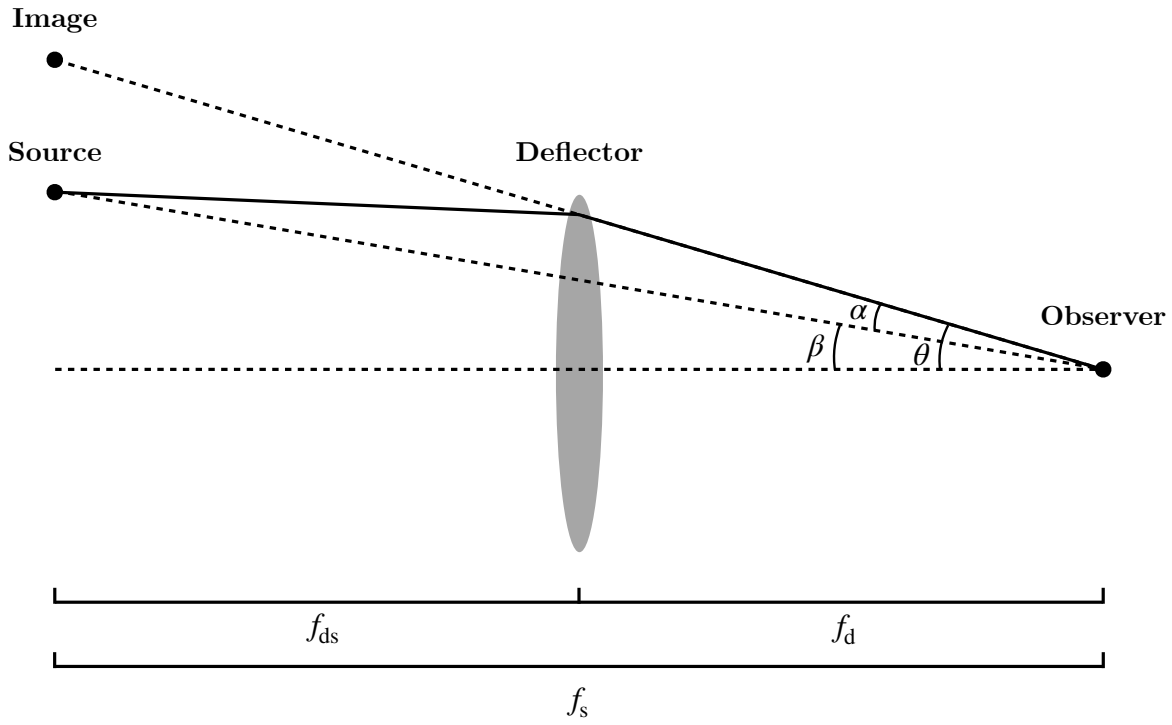

Figure 2.1: Schematic representation of a gravitational lens system. As described by equation 2.2, $\boldsymbol{\beta}$, the angular position of the source, is given by $\boldsymbol{\theta}$, its image angular position, subtracted by $\boldsymbol{\alpha}$, the deflection angle.

where we have introduced the angular gradient $\nabla_{\boldsymbol{\beta}}$, the comoving line-of-sight distance χ, and the comoving angular diameter distance $f_K(\chi)$. The subscripts "s" and "d" refer, respectively, to the source and the deflector (i.e. the lens); hence the geometric factors are $f_{\rm ds} = f_K(\chi_{\rm s} - \chi_{\rm d})$, $f_{\rm d} = f_K(\chi_{\rm d})$ and $f_{\rm s} = f_K(\chi_{\rm s})$. The distortion of an image, formed by the ray at $\boldsymbol{\theta}$ and the ones nearby, can be described by the distortion matrix A, obtained by differentiating the previous equation with respect to $\boldsymbol{\theta}$:

$$A_{ij} \equiv \frac{\partial \beta_i(\boldsymbol{\theta}, z_{\rm s})}{\partial \theta_j} = \delta_{ij} - \frac{2}{\mathrm{c}^2} \int_0^{\chi_{\rm s}} \mathrm{d}\chi_{\rm d} \frac{f_{\rm ds}}{f_{\rm d} f_{\rm s}} \times \frac{\partial^2 \Phi(\boldsymbol{\beta}(\boldsymbol{\theta}, \chi_{\rm d}), \chi_{\rm d})}{\partial \beta_i \partial \beta_k} \frac{\partial \beta_k \boldsymbol{\beta}(\boldsymbol{\theta}, \chi_{\rm d})}{\partial \theta_j} \,, \tag{2.4}$$

where δ_{ij} is the Kronecker delta. This matrix can be decomposed as follows:

$$A \equiv \begin{pmatrix} 1 - \kappa - \gamma_1 & -\gamma_2 - \omega \\ -\gamma_2 + \omega & 1 - \kappa + \gamma_1 \end{pmatrix} \,, \tag{2.5}$$

where we have introduced three fundamental WL quantities. The convergence, κ, is a scalar that measures the isotropic lensing distortion, which corresponds to a uniform scaling of the image, as shown in the left column of Figure 2.2. The rotation, ω, is a scalar that expresses the rigid rotation of the image about its center. It can be shown that, in the context of WL, one can typically assume $\omega \approx 0$. The shear, $\gamma = \gamma_1 + \mathrm{i}\gamma_2$, is a spin-2

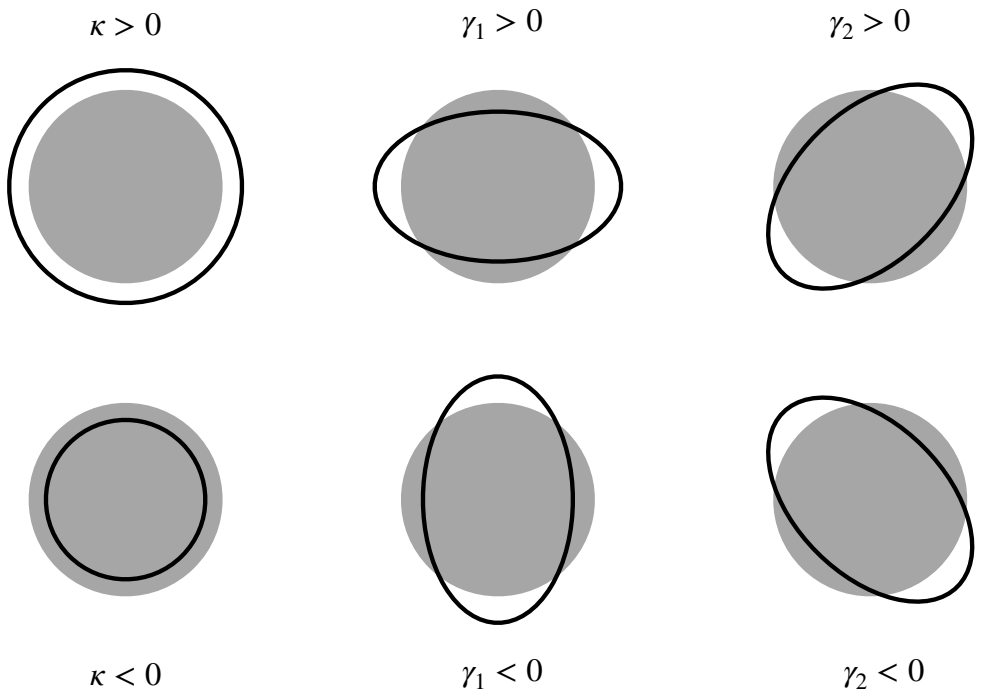

Figure 2.2: Qualitative visualization of the effect of the distortion matrix components, convergence κ and shear $\gamma = \gamma_1 + \mathrm{i}\gamma_2$, on the image of a background object that is intrinsically circular.

quantity that describes the anisotropic deformation of the source, which corresponds to elongation in a specific direction, as dictated by the individual components γ_1 and γ_2, shown in the center and right columns of Figure 2.2 respectively. Throughout this work, when considering the shear field on the celestial sphere, we adopt the convention that γ_1 corresponds to east-west elongation and γ_2 corresponds to northeast-southwest elongation.

2.1.2 The Born approximation

A common way to approach the integral in equation (2.4), known as the Born approximation, consists of integrating along an unperturbed straight light path; i.e., directly over θ instead of β. This significantly simplifies the equation, leading to:

$$\frac{\partial \beta_i(\boldsymbol{\theta}, z_\mathrm{s})}{\partial \theta_j} = \delta_{ij} - \frac{2}{\mathrm{c}^2} \int_0^{\chi_\mathrm{s}} \mathrm{d}\chi_\mathrm{d} \frac{f_\mathrm{ds}}{f_\mathrm{d} f_\mathrm{s}} \frac{\partial^2 \Phi(\boldsymbol{\theta}, \chi_\mathrm{d})}{\partial \theta_i \partial \theta_j} \,. \tag{2.6}$$

We can now make use of the Poisson equation for the gravitational potential Φ and neglect boundary terms at the observer and source positions to obtain the following expression for the convergence:

$$\kappa_\mathrm{born}(\boldsymbol{\theta}, z_\mathrm{s}) = \int_0^{\chi_\mathrm{s}} \mathrm{d}\chi_\mathrm{d}\, q_\mathrm{ds}\, \delta_\mathrm{m}(\boldsymbol{\theta}, \chi_\mathrm{d}, z_\mathrm{d}) \,, \tag{2.7}$$

where $\delta_{\rm m}$ is the density contrast and we introduced the lensing efficiency factor $q_{\rm ds}$, defined as:

$$q_{\rm ds} = \frac{3H_0^2\Omega_m}{2{\rm c}^2}(1+z_{\rm d})f_{\rm d}\frac{f_{\rm ds}}{f_{\rm s}}\,. \tag{2.8}$$

By assuming statistical isotropy and applying a Limber-type approximation (Limber, 1953; LoVerde & Afshordi, 2008), one can furthermore obtain an equation that connects the angular power spectrum of the convergence $C_\kappa(\ell)$ to the three-dimensional matter power spectrum $P_{\rm m}$ (see, e.g., Hilbert et al., 2020, for the complete derivation):

$$C_\kappa(\ell) = \int_0^{\chi_{\rm lim}} {\rm d}\chi \frac{q_{\rm ds}^2}{f_{\rm d}^2} P_{\rm m}(\ell/\chi_{\rm d}, z_{\rm d})\,. \tag{2.9}$$

where $P_{\rm m}(\ell/\chi_{\rm d}, z_{\rm d})$ is the matter power spectrum evaluated at redshift $z_{\rm d}$ and wave number $k = \ell/\chi_{\rm d}$. This last equation shows how the convergence power spectrum mixes different 3D k-modes into 2D ℓ-modes through line-of-sight integration. It is possible to show that with the approximations made so far, the angular power spectra of the shear (E and B modes), convergence, and rotation are related as follows:

$$C_\gamma^{\rm (EE)}(\ell) = C_\kappa(\ell)\,, \tag{2.10a}$$

$$C_\gamma^{\rm (BB)}(\ell) = C_\omega(\ell) = 0\,. \tag{2.10b}$$

2.1.3 Post-Born corrections

The Born approximation is obtained by expanding equation (2.4) to linear order in terms of Φ. By expanding to the quadratic order, one would obtain the following two additional terms:

$$\kappa = \kappa_{\rm born} + \kappa_{\rm ll} + \kappa_{\rm geo} + O(\Phi^3). \tag{2.11}$$

We refer the reader to equations (9) and (10) of Petri et al. (2017) for the explicit expressions of $\kappa_{\rm ll}$ and $\kappa_{\rm geo}$, respectively. In the following, we briefly describe the physical meaning of these two terms. The first post-Born term, $\kappa_{\rm ll}$, accounts for non–local couplings between lenses at the quadratic level; in other words, it considers that light is not perturbed independently by the series of deflectors along the line of sight, but rather that the deformation from background lenses is progressively distorted by the foreground lenses. This term is the lowest-order one to introduce a non-zero rotation. The second post-Born term, $\kappa_{\rm geo}$, accounts for the actual bending of light rays by integrating the matter density contrast along the corrected path at the lowest order in the geodesic deflections, as opposed to a straight trajectory. For this reason, it is sometimes called the *Born correction* (see e.g., Cooray & Hu, 2002).

2.2 Weak lensing measurements from observations

In practice, extracting the WL signal from observational data introduces a number of additional challenges. As mentioned in Chapter 1, WL refers to the coherent distortions

in the shapes of distant galaxies. These distortions are typically subtle, with the values of κ and γ being of the order of a few percent or less, and therefore can only be detected statistically by averaging over large ensembles of galaxies. Moreover, it is important to note that WL observations do not directly measure the shear γ, but rather the *reduced shear* g, defined as:

$$g = \frac{\gamma}{1-\kappa}\,. \tag{2.12}$$

This is because galaxy shape measurements are sensitive to anisotropic distortions introduced by shear, but insensitive to the isotropic magnification caused by convergence. In the WL regime, where $\kappa \ll 1$ and $|\gamma| \ll 1$, the reduced shear approximates the true shear well, i.e., $g \approx \gamma$ (see e.g. Section 4.2 of Bartelmann & Schneider, 2001). Throughout this work, I adopt this approximation, following the common approach in most theoretical and numerical WL studies.

As I will discuss in more detail in Chapter 5, the observed shear of a galaxy is influenced both by its intrinsic shape and by the lensing-induced shear. Assuming random intrinsic orientations, the average ellipticity in a region of the sky provides an unbiased estimate of the local shear field. To extract this signal, several steps are involved, including: point-spread function correction (see e.g., Paulin-Henriksson et al., 2009; Rowe, 2010; Liaudat et al., 2023; Schutt et al., 2025); shape measurement via algorithms such as `lensfit` (Miller et al., 2007), `IM3SHAPE` (Zuntz et al., 2014), or `METACALIBRATION` (Huff & Mandelbaum, 2017); and redshift estimation via photometric or spectroscopic techniques (see e.g., Mandelbaum et al., 2008; Cai & Bernstein, 2012; Hildebrandt et al., 2021; Tanaka et al., 2018). Errors and systematics at any stage of the measurement pipeline can introduce biases in the inferred shear and therefore must be carefully accounted for. This complexity highlights the essential role of accurate numerical simulations, not only for interpreting the WL signal but also for validating and calibrating the entire measurement process.

Chapter 3

The impact of baryons and massive neutrinos on high-resolution weak gravitational lensing convergence maps

The content of this chapter has been published in the Monthly Notices of the Royal Astronomical Society, Volume 524, Issue 4, October 2023, Pages 5591–5606, and reported here with slight modifications.

Abstract

We study weak gravitational lensing convergence maps produced from the MillenniumTNG (MTNG) simulations by direct projection of the mass distribution on the past backwards lightcone of a fiducial observer. We explore the lensing maps over a large dynamic range in simulation mass and angular resolution, allowing us to establish a clear assessment of numerical convergence. By comparing full physics hydrodynamical simulations with corresponding dark-matter-only runs we quantify the impact of baryonic physics on the most important weak lensing statistics. Likewise, we predict the impact of massive neutrinos reliably far into the non-linear regime. We also demonstrate that the "fixed & paired" variance suppression technique increases the statistical robustness of the simulation predictions on large scales not only for time slices but also for continuously output lightcone data. We find that both baryonic and neutrino effects substantially impact weak lensing shear measurements, with the latter dominating over the former on large angular scales. Thus, *both* effects must explicitly be included to obtain sufficiently accurate predictions for stage IV lensing surveys. Reassuringly, our results agree accurately with other simulation results where available, supporting the promise of simulation modeling for precision cosmology far into the non-linear regime.

3.1 Introduction

In this chapter, we introduce our Born-approximation-based method for computing high-resolution full-sky WL convergence maps, starting from the mass-shell outputs produced by our simulation set; we also present a way of efficiently partitioning a full-sky map into smaller square patches, which is based on the Fibonacci sphere distribution. We apply our WL machinery to the MillenniumTNG (MTNG) state-of-the-art simulation suite to study the impact of baryonic physics, massive neutrinos, and angular resolution. We also test how the use of fixed and paired initial conditions (see Angulo & Pontzen, 2016) can improve the statistical robustness of WL simulations obtained from simulation boxes of limited size. The observables considered in this study are the angular power spectrum of the WL convergence, its one-point probability distribution function (PDF), and peaks and minima counts in the corresponding maps.

This study is part of the introductory paper set of the MTNG project. In Hernández-Aguayo et al. (2022), the technical aspects of the simulations are introduced together with a high-level analysis of matter and halo statistics. Pakmor et al. (2022) provides more details of the hydrodynamical simulations, focusing, in particular, on the galaxy cluster population. Barrera et al. (2022) presents an updated version of the L-Galaxies semi-analytic modeling code and applies it to obtain lightcone output for the dark-matter-only simulations. Hadzhiyska et al. (2022b,a) present improved halo occupation distribution models for the halo–galaxy connection, focusing on the one-halo and two-halo terms, respectively. Bose et al. (2022) analyzes galaxy clustering, in particular, as a function of the colour selection. Delgado et al. (2023) investigates the intrinsic alignment of galaxy shapes and large-scale structure, and how it is affected by baryonic physics. Kannan et al. (2022) study the properties of the predicted galaxy population at $z > 8$ in the full-hydro run. Finally, Contreras et al. (2022) shows how the cosmological parameters of MTNG can be recovered from mock SDSS-like galaxy samples, using an extended subhalo abundance matching technique combined with a fast-forward prediction model.

This chapter is organized as follows. In Section 3.2 we describe the methods we use to compute our WL maps and the associated observables. In particular, we describe the "mass-shell" outputs of the MTNG simulations (Sec. 3.2.2) and how these are used in our code to produce WL convergence maps (Sec. 3.2.3). We then introduce our method for partitioning a full-sky map efficiently into square patches via the Fibonacci sphere distribution (Sec. 3.2.4), and we briefly describe how the observables are extracted from the maps (Sec. 3.2.5). In Section 3.3, we begin by comparing results from maps with different angular resolution (Sec. 3.3.1). We then show the impact of baryonic effects (Sec. 3.3.2) and massive neutrinos (Sec. 3.3.3) on WL statistics. Lastly, we study the extent to which the use of fixed and paired initial conditions improves statistical robustness (Sec. 3.3.4). In Section 3.4, we compare our findings on the impact of baryons and massive neutrinos to results from similar recent studies. In Section 3.5, we summarise our findings, concluding that WL lensing simulations aimed to inform stage-IV surveys must have high angular resolution and correctly model both baryonic and neutrino effects. In Appendix A, we show how different smoothing scales vary our results on the impact of resolution.

Table 3.1: Specifications of the simulations of the MillenniumTNG project used in this thesis.

Type	Run name	Series	Box size $[h^{-1}\mathrm{Mpc}]$	N_{cdm}	N_{gas}	N_ν	Mass-shell N_{side}	$\sum m_\nu$ [eV]	ϵ_{cdm} $[h^{-1}\mathrm{kpc}]$
DM only	MTNG740-DM-1	A/B	500	4320^3	–	–	12288	–	2.5
	MTNG740-DM-2	A/B	500	2160^3	–	–	9182	–	5
	MTNG740-DM-3	A/B	500	1080^3	–	–	4096	–	10
	MTNG740-DM-4	A/B	500	540^3	–	–	2048	–	20
	MTNG740-DM-5	A/B	500	270^3	–	–	1024	–	40
Hydro	MTNG740-1	A	500	4320^3	4320^3	–	12288	–	2.5
Neutrinos	MTNG3000-DM-0.1ν	A	2040	10240^3	–	2560^3	12288	0.1	4
	MTNG630-DM-0.3ν	A/B	430	2160^3	–	540^3	12288	0.3	4
	MTNG630-DM-0.1ν	A/B	430	2160^3	–	540^3	12288	0.1	4
	MTNG630-DM-0.0ν	A/B	430	2160^3	–	540^3	12288	0.0	4

3.2 Methods

3.2.1 The MTNG project

The MillenniumTNG (MTNG) project is based on a suite of high-resolution cosmological structure formation simulations. The project focuses on the connection between galaxy formation and large-scale structure by combining the statistical power reached with the large box size of the Millennium simulation (Springel et al., 2005), with the high mass-resolution and sophisticated baryonic physics modeling of the IllustrisTNG project (Nelson et al., 2018; Springel et al., 2018; Marinacci et al., 2018; Pillepich et al., 2018; Naiman et al., 2018; Pillepich et al., 2019; Nelson et al., 2019; Nelson et al., 2019). The goal of this synthesis, which inspired the name of the MTNG project, is to realize accurate and reliable theoretical predictions for galaxy formation throughout volumes large enough to be adequate for the upcoming surveys of cosmic large-scale structure.

The initial conditions of MTNG were generated at $z = 63$ with an updated version of the N-GenIC code, directly incorporated in Gadget-4. The algorithm is based on second-order Lagrangian perturbation theory, and the input linear theory power spectrum was the same as the one used for the IllustrisTNG simulations (based on Planck15 cosmological parameters). A new transfer function with updated cosmological parameters was adopted for the simulations with massive neutrinos.

The dark matter (DM)-only simulations were run with the Gadget-4 code (Springel et al., 2021), using the variance-suppression technique introduced by Angulo & Pontzen (2016), so that for every resolution there are two simulations (which we refer to as A- and B-series) whose initial conditions are characterized by perturbations with opposite phases but the same amplitude, fixed to the *rms* value predicted by the power spectrum. The hydrodynamical simulations start from the same initial conditions as the DM A-series and were performed with the moving-mesh Arepo code, featuring the same galaxy formation model as IllustrisTNG (Weinberger et al., 2017; Pillepich et al., 2018), modulo very small changes[1].

[1]Magnetic fields were not included, and the metallicity tracking was simplified. Both were necessary to

The main characteristics of the MTNG simulations that are primarily used in this work are summarised in Table 3.1. For the bulk of our analysis, and in particular for studying the impact of resolution and of baryons, we use a box size of $500\,h^{-1}\mathrm{Mpc} \simeq 740\,\mathrm{Mpc}$. For the cosmological parameters, we use the Planck Collaboration (2016) cosmology, which is consistent with what had been used for IllustrisTNG: $\Omega_\mathrm{m} = \Omega_\mathrm{cdm} + \Omega_\mathrm{b} = 0.3089$, $\Omega_\mathrm{b} = 0.0486$, $\Omega_\Lambda = 0.6911$, $h = 0.6774$, $\sigma_8 = 0.8159$ and $n_s = 0.9667$. For the study of the impact of massive neutrinos, we use a slightly smaller box size of $430\,h^{-1}\mathrm{Mpc} \simeq 630\,\mathrm{Mpc}$, and updated cosmological parameters that also take the different neutrino masses into account (Abbott et al., 2022). We consider three cases for the neutrino masses, $\Sigma m_\nu = 0$ meV (massless), 100 meV, and 300 meV (see Table 3.1). The reader is referred to Hernández-Aguayo et al. (2022) and Pakmor et al. (2022) for a more detailed description of the MTNG simulations. We simulate the effect of massive neutrinos using the so-called δf method introduced in Elbers et al. (2021), however, we refer to Hernández-Aguayo et al. (2024) for a detailed description of the technical aspects of the simulations with neutrinos.

3.2.2 Mass-shell outputs

Along with snapshot and lightcone data (see Hernández-Aguayo et al., 2022, for further details), the MTNG simulations provide "mass-shell" outputs, introduced as a new feature in Gadget-4. These consist of a series of onion-shell-like full-sky maps built on-the-fly, which store the line-of-sight projected matter field of the full-sky lightcone. Each shell consists of a HEALPix map (Hivon et al., 1999), where each pixel contains, in turn, the total mass of all particles that intersect the lightcone's time-variable hypersurface[2] at a comoving distance that falls within the shell boundaries, and at an angular position that falls within the solid angle corresponding to the pixel. For all the simulations of the MTNG suite, we fixed the comoving depth of these shells to $25\,h^{-1}\mathrm{Mpc}$. The angular resolution of a HEALPix map is modulated by the N_side parameter, which determines the total number of pixels through $N_\mathrm{pix} = 12\,N_\mathrm{side}^2$. For simulations with increasing mass resolution, we typically constructed mass-shells with increasing N_side, as can be seen in Table 3.1. The highest angular resolution we reach with the mass-shells is 0.28 arcmin, given by $N_\mathrm{side} = 12288$, which corresponds to approximately 1.8 billion pixels in the sky.

3.2.3 Computation of full-sky convergence maps

Starting from the mass-shell output, we developed a Gadget-4 post-processing Python package for the computation of full-sky convergence maps in the Born approximation. This works as follows. The i-th mass-shell can be converted into an angular surface mass density distribution Σ dividing the mass at each pixel's angular position by the area of each pixel

reduce the memory consumption of the production run to make it fit into the available memory.

[2]This is simply the spherical surface whose comoving radius varies with time according to the finite propagation speed of light, and reaches the observer at the present time.

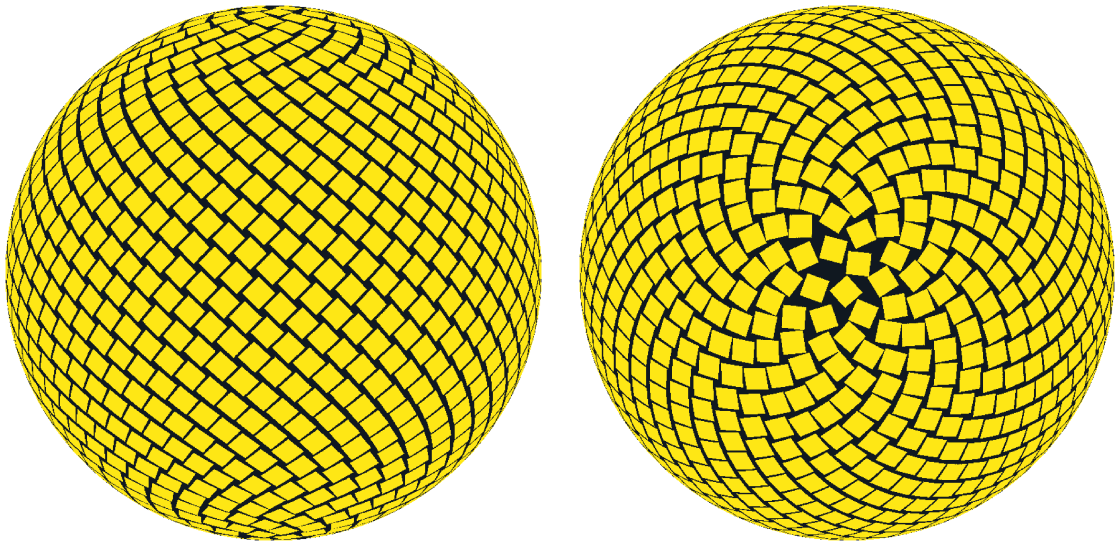

Figure 3.1: Orthographic projection from the side (left) and from above (right) of the 1195 square maps with size $5 \times 5\,\mathrm{deg}^2$ that we extract from a full-sky map. The method we use is based on the Fibonacci grid and manages to cover $\approx 72\%$ of the sphere surface.

in steradians (given by $A_{\rm pix} = 4\pi/N_{\rm pix}$, since HEALPix has equal area pixels):

$$\Sigma^{(i)}(\boldsymbol{\theta}) = \frac{M(\boldsymbol{\theta})}{A_{\rm pix}}\,. \tag{3.1}$$

Every shell is then treated as a lens. For a fixed source redshift z_s, the convergence in the Born approximation will be given by integrating over the surface mass density at every lens plane (i.e. at every shell) between the source and the observer, weighted by the lensing efficiency factor:

$$\kappa(\boldsymbol{\theta}, \chi_s) = \frac{4\pi \mathrm{G}}{\mathrm{c}^2}\frac{1}{f_{\rm s}}\sum_i (1+z_{\rm d}^{(i)})\frac{f_{\rm ds}^{(i)}}{f_{\rm d}^{(i)}}\left[\Sigma^{(i)}(\boldsymbol{\theta}) - \bar{\Sigma}^{(i)}\right]\,, \tag{3.2}$$

where $\bar{\Sigma}^{(i)}$ is the mean angular surface mass density of the i-th shell. To optimize computational efficiency, this calculation is parallelized with MPI4PY (Dalcin & Fang, 2021).

3.2.4 Partitioning into square patches

Once a full-sky map is created, one may want to partition it into smaller non-overlapping square patches in order to simplify the analysis. Performing this operation in an efficient way, i.e. covering as much as possible of the sphere's surface while avoiding overlap, is not a trivial task. An example is found in Davies et al. (2019), where a HEALPix-based partitioning is performed to extract 192 maps with size $10 \times 10\,\mathrm{deg}^2$; this scheme covers $\approx 47\%$ of the sphere's surface.

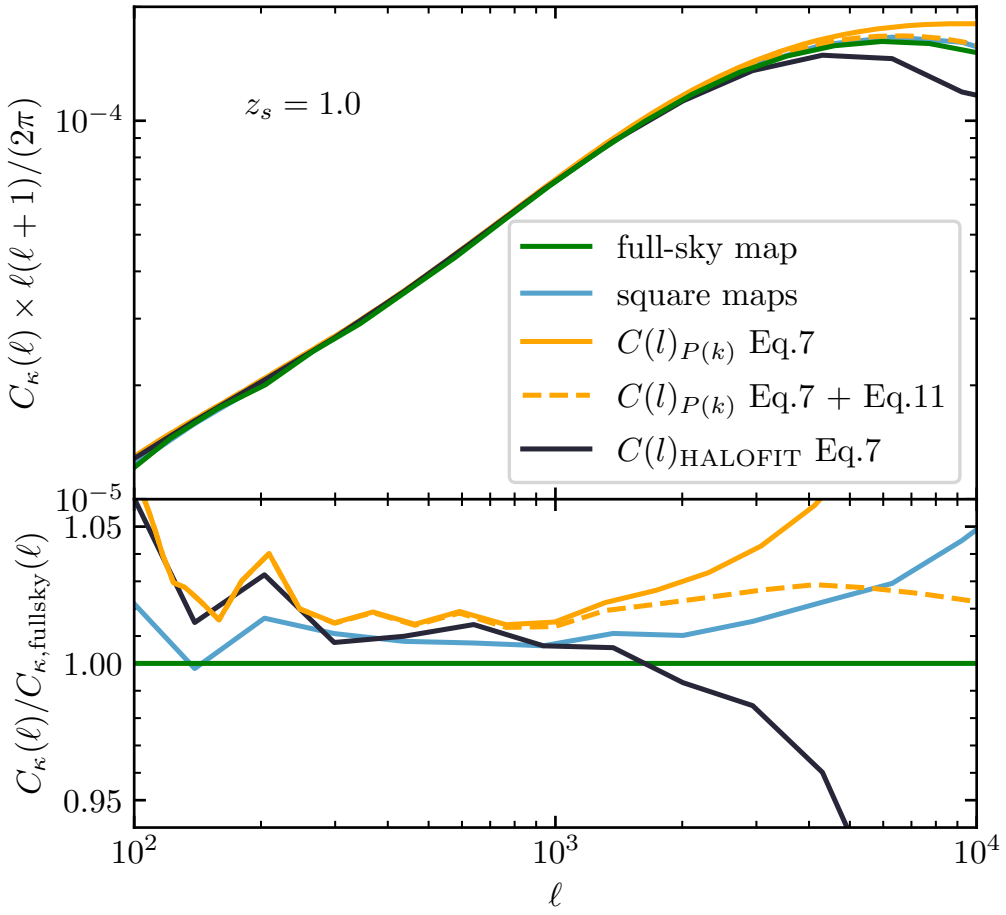

Figure 3.2: Lensing convergence power spectra (upper panel) of MTNG740-DM-1B obtained with our code from $N = 1195$ non-overlapping $5 \times 5\,\mathrm{deg}^2$ square maps (light blue line), and from the full-sky map (green line). These are compared with the convergence power spectrum obtained starting from the redshift-dependent non-linear 3D matter power spectra of the simulation (yellow lines, with the dashed line accounting for the suppression due to finite angular resolution as modeled by Eq. (3.4)) and from 3D power spectra given by the HALOFIT formula (black line). In both cases, the 3D matter power spectra are integrated according to Eq. (2.9). Ratios relative to the full-sky map are shown in the lower panel.

In this work, we introduce a new and more efficient way of partitioning the sphere into smaller square maps. This is directly inspired by a botanical phenomenon known as *phyllotaxis* (from Latin "leaf arrangement"), which refers to the way in which plants arrange their repeating parts (leaves, seeds, florets, etc...) in order to maximize the space occupation (see e.g., Conway & Guy, 1996, p. 113). It turns out that in many cases (e.g., for the dandelion seeds or the florets on the sunflower head) the spatial distribution of points is mathematically described by the so-called Fibonacci grid. As shown in Swinbank & Purser (2006), the spherical coordinates which describe the i-th point on a Fibonacci

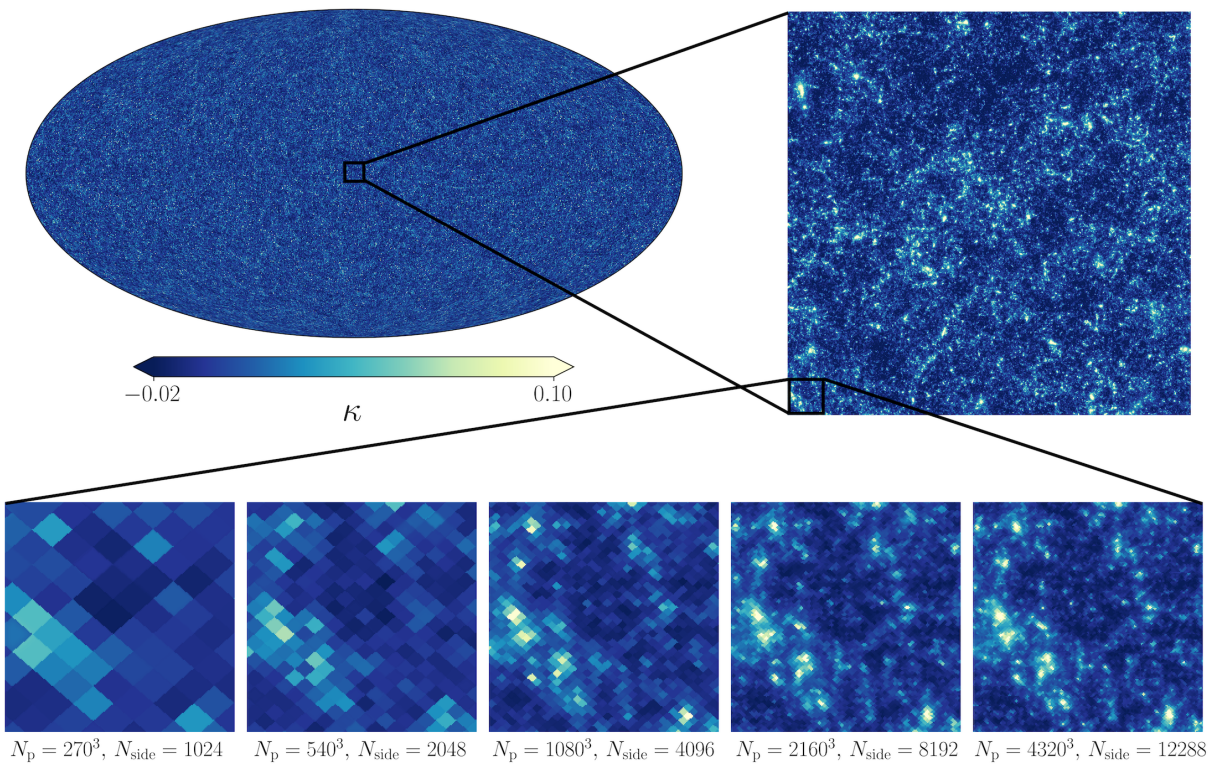

Figure 3.3: The top left shows a full-sky convergence map with $z_s = 1.0$ computed with our code from DM only runs with same initial conditions, but increasing resolution both in mass and in angles; the zoom on the top right focuses on a single $5 \times 5\,\mathrm{deg}^2$ square patch. The bottom panels show a further zoom onto a square region of $0.5 \times 0.5\,\mathrm{deg}^2$; these all represent the same region with increasing resolution from left to right.

grid with a total of $2N + 1$ points are given by,

$$\sin\theta_i = \frac{2i}{2N+1},\ \ \phi_i = \frac{2\pi i}{\varphi},\ \ -N \leq i \leq N,\ \ -\pi/2 \leq \theta_i \leq \pi/2, \tag{3.3}$$

where $\varphi \approx 1.618$ is the golden ratio. We use these coordinates as the centers of our maps[3]. In addition, for square patches, we find that the coverage of the sphere is maximized when one diagonal of the squares lies on a meridian. Using this method, we place 1195 square patches of size $5 \times 5\,\mathrm{deg}^2$; therefore covering $\approx 72\%$ of the sphere's solid angle (the same approximate percentage would also be reached in the case of $10 \times 10\,\mathrm{deg}^2$ square patches). The arrangement of spherical squares is shown in Figure 3.1. Every square patch we extract is sampled on a regular grid with 2048^2 pixels, resulting in a pixel size of about 0.14 arcmin.

[3]Instead of following Eq. (3.3), the first ≈ 10 patches closest to each pole have been placed manually, in order to avoid overlapping.

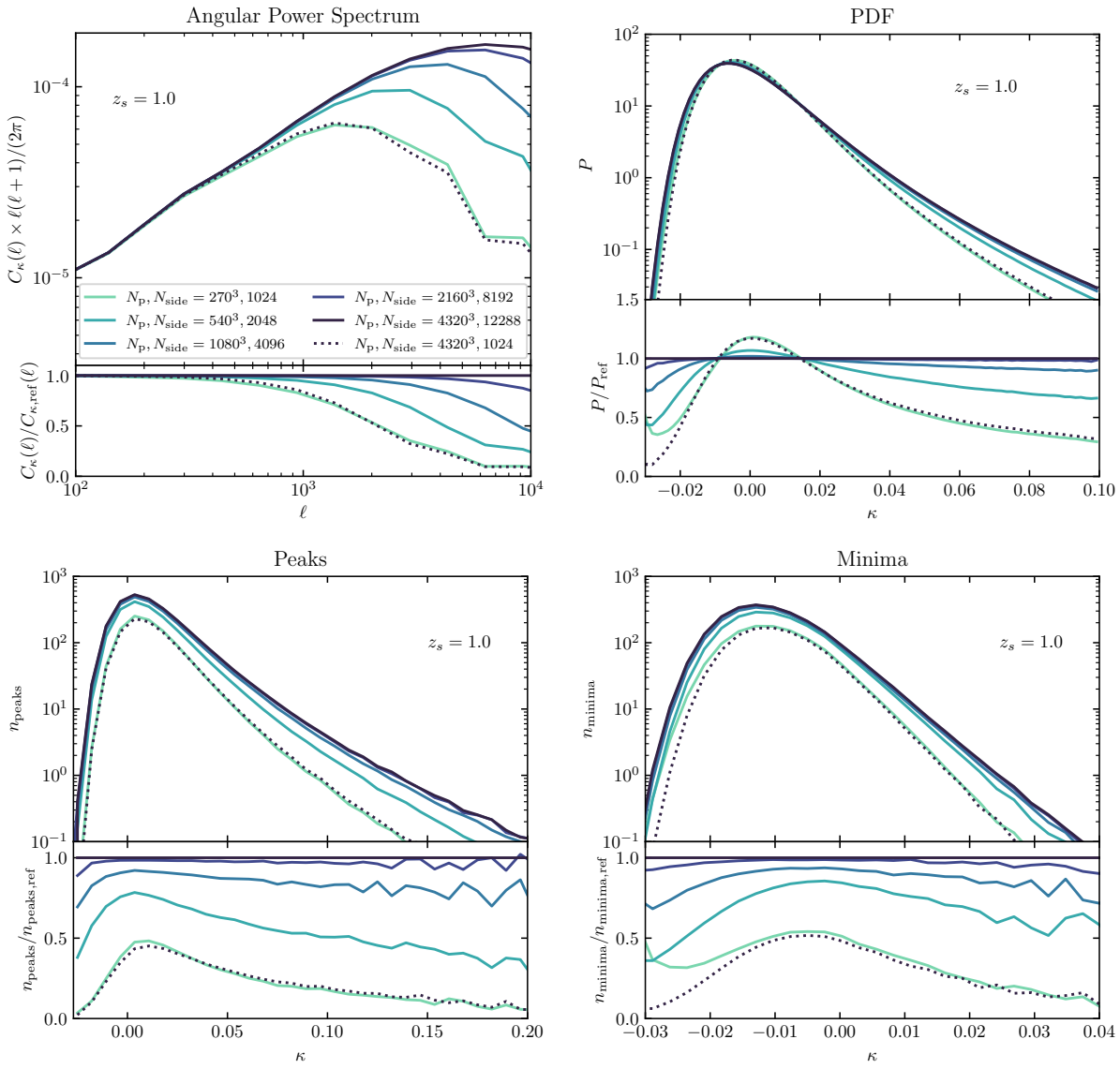

Figure 3.4: Top left: WL convergence power spectrum; top right: WL convergence PDF; bottom left: WL convergence peak counts; bottom right: WL convergence minimum counts. All the observables are computed on the B realization of the MTNG740-DM runs, taking $z_s = 1.0$. The solid lines indicate the mean of 1195 $5 \times 5\,\mathrm{deg}^2$ square maps with increasing darkness representing increasing resolution both in mass and N_side. The dotted line refers to the case with the highest mass resolution but down-sampled to $N_\mathrm{side} = 1024$. In each lower sub-panel, we show the ratio w.r.t. the reference case with $N_\mathrm{part} = 4320^3$ and $N_\mathrm{side} = 12288$ (noted with the subscript "ref").

3.2.5 Computation of the observables

We compute angular power spectra by means of the HEALPix `anafast` routine. This operation has been performed for maps with resolution up to $N_\mathrm{side} = 8192$, which marks

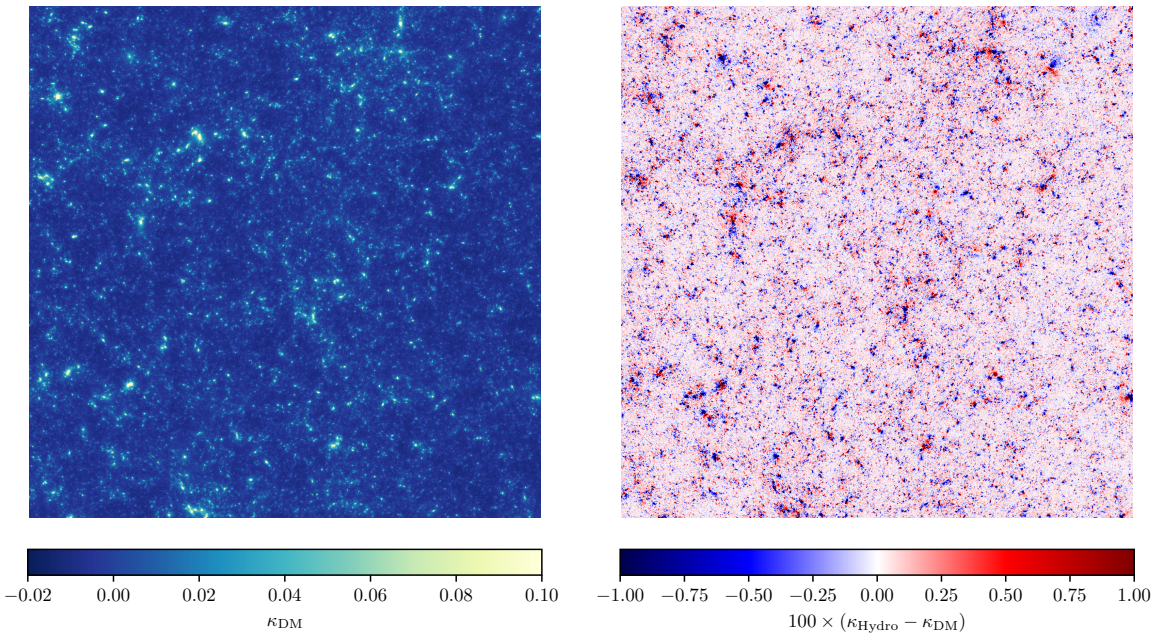

Figure 3.5: Left panel: one of our $5 \times 5\,\mathrm{deg}^2$ square maps at $z_s = 0.5$ from MTNG DM-only run. Right panel: the same map but with the map from the corresponding MTNG hydro run (with the same initial conditions) subtracted.

the maximum resolution for which the HEALPix library is able to perform a spherical harmonics decomposition. In the case of square patches, the power spectra are calculated with Fourier transforms on a regular grid with 2048^2 pixels in the flat-sky approximation, which is valid for the small field-of-view covered by their relatively small area ($5 \times 5\,\mathrm{deg}^2$). The full-sky spectra are then binned into 80 equally spaced logarithmic bins in the range $\ell \in [10^0, 10^4]$. The spectra extracted from the square patches are binned into 20 equally spaced logarithmic bins in the range $\ell \in [10^2, 10^4]$. Before computing the probability distribution function for the convergence, and its peaks and minima statistics, all the square maps are smoothed with a Gaussian kernel characterized by a standard deviation of 1 arcmin. We compute the PDF in 50 linearly spaced convergence bins in the range $\kappa \in [-0.05, 0.1]$. We identified peaks and minima as pixels in the maps that are greater or smaller than their 8 nearest neighboring pixels, respectively. We bin the peak counts into 50 equally spaced bins with $\kappa \in [-0.1, 0.25]$, and the minima counts into 50 equally spaced bins with $\kappa \in [-0.07, 0.06]$. We have fewer maps for the case that includes baryons, as explained in (Sec. 3.3.2), therefore the peak counts are binned into 12 equally spaced bins with $\kappa \in [-0.02, 0.1]$ and the minima counts into 16 equally spaced bins with $\kappa \in [-0.07, 0.06]$. Statistics are computed using only one simulation run (B for the study on resolution, A for the impact of baryons and massive neutrinos) except in the section 3.3.4 in which combined results from both A and B series runs are also calculated. Unless stated otherwise, all the observables are computed for a source redshift of $z_s = 1.0$. Finally, we do not include galaxy

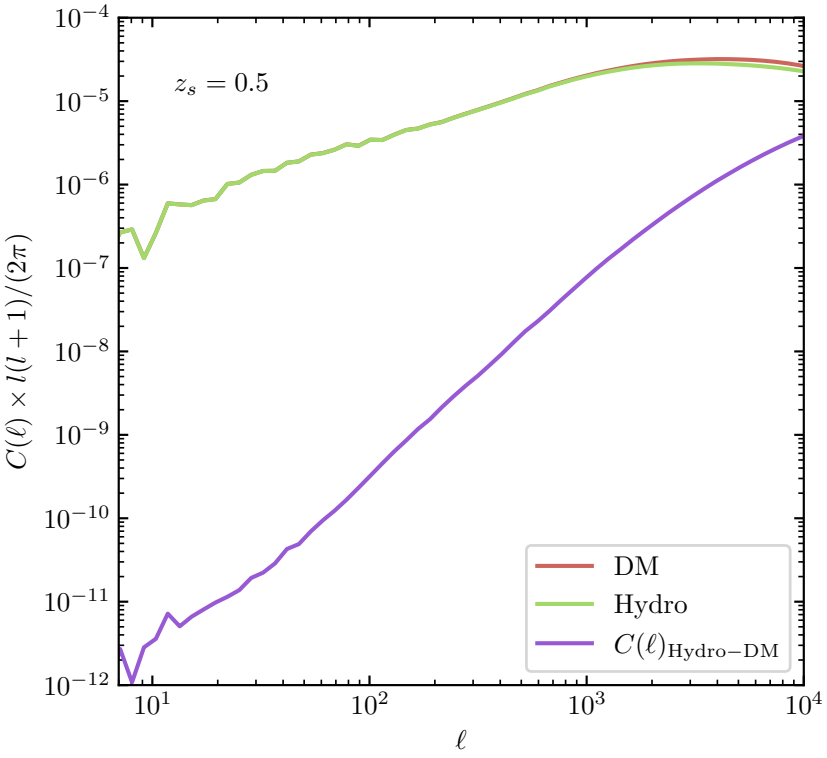

Figure 3.6: Power spectra of full-sky lensing convergence maps assuming $z_s = 0.5$. The red and green lines indicate results for the DM-only and Hydro runs, respectively. The purple line indicates the power spectrum of the difference between the two maps.

shape noise in this analysis, as the focus of this study is to investigate the properties of the physical signal.

3.3 Results

We begin the presentation of our results with the following sanity check shown in Figure 3.2. We compute the convergence power spectrum in four different ways:

- We take the average of the convergence power spectrum computed on a large number of $5 \times 5\,\mathrm{deg}^2$ square maps extracted from the MTNG740-DM-1-A full-sky map.
- We compute the angular power spectrum of the full-sky map of the MTNG740-DM-1-A simulations by means of the HEALPix `anafast` routine.
- We use Eq. (2.9) to obtain the convergence power spectrum by integrating over the 3D matter power spectra measured for MTNG740-DM-1-A at the discrete set of snapshot times.

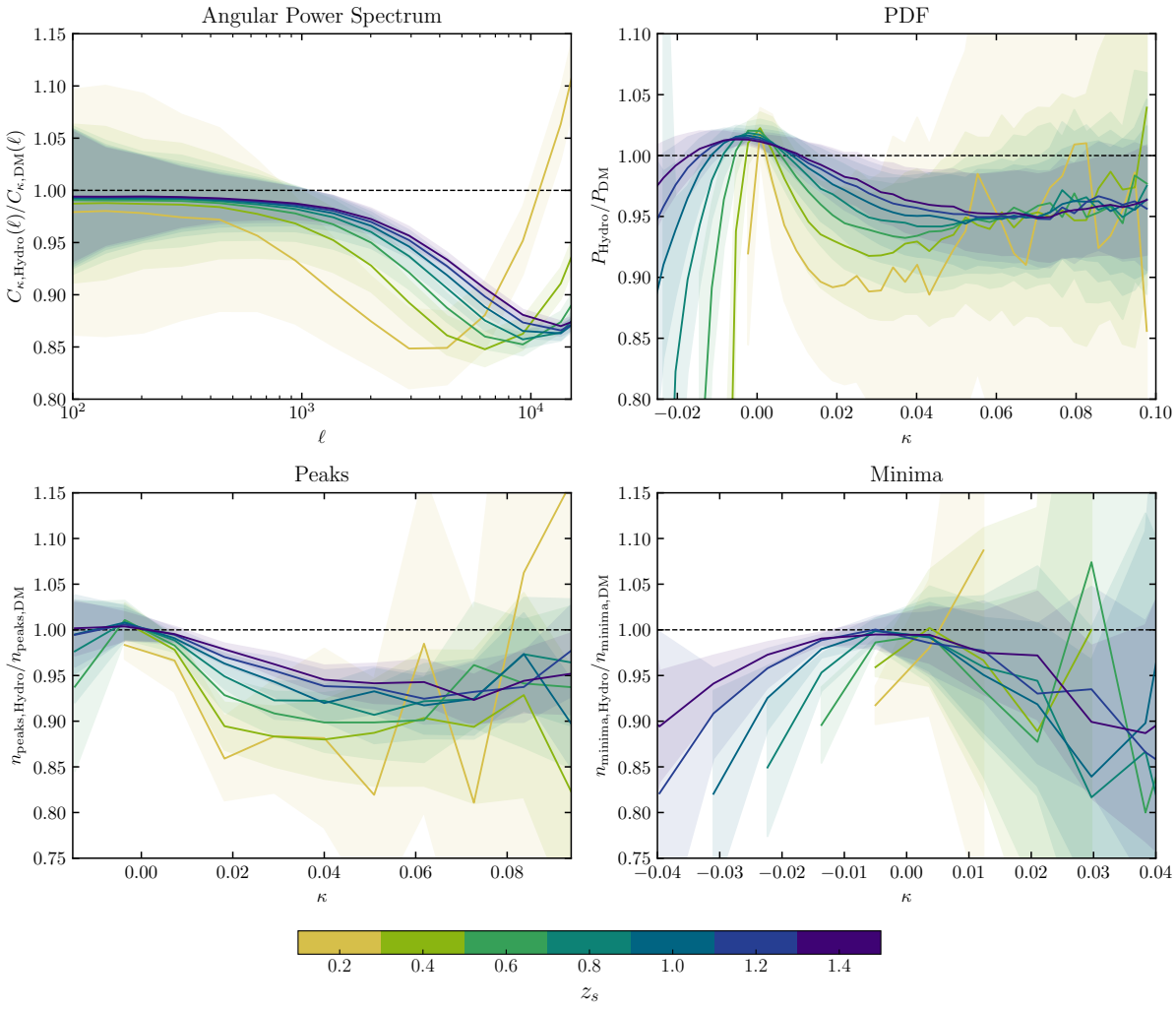

Figure 3.7: Top left: WL convergence power spectrum; top right: WL convergence PDF; bottom left: WL convergence peak counts; bottom right: WL convergence minimum counts. All the panels show the ratio of the results computed from full-hydro and DM-only runs obtained with our code, considering $z_s \in [0.2, 1.4]$ with $\Delta z_s = 0.2$. The solid lines indicate the mean of 125 $5 \times 5\,\mathrm{deg}^2$ square maps, with the shaded regions representing the standard errors on the means.

- Finally, we use the same approach but plug in the 3D matter power spectrum as predicted by the HALOFIT emulation formula (Takahashi et al., 2012a) using the CLASS code (Blas et al., 2011).

As Figure 3.2 shows, we find quite good agreement between the four spectra. Those computed from the full-sky map and from the square patches differ by less than 2.5% over $100 \lesssim \ell \lesssim 4000$, indicating the validity of the flat sky approximation in this regime. The increasing discrepancy at smaller angular scales, i.e. for $\ell \gtrsim 4000$, is consistent with our predictions for different angular resolutions of the maps, as we will discuss in detail in the next section. The loss of power for HALOFIT (black curve) at $\ell \gtrsim 4000$ is most likely

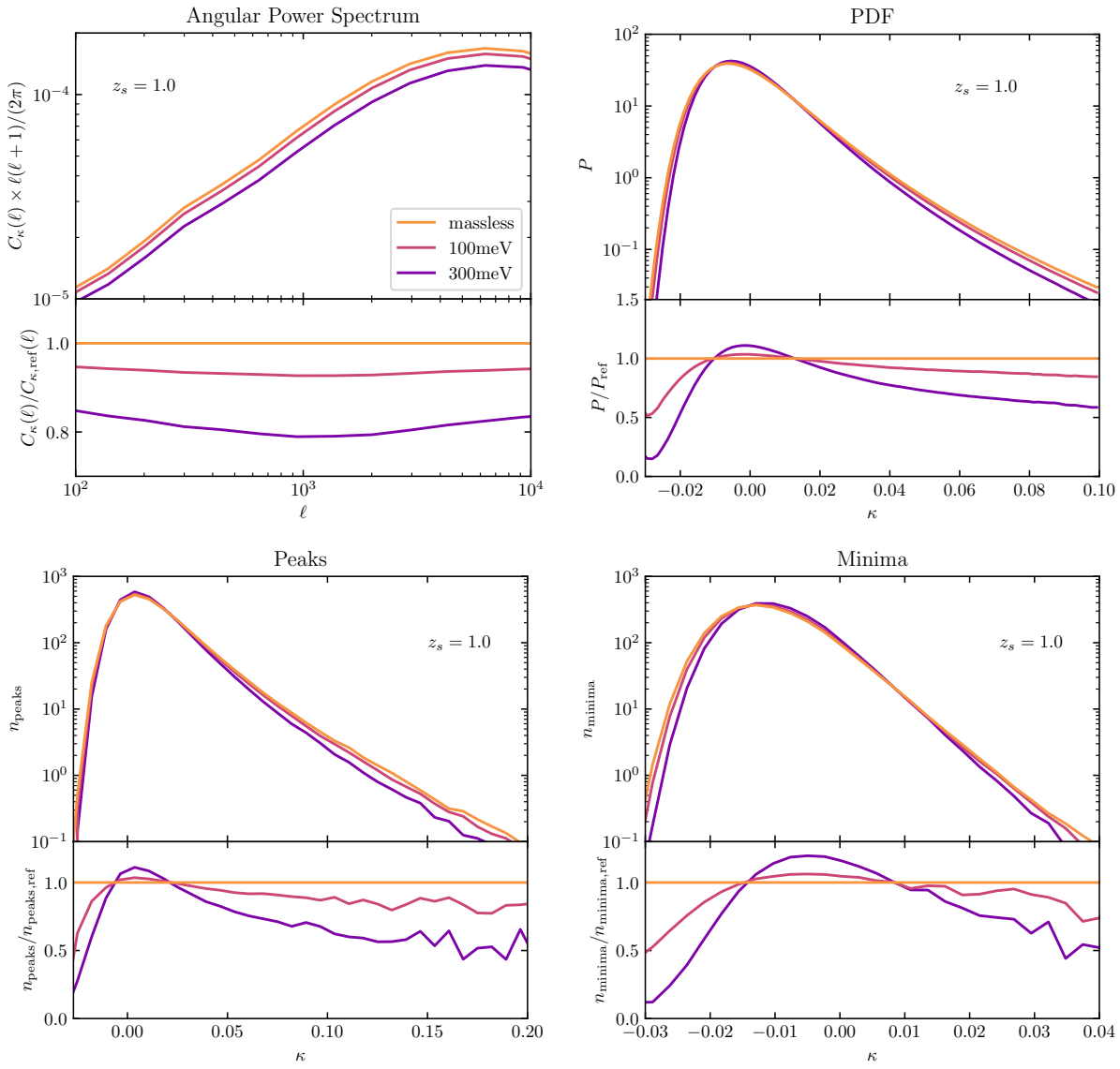

Figure 3.8: Top left: WL convergence power spectrum; top right: WL convergence PDF; bottom left: WL convergence peak counts; bottom right: WL convergence minimum counts. The orange, pink, and violet curves indicate the mean of 1195 $5 \times 5\,\mathrm{deg}^2$ square maps computed on simulations with summed neutrino masses equal to $0, 100, 300\,\mathrm{meV}$ respectively.The lower subpanels show the ratio of each distribution to that of the case with zero neutrino masses.

explained by the fact that this model was calibrated on simulations with lower resolution. On the other hand, we observe that the spectra computed from our maps (both full-sky and square patches) tend to lose power at $\ell \gtrsim 4000$ with respect to the prediction obtained by plugging in the 3D matter power spectra computed from the simulation into Eq. (2.9). This effect can be explained by the finite angular resolution of the maps. As noted by Takahashi

et al. (2017), one can approximately describe this effect by introducing a damping factor:

$$C_\kappa(\ell) \to \frac{C_\kappa(\ell)}{1 + (\ell/\ell_{\rm res})^2} \ . \tag{3.4}$$

By setting the free parameter $\ell_{\rm res} = 2\,N_{\rm side}$ (yellow dashed curve), we recover the 5% concordance at the smallest scales.

3.3.1 Numerical resolution study

In Figure 3.3 we show an example of a full-sky convergence map computed with our code. We zoom in on such a map to show an example of an extracted $5 \times 5\,{\rm deg}^2$ square patch. A further zoom-in to a $0.5 \times 0.5\,{\rm deg}^2$ square region is performed to give a visual impression of how the different angular resolutions look at the smallest scales. By comparing this zoomed region for the $N_{\rm side} = 1024, 2048$ and the $N_{\rm side} = 8192, 12288$ cases, one can see that information on structures on the smallest angular scales is progressively lost as the resolution becomes lower. In this subsection, we investigate how this loss of angular resolution, in combination with reduced mass resolution in the simulation itself, can impact weak lensing observables extracted from the corresponding convergence maps. All the following observables are computed as averages of the 1195 square maps of size $5 \times 5\,{\rm deg}^2$ extracted from the full-sky maps from the B realization of MTNG740-DM runs.

The first observable we study is the convergence power spectrum, as shown in the top left panel of Figure 3.4. The solid lines refer to simulations increasing both in mass resolution and angular resolution. This shows that decreasing the resolution (both in mass and angle) reduces the power at progressively larger scales. We verified that this effect is generally independent of z_s over the range $z_s \in [0.2, 3.0]$. In order to understand how much of this reduction in power is due to the decrease in angular resolution and how much is due to the decrease in mass resolution, we now consider the convergence maps of the simulation with the highest mass resolution but down-sample the maps to $N_{\rm side} = 1024$, this is represented by the dashed line. We see that for the fixed angular resolution $N_{\rm side} = 1024$ we obtain essentially the same result, independent of the mass resolution. The small-scale suppression we find with the decreasing resolution is consistent with the one found in previous studies (see e.g., Takahashi et al., 2017).

Next, we consider how changes in the resolution impact the WL one-point PDF; the results are shown in the top right panel of Figure 3.4. First, we see that the PDF is characterized by an asymmetrical shape that reflects the non-Gaussian nature of the WL convergence. The solid lines (which refer to increasing angular and mass resolution) show a broadening of the distribution when the resolution is increased. Since the maps with the higher angular resolution are able to capture the details of the smaller (angular) structures, more extreme convergence values are resolved; as seen in Figure 3.3, this results in a broader PDF. This explanation is supported by the dashed line (referring to the simulation with the highest mass resolution, but down-sampled to $N_{\rm side} = 1024$) which is almost indistinguishable from the solid line which refers to maps computed with the same angular

resolution but from a simulation with much lower mass resolution. We find that angular resolution affects the convergence PDF similarly for source redshifts over the full range $0.2 \leq z_s \leq 3$. The narrowing of the PDF we observe here is consistent with the suppression of the power spectrum seen previously. The comparison between these two indicates that the most extreme values of κ are contained in the smallest angular scales.

Finally, we present that same investigation for the WL peak and minimum counts; the results are shown in the left and right lower panels of Figure 3.4, respectively. For the peak counts, we find that when increasing resolution in angle and mass, the high κ tail is more extended and the amplitude of the distribution increases. For the distribution of minimum counts also, we see an increase in amplitude with increasing resolution. In both cases, the suppression of the counts with decreasing resolution is not uniform; in particular, it is stronger for higher κ values. Again, we conclude that the differences are dominated by the angular resolution, since the high-mass-resolution simulation, once down-sampled to $N_{\rm side} = 1024$, is again almost indistinguishable from the low-mass-resolution simulation analyzed with the same $N_{\rm side}$. As before, we find qualitatively similar results for source redshifts throughout the range $z_s \in [0.2, 3.0]$. The results we find for peak and minimum abundance are consistent with what has been seen for the PDF: decreasing the resolution will narrow the PDF, therefore damping the most extreme values of κ, which in turn will result in fewer counts of peaks and minima. Finally, we tested the impact of varying the smoothing scale applied to the convergence map before the PDF, peak counts, and minima counts were computed, and found that the results are qualitatively consistent with Figure 3.4. We refer the interested reader to Appendix A, where we show and discuss these results.

3.3.2 Impact of baryons

In this section, we study the impact of baryonic physics on weak lensing observables. In the left panel of Figure 3.5, we show a $5 \times 5\,\mathrm{deg}^2$ square patch with $z_s = 0.5$ extracted from a full-sky map for MTNG740-DM-1-A. We do not separately show the corresponding convergence map for the hydro run (which was run with the same initial conditions) as the difference with respect to the DM case is almost imperceptible by eye. Instead, in the right panel, we show the difference between the two maps. By comparing the two panels, we notice that the regions where the baryonic physics has the strongest impact (redder and bluer areas in the right panel) roughly correspond to regions where the convergence map has high values (lighter areas in the left panel, corresponding to massive structures). We also see that the difference is often characterized by a dipole pattern (neighboring red-blue pairs). This largely reflects the fact that the same objects can end up having slightly different positions when baryonic physics is included and does not necessarily signal a significant difference in internal structure between the two cases.

In order to quantify how baryonic processes affect different angular scales, we compute the power spectrum of the difference between the two full-sky maps; this is shown as a purple line in Figure 3.6, which is compared to the power spectra of the two individual maps. We see that the power spectrum of the difference map drops rapidly and approximately

as a power law towards large scales. The impact of baryonic physics increases strongly towards smaller angular scales over the range of l-values considered here.

We now consider results for the four primary observables considered previously, adopting a set of source redshifts over the range $z_s \in [0.2, 1.4]$ with $\Delta z_s = 0.2$. For the hydrodynamic simulation MTNG740-1, a code configuration error, unfortunately, caused the loss of the original full-sky mass-shells for $z > 0.5$, which were intended to be produced on-the-fly. However, it proved possible to reconstruct these data partially in post-processing, because the full-particle lightcone of the simulation was stored for one octant of the sky out to $z = 1.5$. Straightforwardly binning this data onto HEALPix arrays thus allows lensing maps to be recovered over 1/8-th of the full sky out to this redshift. While this restricts us to a direct comparison of just 125 square maps (those that fall into the first octant), resulting in a somewhat larger statistical error (as indicated by the shaded regions that give standard errors), this does not substantially weaken our ability to assess the small-scale impact of baryonic physics.

In the top left panel of Figure 3.7, we show the ratio between the convergence power spectrum of DM-only and Hydro runs. We observe a small and almost constant suppression at the larger angular scales and a stronger, scale-dependent suppression at smaller scales. The transition between these two regimes takes place at $\ell \approx 10^3$ and happens at progressively larger ℓ with increasing z_s. The overall effect produces a spoon-shaped suppression which reaches $\approx 15\%$. The dominant component of the power suppression can be explained in terms of feedback from black hole accretion and supernovae explosions, which blow away matter from the central regions of the halos. This will primarily affect relatively small physical (and consequently angular) scales, but the associated redistribution of baryons also induces an impact on larger scales, particularly due to AGN as they are capable of affecting very massive halos. The shift of the spoon feature that we observe can be explained by considering that the physical scale at which the effect of baryons suppresses the most the power spectrum, will correspond to smaller angular scales (and therefore higher values of ℓ) for increasing z_s.

We show the ratio between the WL PDF in the Hydro and in the DM-only cases in the top right panel of Figure 3.7. We find a roughly constant $\approx 5 - 10\%$ suppression in the high-κ tail for the Hydro run relative to the DM-only run. In the low-κ regime, there is a suppression as well, and this increases dramatically as κ becomes more negative. The central region of the PDF is in turn enhanced by $\approx 2 - 3\%$. These changes impact a progressively broader κ range as z_s increases. Finally, we consider the effect of baryonic physics by considering the WL peaks and minima, shown in the right and left panels of Figure 3.7, respectively. In the case of the peak abundance, we observe a suppression of $\approx 5 - 15\%$ for $\kappa \gtrsim 0.02$, which is stronger for decreasing z_s; although the results are noisier in the case of lower z_s. The distribution of the minima shows suppression in the baryonic case in both the high-κ and low-κ tails, and this effect increases the more κ reaches extreme values. The trend is approximately symmetric and broader in κ as z_s increases.

The effects we observe are consistent with the physical explanation given previously for the power spectrum: feedback processes redistribute matter from denser regions to lower-density regions. This manifests in a narrower PDF, and in a suppression of the

peaks and minima counts. In particular, the high-κ peaks are expected to correspond mostly to the presence of galaxy clusters along the line of sight, while the low-κ peaks could be produced by haloes in voids or chance alignments of small haloes along the line of sight. We, therefore, expect the baryons to impact the peak abundance in a κ-dependent fashion. This could help in explaining the upturn we see for increasing κ (for a more detailed discussion we direct the reader to e.g., Liu & Haiman, 2016; Yang et al., 2011; White et al., 2002).

Finally, we notice that the impact of baryonic physics on all four observables is progressively stronger with decreasing z_s: we indeed expect this to happen because, at lower redshifts, baryonic processes have had more time to take place and therefore influence the overall cosmic structure.

3.3.3 Impact of neutrinos

Another important element that influences structure formation, and therefore WL observables, is the presence of massive neutrino species. In the early Universe, these act as an additional relativistic component, thus delaying the onset of structure formation and suppressing the formation of structures below the free-streaming scale (for reviews, the reader is redirected to e.g., Lesgourgues & Pastor, 2006; Wong, 2011). We, therefore, expect massive neutrinos to reduce the WL signal at those scales. Consequently, the use of WL has been suggested as a tool to constrain the neutrino mass (see, e.g., Cooray, 1999). In the following, we show results obtained by comparing MTNG DM-only with runs that include neutrino components with different overall mass contributions, corresponding to summed neutrino rest masses of $\sum m_\nu = [0, 100, 300]$ meV.

We start by considering the angular power spectrum, which is shown in the top left panel of Figure 3.8. We notice that this is suppressed by ≈ 5 and $15-20\%$ for $\sum m_\nu = 0.1$ and 0.3 eV, respectively, relative to the massless case. The suppression is slightly greater for intermediate angular scales ($\ell \approx 1000$); this effect, which is barely noticeable in the $\sum m_\nu = 0.1$ eV case, becomes more prominent for $\sum m_\nu = 0.3$ eV. Such an effect is consistent with massive neutrino species suppressing structure formation on small scales. We verified that, as expected, this effect decreases significantly at the smallest l-values.

We show the convergence PDF in the top right panel of Fig. 3.8. Here the distribution is enhanced in its central region (for $-0.015 \leq \kappa \leq 0.015$) of order ≈ 11 and 4% for the $\sum m_\nu = 0.1$ and 0.3 eV cases, respectively. On the other hand, we see that the PDF is progressively suppressed in the tails, an effect that gets stronger for higher neutrino masses. Interestingly, we find that the impact of massive neutrinos on the convergence PDF is quite similar to that induced by decreasing the angular resolution of the map, as one can notice by comparing this panel with the top left panel of Fig. 3.4. The effect we observe is consistent with the physical interpretation given above: massive neutrinos will smooth out the density field, therefore narrowing the PDF of the WL convergence.

Finally, in the bottom panels of Fig. 3.8 we consider the effect of neutrinos on the convergence peak and minimum counts. For the peak counts, we see an enhancement for $-0.015 \leq \kappa \leq 0.015$, reaching $\approx 11\%$ for $\sum m_\nu = 0.3$ eV and $\approx 4\%$ for $\sum m_\nu = 0.1$ eV.

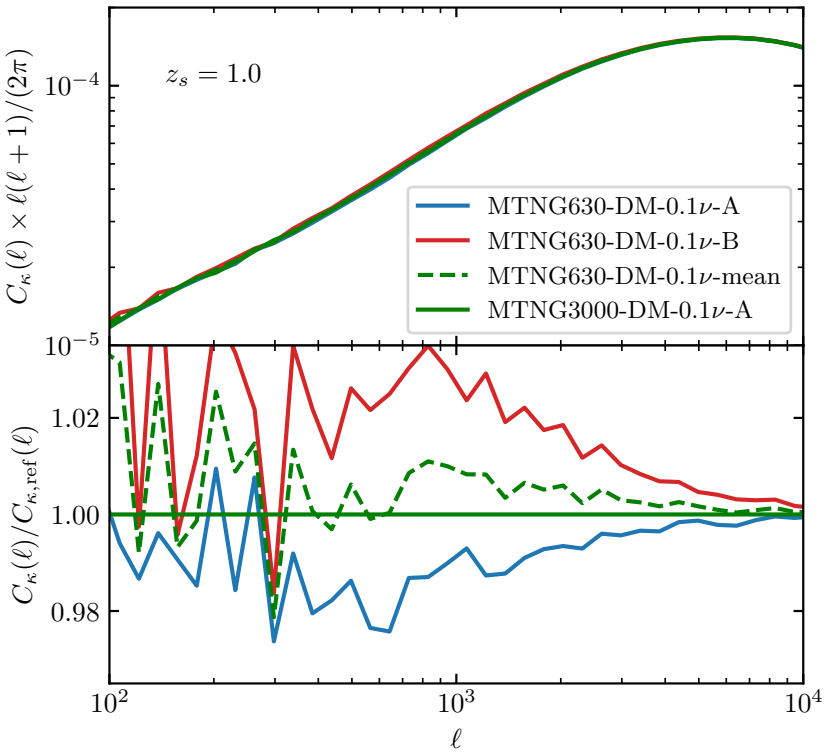

Figure 3.9: Lensing convergence power spectrum of full-sky convergence maps computed with our code considering $z_s = 1.0$. The blue and red lines indicate respectively the A and B series with fixed and paired initial conditions of MTNG630-DM-0.1ν, the dashed green line refers to the mean of these two, while the solid green line to the run with the biggest box size, i.e. MTNG3000-DM-0.1ν. In the lower sub-panel, we show the ratio w.r.t. the MTNG3000-DM-0.1ν run (noted with the subscript "ref").

In the case of the minimum counts, the enhancement is present at $-0.015 \leq \kappa \leq 0.01$ and reaches $\approx 20\%$ and 6% for $\sum m_\nu = 0.1$ and 0.3 eV, respectively. Both the peak and minima counts are progressively suppressed along the tails of the distribution, and this effect becomes again stronger when the mass of neutrinos increases. What we observe is consistent with the effects on the PDF and the power spectrum. Massive neutrino species will tend to fill the emptiest regions, thus suppressing the negative-κ tail of the minimum counts, and oppose the formation of large structures, thus damping the high-κ tail of peak counts.

3.3.4 Paired and fixed initial conditions

To conclude the presentation of our primary results, we investigate the impact of the variance suppression technique introduced by Angulo & Pontzen (2016). As they show, averaging the 3D matter power spectra of two simulations with fixed and paired initial conditions can reduce the noise due to cosmic variance very significantly (for another work

that employs a variance suppression technique inspired by the previous citation, we direct the reader to Harnois-Déraps et al., 2019). Here we test whether this approach also helps in the case of the convergence angular power spectrum. This requires a redshift integration over the lightcone, rather than a single time-slice of the underlying simulation, so it remains to be validated that the cancellation of second-order deviations from linear theory will work equally well in this case.

We show our results for this in Figure 3.9, where the blue and red lines indicate the angular power spectra of full-sky convergence maps computed for the A and B versions of MTNG630-DM-0.1ν, respectively, while the green dashed line shows their mean. For comparison, the power spectrum obtained from the full-sky lightcone of the A version of MTNG3000-DM-0.1ν is shown as a green solid line. Because of its larger box, the initial conditions of this simulation contain about 100 times as many modes on each scale as those of the smaller box simulations, and so the cosmic variance in its power spectrum is expected to be about 10 times smaller. We find that the power spectra of the smaller simulations differ from each other by up to 5% and from the power spectrum of the big simulation by up to 3% for $300 \leq l \leq 10^4$. Their mean, however, differs from the power spectrum of the big run by a maximum of 1% and by much less at the smaller angular scales. Thus, although the suppression of cosmic variance is less strong than found by Angulo & Pontzen (2016) for the power spectra of the dark matter distribution in simulation snapshots, it is still very substantial, thus supporting the notion that the fixed and paired technique is an effective way to reduce cosmic variance uncertainties in simulation results also for WL observables.

3.4 Discussion

We now discuss the implications of the results presented in the previous sections, in particular, for the relative impact of baryons and massive neutrinos on WL observations. Further, we compare our estimates of these effects with results from other recent studies.

The four panels of Figure 3.10 show results for the four convergence map observables that we focus on in this study, the angular power spectrum (top-left), the one-point PDF (top right), and the peak and minimum counts (bottom left and bottom right). In this case, in order to make the comparison consistent with other works, we smoothed the square maps with a Gaussian kernel with a standard deviation of 2 arcmin when studying the PDF, peak, and minimum counts. As in Figure 3.7 and in the lower subpanels of Figure 3.8 we plot the ratios of results obtained in a simulation including either baryons or massive neutrinos to those for a simulation from identical initial conditions that followed only the CDM. First, we discuss the new results from this work, which is represented by the thicker lines: green for the baryons, blue for $\sum m_\nu = 0.1$ eV, and dark blue for $\sum m_\nu = 0.3$ eV. For the last case, neutrino effects dominate baryonic effects for all four observables: the suppression of the power spectrum, the distortion induced in the PDF, and the modification of the peak and minimum counts are all substantially stronger. On the other hand, for $\sum m_\nu = 0.1$ eV the baryonic and neutrino effects are comparable, though with different scale dependence,

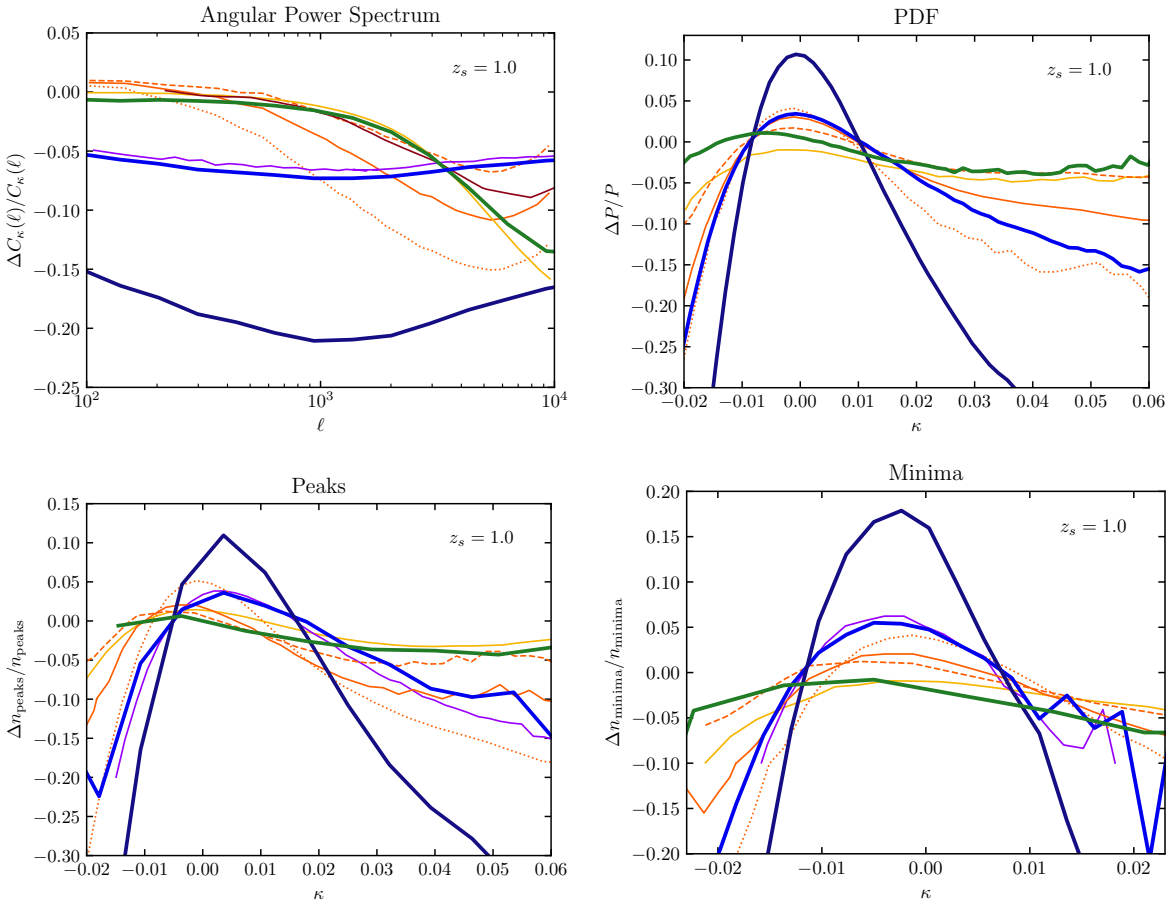

Color	Simulation	Code	Box size $[h^{-1}\text{Mpc}]$	$N_{\rm CDM}$	$\sum m_\nu$ [eV]	h	Ω_m	Ω_b	σ_8
	MTNG740-1	Arepo	500	4320^3	-	0.6774	0.3089	0.0486	0.8159
	MTNG630-DM-0.1	Gadget-4	430	2160^3	0.1	0.68	0.306	0.0487	0.8040
	MTNG630-DM-0.3	Gadget-4	430	2160^3	0.3	0.68	0.306	0.0487	0.7623
	TNG300-1	Arepo	205	2500^3	-	0.6774	0.3089	0.0486	0.8159
	Bahamas	Gadget-3	400	1024^3	-	0.7	0.2793	0.0463	0.821
	Horizon AGN	Ramses	100	1024^3	-	0.704	0.272	0.045	0.81
	MassiveNuS	Gadget-2	512	1024^3	0.1	0.7	0.3	0.046	0.8295

Figure 3.10: Top left: WL convergence power spectrum; top right: WL convergence PDF; bottom left: WL convergence peak counts; bottom right: WL convergence minimum counts. All the panels show the ratio between a simulation and its DM-only version. Here we compare our findings with those of similar recent studies. The results concerning baryonic effects are from MTNG (green), TNG (yellow), HorizonAGN (brown), and Bahamas (orange); Bahamas comes in three different AGN intensities: low (dashed line), fiducial (solid line), and high (dotted line). The results concerning massive neutrinos are from MTNG with $\sum m_\nu = 0.1$ eV (blue), MTNG with $\sum m_\nu = 0.3$ eV (dark blue), and MassiveNuS (purple).

Table 3.2: Overview of the fractional differences between our results and those from other simulations for the four observables considered in this study: WL convergence power spectrum, PDF, peak counts, and minima counts. The values of the table are computed based on the results shown graphically in Figure 3.10.

Simulation	$C(\ell)$		PDF		Peaks		Minima	
	$\ell = 10^3$	$\ell = 10^4$	$\kappa = 0$	$\kappa = 0.05$	$\kappa = 0$	$\kappa = 0.05$	$\kappa = 0$	$\kappa = -0.02$
Baryons								
TNG300-1	< 0.01	0.03	0.02	0.01	0.01	0.01	< 0.01	0.05
Bahamas low AGN	< 0.01	0.09	0.01	< 0.01	< 0.01	< 0.01	0.03	0.02
Bahamas fiducial	0.02	0.05	0.02	0.05	0.02	0.04	0.04	0.10
Bahamas high AGN	0.06	0.01	0.03	0.12	0.05	0.12	0.06	0.22
Horizon AGN	< 0.01	0.05	/	/	/	/	/	/
Massive neutrinos								
MassiveNuS	< 0.01	< 0.01	/	/	< 0.01	0.03	< 0.01	/

highlighting that these effects are partly degenerate.

For the power spectra, the suppression induced by baryonic physics is negligible compared to that induced by neutrinos with $\sum m_\nu = 0.1$ eV for angular scales $\ell < 2000$, but becomes dominant on smaller angular scales $\ell > 4000$. In the case of the PDF, peak counts, and minimum counts, we see that even a total neutrino mass of $\sum m_\nu = 0.1$ eV produces distortions that are larger than those induced by baryonic physics, especially in the tails of the distributions.

A crucial test to validate the reliability of results coming from numerical experiments is the comparison between independent simulation studies. In Figure 3.10 results from previous studies are indicated by the thinner lines, yellow, brown, and orange referring to the baryonic effects computed for IllustrisTNG (Osato et al., 2021), HorizonAGN (Gouin et al., 2019), and Bahamas (Coulton et al., 2020), respectively. This last simulation project considered three different models with increasingly strong AGN feedback: these are indicated by dashed (*low*) solid (*fiducial*) and dotted (*high*) lines. In purple, we include the result reported for massive neutrinos with $\sum m_\nu = 0.1$ eV for the MassiveNuS simulations, where the angular power spectrum effects were computed by Liu & Madhavacheril (2019), and the peak and minimum counts were computed in Coulton et al. (2020).

Focusing first on the comparison with previous results for $\sum m_\nu = 0.1$ eV neutrinos, we see that our angular power spectrum modification agrees to $\approx 1\%$ with that of MassiveNuS at all angular scales. For the peak and minimum counts, we also find a reassuring $\approx 1 - 2\%$ agreement for all values of κ other than the high-κ tails, where some statistical fluctuations are present. This exemplifies the robustness of such neutrino predictions, provided a sufficiently accurate simulation methodology is employed. This agrees with conclusions from the recent neutrino simulation code comparison project of Adamek et al. (2022).

Next, considering the impact of baryons as predicted by different studies, we can directly compare the power spectrum modification we measure to results from the three independent

projects included in Figure 3.10. We find a $\approx 1-2\%$ agreement up to $\ell \approx 4000$ between MTNG and IllustrisTNG, HorizonAGN, and the 'low AGN' variant of Bahamas. At smaller angular scales, we see that MTNG and TNG predict a suppression that is of the same order as that in the high AGN variant of Bahamas; for $\ell \approx 10^4$, this is stronger by roughly a factor of two than the predictions of HorizonAGN and of the low and fiducial AGN versions of BAHAMAS. Clearly the predictions are strongly affected by the specific implementation of feedback for $\ell > 10^3$. Even at $\ell = 10^3$ the fiducial version of Bahamas predicts a 3% effect, which is more than twice that found in the other models.

Moving to the PDF, we find $\approx 2\%$ agreement between MTNG, TNG, and the Bahamas's low-AGN model, the only exception being for $\kappa \lesssim 0.01$, where our results predict a milder suppression of the tails. The fiducial and high AGN versions of Bahamas deviate substantially, predicting a more extreme narrowing of the PDF. It is interesting to observe that these two cases become quite close to the effects seen for massive neutrinos with $\sum m_\nu = 0.1$ eV. Similar conclusions can be drawn concerning the peak and minimum distributions, where we agree at $\approx 5\%$ with TNG, and the low-AGN version of Bahamas. Here also, the Bahamas's fiducial and (especially) high AGN models differ substantially, and are quantitatively closer to the results for the $\sum m_\nu = 0.1$ eV neutrino case. As a summary of this discussion, we explicitly quantify the deviation between our results and the ones from other numerical studies in Table 3.2.

Overall, our results reaffirm the strong sensitivity of WL observables to AGN feedback physics, and they also point out an important partial degeneracy between the impacts of massive neutrinos and baryonic physics. At the same time, the comparatively good agreement between different simulation methodologies can be seen as encouraging, underlining the predictive power of the simulations far into the non-linear regime, even though the high systematic uncertainty in the strength of AGN feedback clearly remains a point of concern.

3.5 Conclusions and outlook

In this chapter, we introduced our methodology for computing full-sky maps of weak lensing convergence, starting from the mass-shell outputs of Gadget-4. We applied our code to a selection of simulations from the MillenniumTNG suite, presenting predictions for four observables, namely the angular power spectrum, the one-point PDF, and counts of peaks and minima as a function of convergence.

After assessing the internal consistency of our code by comparing our results to theoretical predictions, we investigated the impact of mass and angular resolution on the weak lensing convergence, finding low angular resolution to be particularly problematic. Even if the underlying simulation has high mass resolution, insufficient angular resolution causes significant suppression of the angular power spectrum at small scales, as well as a narrowing of the one-point PDF and an underprediction of the number of peaks and minima at all values of the WL convergence. Creating convergence maps featuring high angular resolution is therefore of critical importance, arguably even more important than the underlying mass

resolution. We also tested whether the "fixed and paired" variance-suppression technique proposed by Angulo & Pontzen (2016) remains beneficial when applied to continuous light-cone output over a wide redshift range, rather than to individual simulation snapshots. We found that it does indeed significantly reduce cosmic variance uncertainties in the angular power spectrum of WL convergence at medium to large ℓ-values.

We investigated the impact of baryonic physics on WL measurements by comparing convergence maps from DM-only and full-hydro simulations run from identical initial conditions. We found that including the baryons results in a redshift-dependent suppression of angular power which can reach $\approx 15\%$ for $\ell \gtrsim 10^3$. The PDF in turn becomes narrower, increasingly so for higher source redshift, while the counts of peaks and minima are suppressed in an κ-dependent fashion by up to $\approx 15\%$. This emphasizes the need to include the impact of baryons in any attempt to model WL observables with high precision.

We also studied the effect of massive neutrinos on WL observables by comparing simulations with different total neutrino masses, viz. $\sum m_\nu = [0, 100, 300]\,\mathrm{meV}$. The impact is significant, and is especially drastic for $\sum m_\nu = 300\,\mathrm{meV}$, producing a suppression of the angular power spectrum by up to $\approx 20\%$, and inducing a significant distortion of the PDF and of the distributions of peak and minimum counts, primarily a suppression of the tails and an enhancement of the central parts of the distributions.

In summary, weak lensing predictions of the precision needed to interpret stage IV surveys *require* appropriate modeling of the impact *both* of baryonic physics and of massive neutrinos. Furthermore, these must be implemented in simulations which simultaneously have *both* sufficiently high angular and mass resolution *and* large enough periodic box size. In the present study, we adopted a purely theoretical perspective, focusing exclusively on the mass distributions predicted by the MTNG simulations. However, this simulation suite also predicts the properties of the galaxies themselves, either directly in the large hydrodynamical simulation MTNG740, or through semi-analytic modeling throughout the extremely large-volume DM-only simulation MTNG3000 (which also includes massive neutrinos). Forthcoming work will thus consider realistic forward modeling of weak lensing observations in order to study various correlations between the WL signals and the galaxy distribution.

Chapter 4

Ray-tracing vs. Born approximation in full-sky weak lensing simulations of the MillenniumTNG project

The content of this chapter has been published in the Monthly Notices of the Royal Astronomical Society, Volume 533, Issue 3, September 2024, Pages 3209–3221, and reported here with slight modifications.

Abstract

Weak gravitational lensing is a powerful tool for precision tests of cosmology. As the expected deflection angles are small, predictions based on non-linear N-body simulations are commonly computed with the Born approximation. Here we examine this assumption using DORIAN, a newly developed full-sky ray-tracing scheme applied to high-resolution mass-shell outputs of the two largest simulations in the MillenniumTNG suite, each with a 3000 Mpc box containing almost 1.1 trillion cold dark matter particles in addition to 16.7 billion particles representing massive neutrinos. We examine simple two-point statistics like the angular power spectrum of the convergence field, as well as statistics sensitive to higher-order correlations such as peak and minimum statistics, void statistics, and Minkowski functionals of the convergence maps. Overall, we find only small differences between the Born approximation and a full ray-tracing treatment. While these are negligibly small at the power spectrum level, some higher-order statistics show more sizable effects; ray-tracing is necessary to achieve percent-level precision. At the resolution reached here, full-sky maps with 0.8 billion pixels and an angular resolution of 0.43 arcmin, we find that interpolation accuracy can introduce appreciable errors in ray-tracing results. We therefore implemented an interpolation method based on nonuniform fast Fourier transforms (NUFFT) along with more traditional methods. Bilinear interpolation introduces significant smoothing, while nearest grid point sampling agrees well with NUFFT, at least for our fiducial source redshift, $z_s = 1.0$, and for the 1 arcmin smoothing we use for higher-order statistics.

4.1 Introduction

Accurately computing the statistics mentioned in Section 1.2.2, either numerically or analytically, is a significant challenge, as many approximations need to be employed. A non-exhaustive list of assumptions often made in numerical WL experiments includes: the Limber and flat-sky approximations (Lemos et al., 2017); the projection of 3D mass distributions into infinitely thin planes, i.e. the thin lens approximation (Frittelli & Kling, 2011; Parsi Mood et al., 2013; Zhou et al., 2024); neglecting higher-order image distortions beyond convergence and shear, e.g. flexions (Schneider & Er, 2008); the use of DM-only simulations rather than including full baryonic physics (Semboloni et al., 2011; Yang et al., 2013; Osato et al., 2021; Broxterman et al., 2024; Ferlito et al., 2023); and simplifying assumptions for the sample redshift distribution $n(s)$ (Zhang et al., 2023).

Finally, one of the most common approximations used in calculating WL from simulations is the Born approximation. This assumes that the perturbations to the light path induced by gravitational lensing are negligible, so that it can be well approximated by an undeflected straight line. Carrying out a WL simulation in the Born approximation requires significantly less memory and computational effort than tracing the paths of rays explicitly (see e.g., Petri et al., 2017), making it particularly attractive. The accuracy of the Born approximation in WL simulations has previously been studied for square maps (Petri et al., 2017), and, in the case of lensing of the cosmic microwave background (CMB), also for full-sky maps (Fabbian et al., 2018). These studies have shown its impact to be effectively negligible at the level of the power spectrum (see also e.g., Fabbian et al., 2019; Hilbert et al., 2020). Nevertheless, it has also been found to have a non-negligible impact on higher moments of the convergence PDF; i.e. the skewness and kurtosis (Petri et al., 2017; Fabbian et al., 2018; Barthelemy et al., 2020).

In this chapter, we revisit this question and develop a full-sky ray-tracing scheme that works on the lightcone mass-shell outputs produced by the GADGET-4 code (Springel et al., 2021) for the MillenniumTNG simulation suite. This allows us to explicitly test the Born approximation, not only on the power spectrum and PDF, but also on a set of popular higher-order statistics: counts of peaks and minima, the abundance and profiles of voids, and Minkowski functionals.

This chapter is organized as follows. In Section 4.2, we describe the numerical simulations and methods employed in this work. We first introduce the simulations and relative data products employed (Sec. 4.2.1), we discuss our implementation of a ray-tracing scheme (Sec. 4.2.2), and we then focus on the spherical harmonics relations (Sec. 4.2.3) and the interpolation schemes (Sec. 4.2.4) used. At the end of the section, we provide additional details relevant to the computation of observables (Sec. 4.2.5). In Section 4.3, after a qualitative discussion of our full-sky maps, we show the impact of ray-tracing on the following statistics: the angular power spectrum (Sec. 4.3.2); the PDF and counts of peaks and minima of the convergence (Sec. 4.3.3, 4.3.4); void statistics (Sec. 4.3.5); and Minkowski functionals (Sec. 4.3.6). Finally, in Section 4.4 we summarize our conclusions, and in Appendix B we discuss in further detail the effects caused by bilinear interpolation.

4.2 Methods

4.2.1 Simulations

The simulations used in this work are a subset of the MillenniumTNG (MTNG) project, introduced in Section 3.2.1. In order to avoid repetitions of the simulation volume along the line of sight and to maximize statistical robustness, we employ the simulations of the MTNG suite, which feature the biggest box size together with the highest particle number. These are the A- and B-realizations of the N-body cosmological run MTNG3000-DM-0.1ν, which feature dark matter (DM) and massive neutrinos with a summed mass of $\Sigma m_\nu = 100\,\mathrm{meV}$.

In continuation of Ferlito et al. (2023), the main simulation product of interest for WL applications is the "mass-shell" output: a collection of concentric HEALPix maps (Górski et al., 2005) produced during the simulation on the fly in an onion-like fashion with fixed comoving thickness. For each shell, every pixel stores the cumulative mass of particles intersecting the time-evolving hypersurface of the lightcone of a putative observer. In the present work, we use a HEALPix parameter of $N_{\mathrm{side}} = 8192$, corresponding to 8.053×10^8 pixels and an angular resolution of 0.43 arcmin.

4.2.2 Implementation of ray-tracing

Our ray-tracing implementation, dubbed DORIAN[1], is a `Python` code based on the multiple-lens-plane approximation (e.g., Blandford & Narayan, 1986; Schneider et al., 1992; Jain et al., 2000), which has been adopted in a number of codes (see e.g., Hilbert et al., 2009; Becker, 2013; Petri, 2016; Fabbian et al., 2018). In our setup, each mass-shell (as described in the previous section), here labeled with an index k, constitutes a thin lens. The surface mass density distribution of the lens is given by

$$\Sigma^{(k)}(\boldsymbol{\beta}) = \frac{M(\boldsymbol{\beta})}{A_{\mathrm{pix}}}\,. \tag{4.1}$$

This is obtained by dividing the mass assigned to each pixel by the pixel area $A_{\mathrm{pix}} = 4\pi/N_{\mathrm{pix}}$ (in steradians). Using equation (2.7), we can compute an approximation of the convergence at the k^{th} lens plane as:

$$\kappa^{(k)}(\boldsymbol{\beta}) = \frac{4\pi \mathrm{G}}{\mathrm{c}^2} \frac{(1+z_{\mathrm{d}}^{(k)})}{f_K^{(k)}} \left[\Sigma^{(k)}(\boldsymbol{\theta}) - \bar{\Sigma}^{(k)}\right]\,, \tag{4.2}$$

where ${f^{(k)}}_K = f_K(\chi_{(k)})$. We introduce the lensing potential ψ as the 2-D projection of the Newtonian gravitational potential onto the k^{th} lens surface:

$$\psi^{(k)}(\boldsymbol{\beta}) = \frac{2}{c^2 f_K^{(k)}} \int_{\chi_k - \Delta\chi/2}^{\chi_k + \Delta\chi/2} \Phi(\boldsymbol{\beta}) \mathrm{d}\chi, \tag{4.3}$$

[1] Acronym for "Deflection Of Rays In Astrophysical Numerical simulations".

where $\Delta\chi$ is the comoving thickness of each shell. The above quantity is related to $\kappa^{(k)}$ through the Poisson equation:

$$\nabla^2_{\boldsymbol{\beta}}\psi^{(k)}(\boldsymbol{\beta}) = 2\kappa^{(k)}(\boldsymbol{\beta})\,, \tag{4.4}$$

where $\nabla^2_{\boldsymbol{\beta}}$ is the Laplacian operator. The multiple lens plane approximation neglects modes along the line of sight larger than the shell thickness, and therefore is expected to become unreliable as the lens planes become too thin (Das & Bode, 2008). This motivates us to set the shell thickness to $\Delta\chi = 100\,h^{-1}$Mpc in the present work (see also Zorrilla Matilla et al., 2020). We refer the reader to section 2.2 of Becker (2013) and appendix B of Takahashi et al. (2017) for a more detailed discussion.

By taking the first derivative of the lensing potential, one obtains the deflection angle at the $k^{\rm th}$ lens plane:

$$\boldsymbol{\alpha}^{(k)}(\boldsymbol{\beta}) = \frac{\partial\psi^{(k)}(\boldsymbol{\beta})}{\partial\beta_i}\,. \tag{4.5}$$

The second derivatives of the lensing potential give the shear matrix U at the $k^{\rm th}$ lens plane:

$$U^{(k)}_{ij}(\boldsymbol{\beta}) = \frac{\partial^2\psi^{(k)}(\boldsymbol{\beta})}{\partial\beta_i\partial\beta_j} = \frac{\partial\alpha^{(k)}_i(\boldsymbol{\beta})}{\partial\beta_j}\,. \tag{4.6}$$

We note that, since we are dealing with quantities on the curved sky, partial derivative operators are promoted to covariant derivatives (Becker, 2013). We have now introduced all the quantities needed for a numerical implementation of equations (2.3) and (2.4). In particular, the integrals can be carried out as a discrete summation over N spherical lens planes, which leads to the following expressions for $\boldsymbol{\beta}$ and A, respectively:

$$\boldsymbol{\beta}^{(N)}(\boldsymbol{\theta}) = \boldsymbol{\theta} - \sum_{k=0}^{N-1}\frac{f_K^{(k,N)}}{f_K^{(N)}}\boldsymbol{\alpha}^{(k)}(\boldsymbol{\beta}^{(k)})\,, \tag{4.7}$$

$$A^{(N)}_{ij}(\boldsymbol{\theta}) = \delta_{ij} - \sum_{k=0}^{N-1}\frac{f_K^{(k,N)}}{f_K^{(N)}}U^{(k)}_{il}A^{(k)}_{lj}\,, \tag{4.8}$$

where $f_K^{(k,N)} \equiv f_K(\chi^{(N)} - \chi^{(k)})$.

Using the above formulae with high-resolution maps would, however, require a large number of operations, and most importantly, the memory needs would be prohibitively large. Hilbert et al. (2009) reformulated these equations to allow the quantities to be calculated with an iterative procedure that requires only information about the previous two lens planes:

$$\begin{aligned}\boldsymbol{\beta}^{(k+1)} = &\left(1 - \frac{f_K^{(k)}}{f_K^{(k+1)}}\frac{f_K^{(k-1,k+1)}}{f_K^{(k-1,k)}}\right)\boldsymbol{\beta}^{(k-1)}\\ &+ \frac{f_K^{(k)}}{f_K^{k+1}}\frac{f_K^{(k-1,k+1)}}{f_K^{(k-1,k)}}\boldsymbol{\beta}^{(k)} - \frac{f_K^{(k,k+1)}}{f_K^{(k+1)}}\boldsymbol{\alpha}^{(k)}(\boldsymbol{\beta}^{(k)})\,,\end{aligned} \tag{4.9}$$

$$A_{ij}^{(k+1)} = \left(1 - \frac{f_K^{(k)}}{f_K^{(k+1)}} \frac{f_K^{(k-1,k+1)}}{f_K^{(k-1,k)}}\right) A_{ij}^{(k-1)} + \frac{f_K^{(k)}}{f_K^{k+1}} \frac{f_K^{(k-1,k+1)}}{f_K^{(k-1,k)}} A_{ij}^{(k)} - \frac{f_K^{(k,k+1)}}{f_K^{(k+1)}} U_{il}^{(k)} A_{lj}^{(k)} \,. \tag{4.10}$$

Here the initial conditions at the first lens plane are set to $\boldsymbol{\beta}^{(-1)} = \boldsymbol{\beta}^{(0)} = \boldsymbol{\theta}$ and $A_{ij}^{(-1)} = A_{ij}^{(0)} = \delta_{ij}$; i.e. we perform backward-in-time ray-tracing from the observer to the source plane.

As noted by Becker (2013), when working with spherical lens planes, one has to parallel transport the distortion matrix (a tensor on the sphere) along the geodesic connecting the angular positions of the ray at consecutive planes, which takes into account the change in the local tensor basis.

4.2.3 Spherical harmonics relations

Since we are working with full-sky maps, the optimal way to compute the derivatives in equations (4.5) and (4.6) is by performing them in the spin-weighted spherical harmonics domain (see Varshalovich et al., 1988, for a standard reference). In this section, we will discuss how we compute $\boldsymbol{\alpha}$ and U at each lens plane by making use of the relations derived in Hu (2000).

Once κ, a spin-0 (i.e. scalar) quantity, is computed from equation (4.2) (in this section we omit the superscript k for clarity), we can obtain its spherical harmonic coefficients $\kappa_{\ell m}$ using the HEALPix `map2alm` routine. The key relation is then:

$$\kappa(\boldsymbol{\beta}) = \sum_{\ell=0}^{\infty} \sum_{m=-\ell}^{\ell} \kappa_{\ell m} Y_l^m(\boldsymbol{\beta}) \,, \tag{4.11}$$

where Y_l^m are the spin-0 spherical harmonics. The Poisson equation on the surface of the sphere, i.e. equation (4.4), takes the following form in the spherical harmonics domain:

$$\kappa_{\ell m} = -\frac{\ell(\ell+1)}{2} \psi_{\ell m} \,, \tag{4.12}$$

while the derivative in equation (4.5) yields the spin-1 (i.e. tangential vector) field:

$$\alpha_{lm} = -\sqrt{\ell(\ell+1)} \psi_{\ell m} \,. \tag{4.13}$$

We point out that one can skip the computation of the potential and obtain the deflection field directly from the convergence by combining equations (4.12) and (4.13):

$$\alpha_{lm} = \frac{2}{\sqrt{\ell(\ell+1)}} \kappa_{\ell m} \,. \tag{4.14}$$

Regarding the shear matrix, we combine equations (7) and (8) of Castro et al. (2005), yielding:

$$U_{ij}(\boldsymbol{\beta}) = \kappa(\boldsymbol{\beta})\delta_{ij} + [\gamma_1(\boldsymbol{\beta})\sigma_3 + \gamma_2(\boldsymbol{\beta})\sigma_1]_{ij} \,, \tag{4.15}$$

where σ_1 and σ_3 are the Pauli matrices. Therefore, the only additional quantity we need to obtain for the shear matrix is the shear, a spin-2 quantity which can be computed from κ as follows:

$$\gamma_{lm} = -\sqrt{(\ell+2)(\ell-1)/(\ell(\ell+1))}\kappa_{\ell m} \,, \tag{4.16}$$

under the assumption that the B-modes of the shear (which have comparable power to the rotation) can be neglected (see e.g., Hadzhiyska et al., 2023).

4.2.4 Interpolation on HEALPix maps

As one can see from equations (4.9) and (4.10), $\boldsymbol{\alpha}^{(k)}$ and $U^{(k)}$ have to be evaluated at the angular position $\boldsymbol{\beta}^{(k)}$ for each ray, which in general will not coincide (apart from the first iteration) with the center of a HEALPix pixel. A classic approach to this problem consists of transforming the quantities back to real space with the HEALPix `alm2map_spin` routine, and then performing interpolation in the resulting maps, with the simplest choices being Nearest Grid Point (NGP, e.g., Fabbian et al., 2018) and bilinear (e.g., Broxterman et al., 2024) interpolation. The first is faster but less precise, while the second is in principle more precise, but at the cost of being slower and introducing significant smoothing. We discuss the impact of the additional effective smoothing from bilinear interpolation in Appendix B.

A novel, more accurate and faster approach, based on the nonuniform fast Fourier transform (NUFFT, cf. Fessler & Sutton 2003; Barnett et al. 2019) algorithm, has been efficiently implemented in the context of gravitational lensing by Reinecke et al. (2023). The idea is to accurately synthesize the fields at the desired angular positions by first computing a map on an equiangular grid from the spherical harmonic coefficients using a conventional spherical harmonic transform algorithm, then extending this map to 2π in the θ direction (which results in a map that is periodic along both coordinate axes), and finally interpolating the result to the desired locations using non-uniform FFTs.

In this work, we will compare NGP, bilinear, and NUFFT interpolated ray-tracing simulations to the Born approximation. This will allow us to evaluate not only the impact of ray-tracing as opposed to the Born approximation, but also to capture and study the differences between the three different interpolation schemes employed.

4.2.5 Computation of the WL statistics

The power spectra are computed with the HEALPix routine `anafast`, and binned into 80 equally spaced logarithmic bins in the range $\ell \in [1, 2.5 \times 10^4]$. Before computing all the other statistics, every map is smoothed with the HEALPix `smoothing` routine with a Gaussian symmetric beam characterized by a standard deviation of 1 arcmin, consistent with Ferlito et al. (2023) and with other similar studies. For the convergence PDF, we bin all pixels in 100 linearly spaced bins in the range $\kappa \in [-0.15, 0.25]$. Peaks and minima are

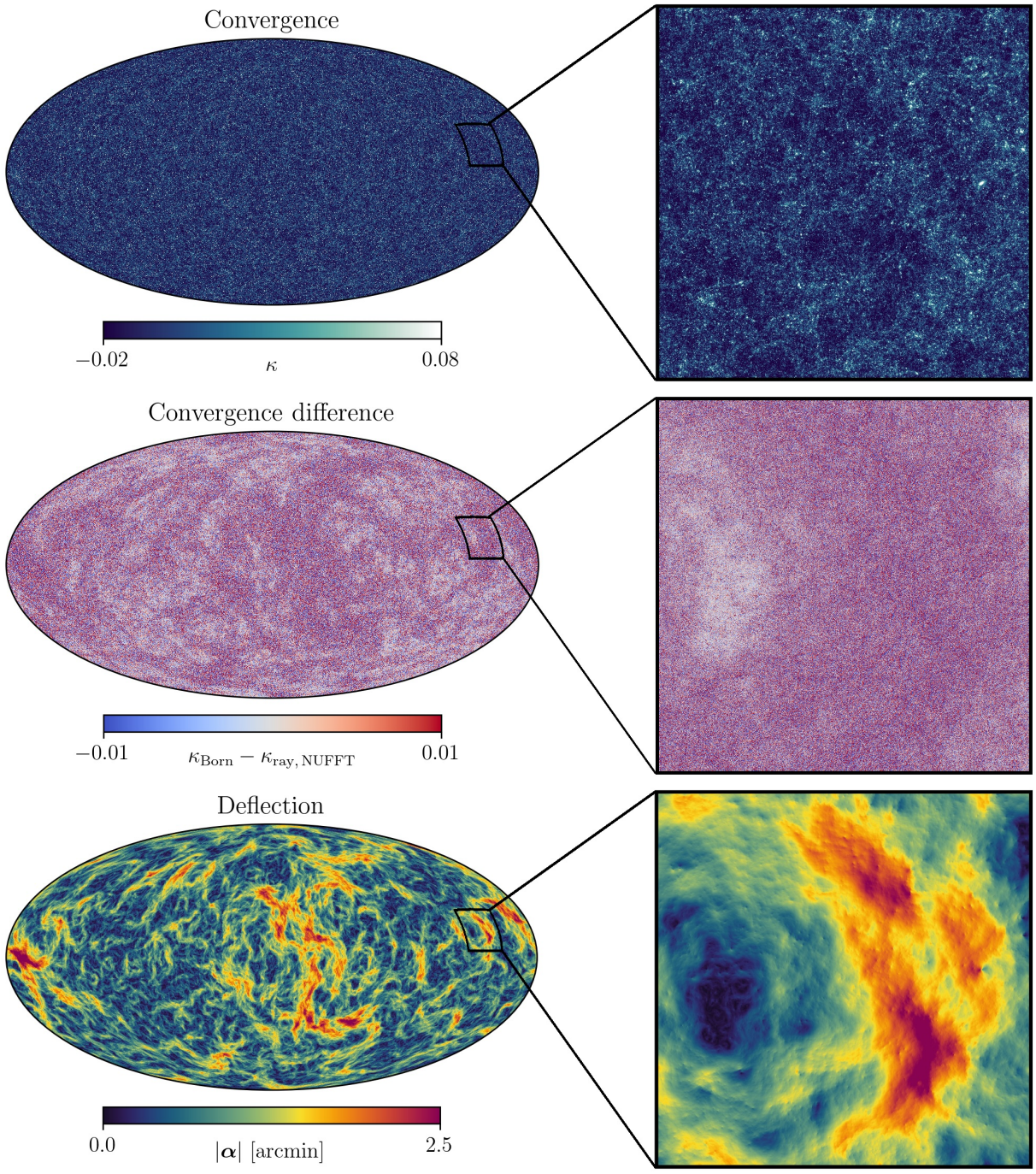

Figure 4.1: *Top row:* convergence field computed with our ray-tracing code using NUFFT interpolation. *Middle row*: difference of the convergence field when computed with ray-tracing instead of the Born approximation. *Bottom row:* amplitude of the deflection field $\boldsymbol{\alpha}$, computed as the difference between the observed angular position $\boldsymbol{\theta}$ and the original angular position $\boldsymbol{\beta}$. In each case, the panels on the right-hand side show enlargements with a size of 10 degrees on a side. They may also be compared to the corresponding regions in the fields shown in Figure 4.2.

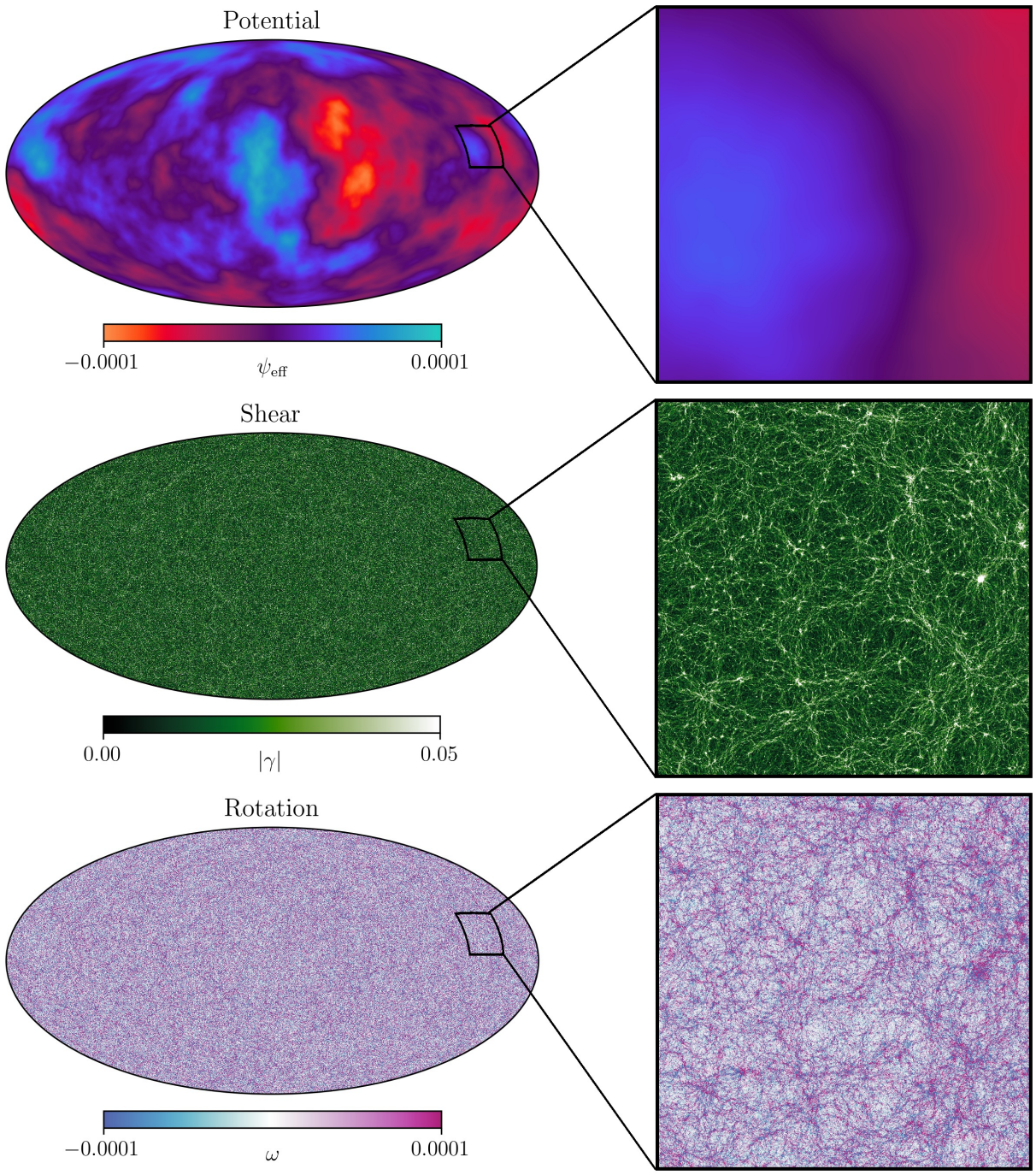

Figure 4.2: *Top row:* effective lensing potential, computed by plugging the convergence field into equation (4.12). *Middle row*: shear field amplitude $|\gamma| = \sqrt{\gamma_1^2 + \gamma_2^2}$. *Bottom row:* rotation field. All quantities were computed with our ray-tracing code using NUFFT interpolation. In each case, the panels on the right-hand side show enlargements with a size of 10 degrees on a side. They may also be compared to the corresponding regions in the fields shown in Figure 4.1.

computed as the pixels that are, respectively, greater or smaller than their 8 neighbours[2], which are retrieved using the HEALPix `get_all_neighbours` routine. For the peaks, we set 25 linearly spaced bins in the range $\kappa \in [-0.04, 0.2]$, while for the minima 30 linearly spaced bins in the range $\kappa \in [-0.045, 0.045]$ are used. Void statistics were computed following Davies et al. (2018). In particular, for the void abundance, we set 25 linearly spaced bins in the range $R_v \in [0, 0.2]$ deg where R_v is the void radius, and for the stacked void profiles, we use 20 linearly spaced bins in the range $r/R_v \in [0, 2]$, where r/R_v is the distance from the void center (r) in units of void radius. Finally, Minkowski functionals (MF) were computed with the publicly available Python package PYNKOWSKI (Carones et al., 2024), using 130 linearly spaced bins in the range $\kappa \in [-0.03, 0.11]$. For all of the above statistics, the value at each bin is computed as the average of the A- and B-realizations of our MTNG simulations. In the case of the void profiles and the third MF, in the lower sub-panel of the respective plots, we decided to show the difference with respect to the Born approximation. The reason is that since these two statistics cross the zero value, the ratio would diverge to infinity, making the plot somewhat more difficult to interpret. For all the other statistics, the lower sub-panel shows the ratio with respect to the Born approximation.

4.3 Results

We begin the presentation of our results with an overview of some key quantities produced by our simulations, then move our focus to the impact of the Born approximation on the following WL statistics: power spectrum, PDF, Peaks, Minima, Void statistics, and Minkowski functionals. For definiteness, all the WL statistics in the present work are computed assuming a source redshift of $z_s = 1.0$.

4.3.1 Overview of WL quantities

Figures 4.1 and 4.2 show maps of some essential WL quantities, as computed with our ray-tracing code using the NUFFT interpolation. We start by looking at the amplitude of the deflection field (bottom panel of Figure 4.1), which is defined as the difference between the observed angular position $\boldsymbol{\theta}$ and the original angular position $\boldsymbol{\beta}$. We see that the characteristic angular scale of fluctuations is larger than that of the convergence field (top panel of Figure 4.1): this is expected as the convergence is the derivative with respect to the angular position of the deflection. Features that cause the strongest deflection, i.e. with an intensity $\gtrsim 2$ arcmin (colored in red), reach an angular size of $\approx 5 - 10$ degrees. This reflects the fact that for cosmological WL, the dominant component of the deflection field is generated from the large-scale structure of the Universe, rather than single objects. To better quantify the magnitude of the deflection field, we can look at its PDF in Figure 4.3. We notice that the median deflection that a ray experiences along its path from the source to the observer is ≈ 0.79 arcmin, which is almost twice the angular size of a pixel in

[2]In the HEALPix tessellation, every pixel has 8 neighbors, except for a small minority of pixels, for which it can be 7 or 6.

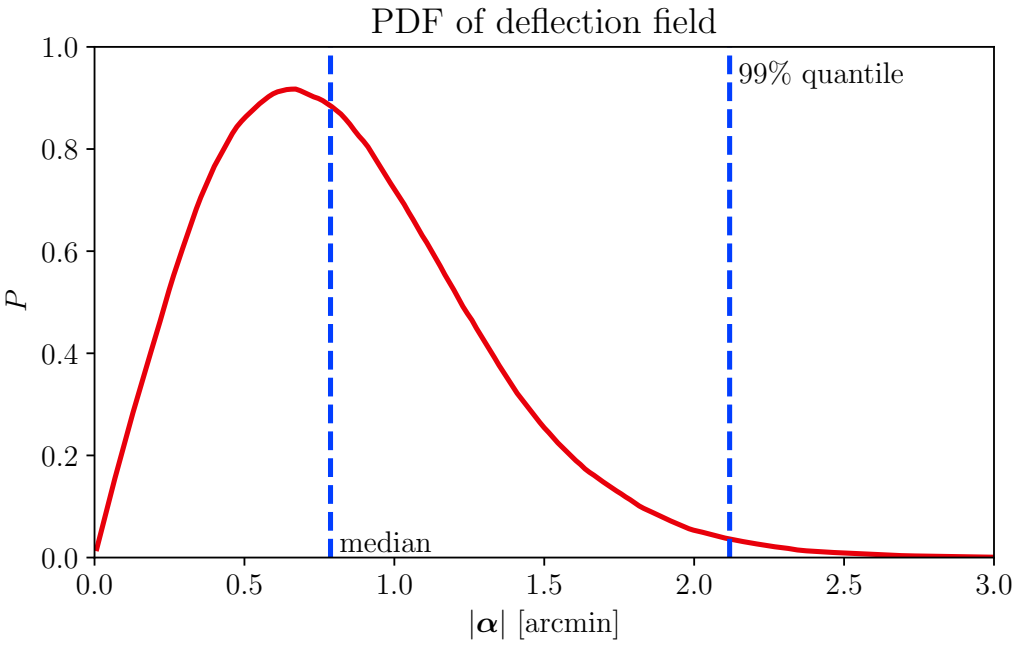

Figure 4.3: PDF of the deflection field $\boldsymbol{\alpha}$, computed with our ray-tracing code using NUFFT interpolation as the difference between the observed angular position $\boldsymbol{\theta}$ and the original angular position $\boldsymbol{\beta}$. The dashed lines indicate the median and the 99% percentile.

our setting. Interestingly, only 1% of the rays experience a deflection greater than ≈ 2.1 arcmin.

By comparing the full-sky map of $|\boldsymbol{\alpha}|$ with the one of the convergence difference (center panel of Figure 4.1), we can perform a qualitative consistency check by noticing that the regions where the rays experience the least deflection (colored from dark blue to black) correspond to the regions where the difference between the Born approximation and ray-tracing is the closest to zero (colored from light grey to white). This becomes even more evident by looking at the zoomed-in region, where a low-deflection region is seen in the left half of the panel.

In the top panel of Figure 4.2, we show the "effective" lensing potential ψ_{eff}, computed by plugging the convergence field (the final product of our code) into equation (4.12). Consistent with theoretical expectations, a flatter potential will correspond to a smaller deflection (e.g. left half of the zoomed panel). Conversely, where the potential has strong variation, the deflection will be greater (e.g. right half of the zoomed panel). Analogously to the relation between convergence and deflection, we notice that the characteristic angular scales of fluctuations of the lensing potential are larger than those of the deflection, which is its derivative with respect to angular position.

In the center and bottom panels of Figure 4.2, we show the shear amplitude $|\gamma| = \sqrt{\gamma_1^2 + \gamma_2^2}$ and the rotation ω, respectively. Both quantities are obtained from the distortion matrix A computed with our ray-tracing code. By looking at the zoomed regions of

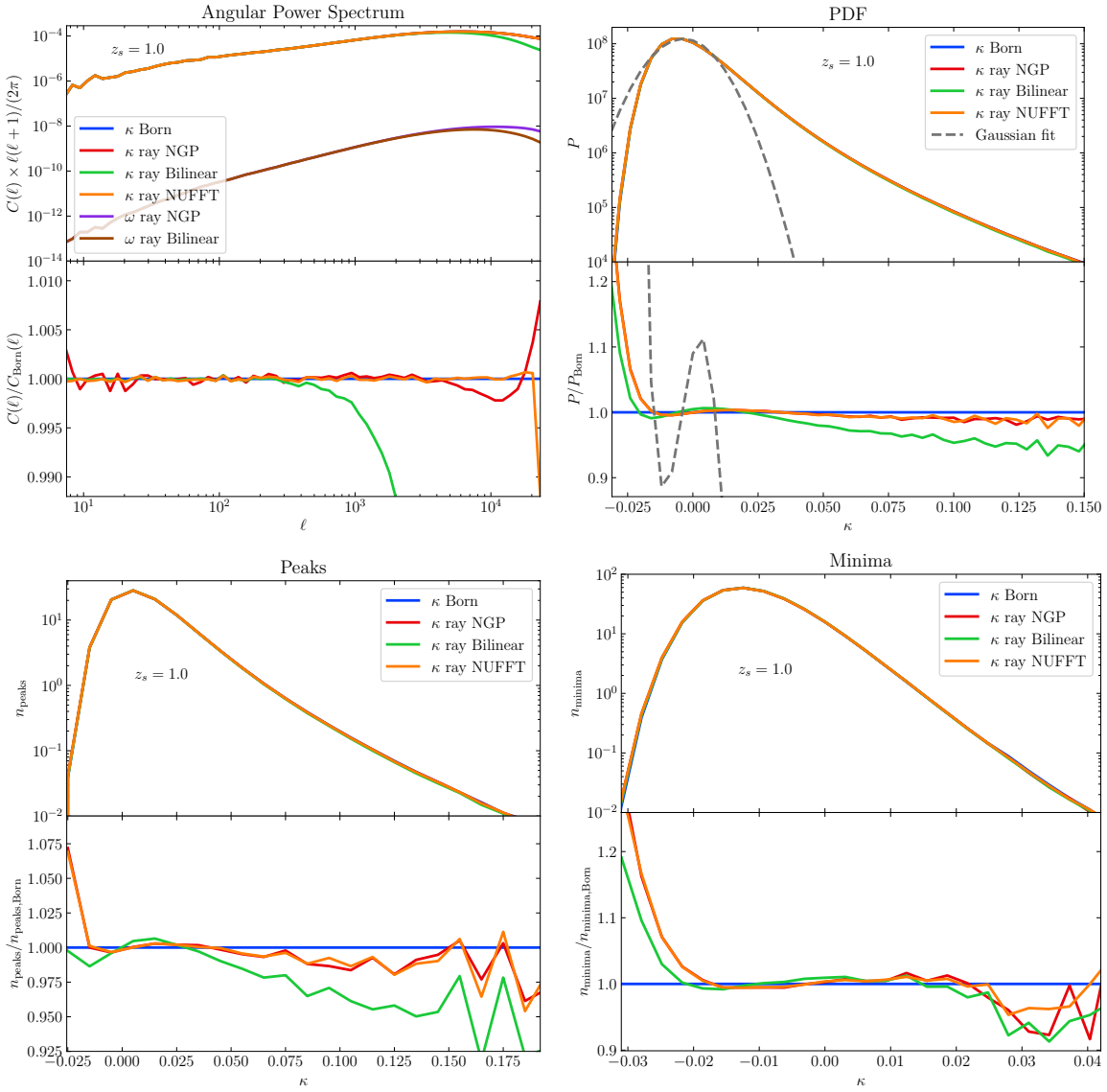

Figure 4.4: *Top left:* angular power spectrum; *top right:* PDF; *bottom left:* WL peak counts; *bottom right:* minimum counts. All the observables are computed adopting a fiducial source redshift of $z_{\rm s} = 1.0$. The statistics are extracted from WL convergence maps computed in the Born approximation (blue), as well as with our ray-tracing code, by using NGP (red), bilinear (green), and NUFFT (orange) interpolation. The lower sub-panel of each plot shows the ratio of these three ray-tracing results with respect to the Born approximation. In the case of the angular power spectrum, we also show the WL rotation computed with the ray-tracing code using NGP (purple) and bilinear (brown) interpolation. In the case of the PDF, we also include a Gaussian fit to the map obtained with the Born approximation (dashed grey). We observe that the power spectrum is not significantly affected by the Born approximation, while the convergence PDF is slightly Gaussianised by ray-tracing, and peaks and minima counts are impacted correspondingly. We also notice that, for all the observables, bilinear interpolation introduces a smoothing that significantly distorts the effects of ray-tracing itself.

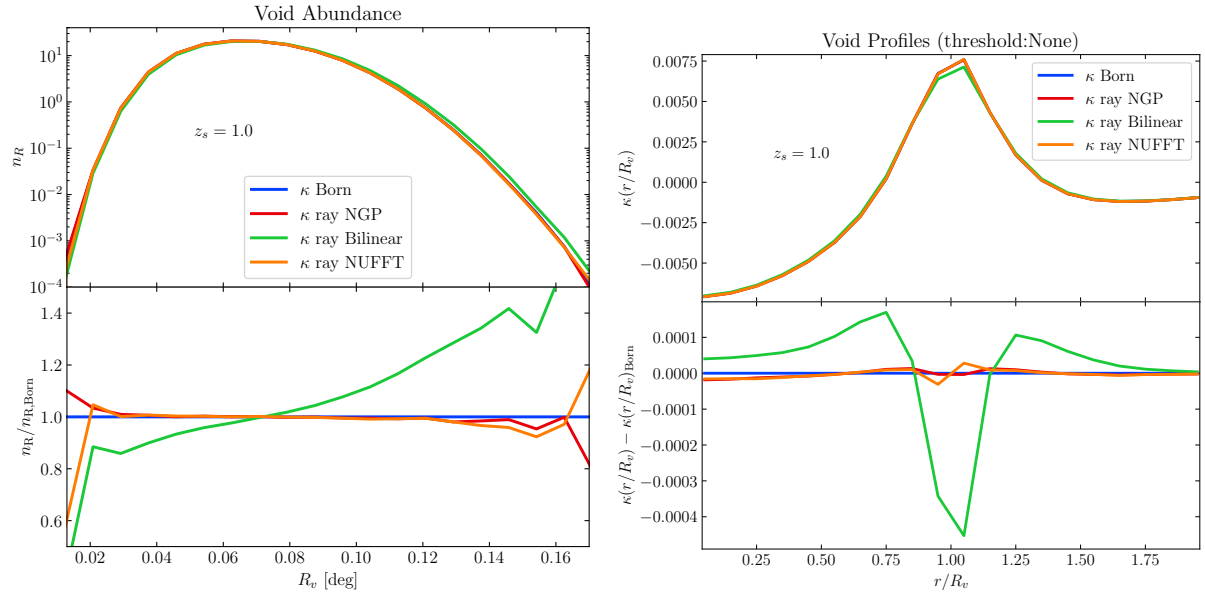

Figure 4.5: *Left:* void abundance distribution; *right left:* stacked void profiles. The statistics are extracted from WL convergence maps computed in the Born approximation (blue), as well as with our ray-tracing code, by using NGP (red), bilinear (green) and NUFFT (orange) interpolation. The maps have a source redshift of $z_\mathrm{s} = 1.0$. The lower sub-panel of each plot shows the ratio (or the difference, in the case of the profiles) of these three ray-tracing results with respect to the Born approximation. Neither statistic is significantly affected by the Born approximation. We also notice that bilinear interpolation introduces a smoothing that moves the void abundance distribution toward larger radii and flattens the void profiles.

convergence and shear, we can recognize the same underlying cosmic structure in both fields. But the two fields show strikingly different features: the convergence field is dominated by a huge number of single objects, which will result in many peaks with different intensities; on the other hand, the shear intensity field shows a more interconnected structure, in which filaments and walls are clearly visible. Finally, we observe that the rotation field shows a very similar morphology to that of the shear intensity field.

4.3.2 Power Spectrum

In the top left panel of Figure 4.4, we show the angular power spectra of WL convergence and rotation. As expected from theoretical predictions, the power of the rotation field is ∼2-3 orders of magnitude smaller than that of the convergence field. The most striking feature that can be observed for both quantities is the progressive power suppression at smaller angular scales. This suppression, observed when the ray-tracing scheme with bilinear interpolation is used, is around $\approx 1\%$ at $\ell \approx 1500$. As we discuss in more detail in Appendix B, this effect is not directly connected to the ray-tracing, but rather arises when performing a series of bilinear interpolations on a HEALPix grid.

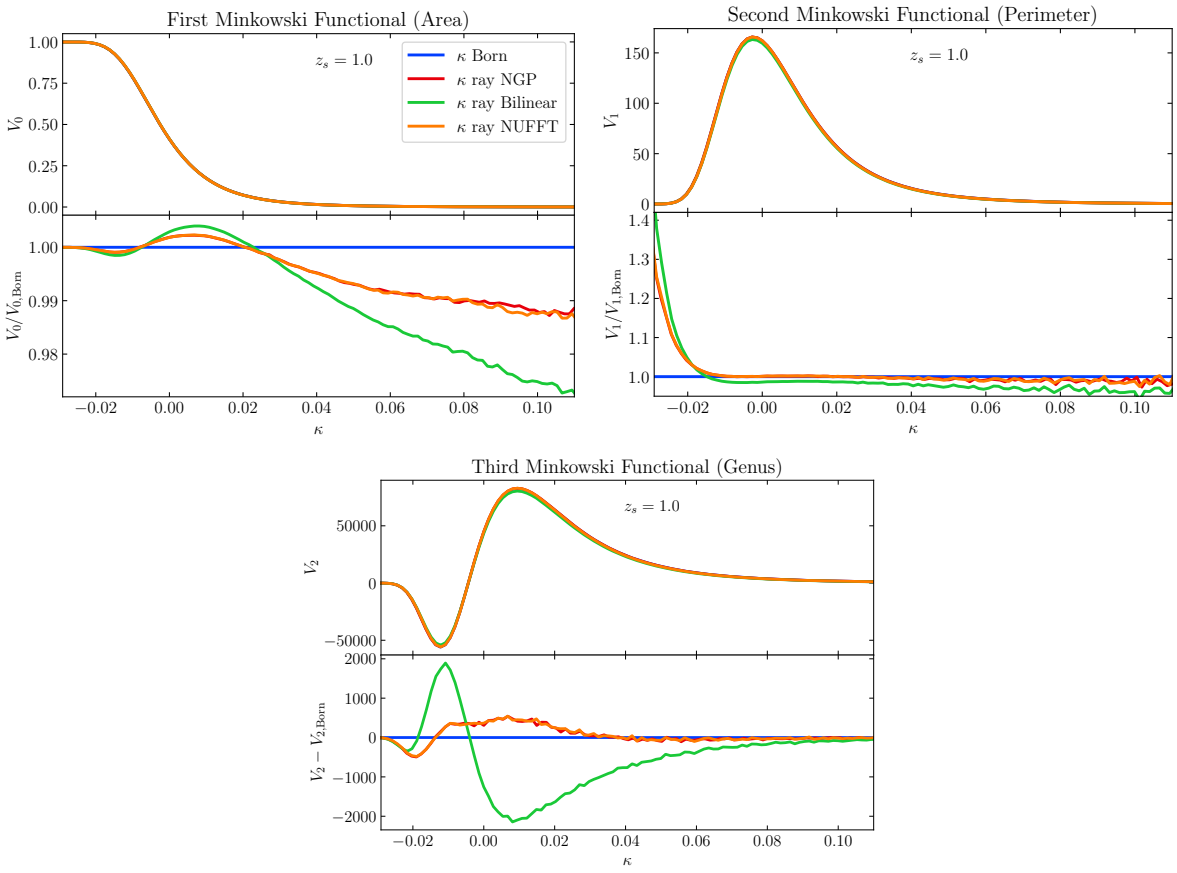

Figure 4.6: *Top:* first Minkowski functional (MF, area); *middle:* second MF (perimeter); *bottom:* third MF (genus). The statistics are extracted from WL convergence maps computed in the Born approximation (blue), as well as with our ray-tracing code, by using NGP (red), bilinear (green), and NUFFT (orange) interpolation. The maps have a source redshift of $z_\mathrm{s} = 1.0$. The lower sub-panel of each plot shows the ratio (or the difference, in the case of the genus) of these three ray-tracing results with respect to the Born approximation. We see that the three MFs are affected to different degrees and that the bilinear interpolation introduces a smoothing that significantly distorts the effects of ray-tracing itself.

Next, in the lower sub-panel, we show the ratio between the convergence spectra with ray-tracing and Born approximation. In the case of ray-tracing performed with NGP interpolation, we see that the fluctuations with respect to the Born approximation never exceed 0.2%, at least until $\ell \approx 10^4$ where we see a suppression of 0.25%, followed by a steep increase in power. This effect, which occurs at approximately the pixel scale, could also be connected to the interpolation scheme. We have verified this by checking that this feature moves to lower multipoles when we decrease the angular resolution of the corresponding HEALPix maps. Finally, in the case of ray-tracing performed with NUFFT interpolation, we see that fluctuations never exceed 0.1% at every scale, until the very last bin, at $\ell \approx 2.3 \times 10^4$, where a $\approx 1\%$ suppression is found.

We conclude that, modulo some $\lesssim 0.2\%$ fluctuations (consistent with Hilbert et al., 2020), the effects on the power spectrum when performing ray-tracing instead of the Born approximation are dominated by the interpolation schemes, rather than from the improved modeling of the physical process. For this reason, NUFFT is found to be a preferable scheme, as it introduces the least power distortions.

4.3.3 Convergence PDF

Having verified that ray-tracing has a negligible impact with respect to the Born approximation at the level of the power spectrum, we next investigate whether this is also true for higher-order statistics. We start with the convergence one-point PDF, shown in the top right panel of Figure 4.4. By looking at the lower sub-panel, which shows the ratio of the ray-tracing schemes to the Born approximation, we see that for NGP and NUFFT the central region is minimally distorted, with deviations never exceeding $\approx 1\%$ in the range $-0.015 < \kappa < 0.07$. Conversely, the outer regions of the distribution exhibit two opposite trends: for $\kappa \gtrsim 0.04$ there is a weak but progressive suppression that reaches $\approx 1.5\%$ at $\kappa \approx 0.09$; for $\kappa \lesssim -0.015$, we see a steep enhancement that reaches $\approx 10\%$ at $\kappa \approx -0.025$. In the case of ray-tracing with bilinear interpolation, there is a larger suppression of the high-κ tail, which reaches $\approx 4\%$ at $\kappa \approx 0.09$, while the steep upturn in the low-κ tail is shifted to smaller values. The discrepancy between this last ray-tracing method and the previous two can be explained by taking into account the smoothing introduced by the bilinear interpolation, which narrows the PDF. We conclude that the Born approximation is likely to mildly overestimate the high-κ tail and significantly underestimate the low-κ part of the PDF.

In contrast to the power spectrum, the features here are not dominated by the interpolation schemes. In particular, a smoothing of the PDF will lead to a suppression at negative κ, whereas we see the opposite in this case. Additionally, while for the power spectrum the three interpolation schemes have noticeably different effects, for the PDF the impact is similar in all cases, indicating that this is driven by a common underlying process.

An interpretation of this result can be given by referring to the leading-order post-Born corrections introduced in equation (2.11). Both the geodesic correction and the lens-lens coupling contribute to making the convergence distribution more Gaussian. This can be directly seen by considering the Gaussian fit (dashed grey line). The former does this by repeatedly displacing the ray positions along directions tangential to the line of sight. The latter by progressively processing the light signal through a system of lenses that are not correlated on sufficiently large scales.

We note that our results found in the case of NGP interpolation are qualitatively consistent with the numerical study of Fabbian et al. (2018) and the theoretical work of Barthelemy et al. (2020). While they found somewhat stronger effects, this is to be expected as they studied CMB lensing.

4.3.4 Peaks and minima

In the bottom left and bottom right panels of Figure 4.4, we show our results regarding peaks and minima counts. In the case of ray-tracing with bilinear interpolation, we observe for both a uniform $\approx 2.5\%$ suppression of the counts of peaks and minima at all values of κ. For a better comparison, this effect was removed in our figures by normalizing the count distributions to unity.

Let us first discuss the peak counts. We see that the overall results are qualitatively similar to what we found for the PDF. In this case, the most relevant effect is the suppression of the high-κ tail, which, in the case of the ray-tracing with NGP and NUFFT interpolation, reaches $\approx 1.5\%$ at $\kappa \approx 0.15$. The additional suppression in the tails of the distribution in the case of ray-tracing with bilinear interpolation is explained by the smoothing that such a scheme introduces.

In the case of the minima counts, we observe that both tails of the distribution are distorted quite significantly. In particular, in the case of ray-tracing with NGP and NUFFT interpolation, the low-κ tail experiences a steep enhancement amounting to $\approx 15\%$ at $\kappa \approx -0.025$, while the high-κ tail is suppressed by $\approx 7\%$ at $\kappa \approx 0.03$. Similarly to the case of the PDF, ray-tracing with bilinear interpolation introduces a delay in the enhancement of the low-κ tail, which can again be explained in terms of the smoothing introduced by the interpolation.

Overall, it is interesting that the effects of Gaussianisation induced by ray-tracing are stronger for minima. This appears clearer by noting that the red and orange curves (NGP and NUFFT respectively) are the ones deviating more from the Born approximation, while, in the case of the peaks, it is the green curve (bilinear) that has the stronger deviation, indicating that the smoothing from bilinear interpolation is dominating over the post-Born effects.

4.3.5 Void statistics

We continue our investigation by considering WL tunnel voids, a WL higher-order statistic that is sensitive to extended underdense regions and has been shown to have promising constraining power on cosmological parameters (Davies et al., 2021). The voids are defined as large underdense regions in the convergence field. The void-finding method used here is the tunnel algorithm, which identifies the largest circles that are empty of suitably defined tracers. In the present case, the tracers are the WL peaks of the convergence field. The corresponding void abundance and profiles are shown in the left and right panels of Figure 4.5, respectively.

From the void abundance, we find that ray-tracing with bilinear interpolation distorts the distribution by shifting it towards larger void radii R_v, which is consistent with the induced additional smoothing. In particular, we observe a $\approx 20\%$ suppression in the low radii tail at $R_v \approx 0.02$ deg, and a $\approx 40\%$ enhancement in the high radii tail at $R_v \approx 0.14$ deg. In the case of ray-tracing with NGP and NUFFT interpolation, we only find a much smaller effect, namely a suppression at $R_v \approx 0.15$ deg amounting to around $\approx 10\%$, and

deviations at the most extreme bins of the distribution, at $R_v < 0.02$ deg and $R_v < 0.16$ deg.

Moving to the stacked radial void profiles, we find that, also in this case, ray-tracing with bilinear interpolation has the strongest impact: it enhances the inner and outer regions while suppressing intermediate radii by $\approx 5\%$, at the peak of the convergence. This flattening of the profile can be explained by the effective smoothing introduced by bilinear interpolation. The effect of ray-tracing with NGP and NUFFT interpolation is significantly weaker, with the most noticeable feature being a $\approx 0.5\%$ suppression of the convergence in the innermost regions of the voids. This effect can be connected to the enhancement we observe in the low tail of the PDF of the minima distribution. In the case of NUFFT interpolation, we observe additional $\approx 1\%$ deviations at $r/R_v \approx 1$.

In general, we find that, modulo the artificial smoothing effects introduced by the bilinear interpolation, the post-Born corrections do not have a significant impact on void statistics. We tested the above statistics for a range of peak catalogue thresholds (Davies et al., 2018) and found qualitatively similar results.

4.3.6 Minkowski Functionals

Finally, we investigate the impact of the Born approximation on the Minkowski functionals. These are, in general, a set of $N + 1$ morphological descriptors invariant under rotations and translations that characterize a field in an N-dimensional space. The MFs are defined on an excursion set $\Sigma(\nu) = \kappa > \nu\sigma_0$; i.e. for the set of pixels whose values exceed a certain threshold $\nu\sigma_0$. Here σ_0 is conventionally chosen as the standard deviation of the field.

In our case we are dealing with a 2D field on the surface of the sphere, therefore we have the following three MFs: V_0 is simply the total area of the excursion set; V_1 is one-fourth of the total perimeter of the excursion set; and finally V_2, called "genus", is associated with the number of connected regions minus the number of topological holes of the excursion set. We refer the reader to equations (2.5), (2.6) and (2.7) of Marques et al. (2024) for the mathematical expressions of V_0, V_1 and V_2. Since MFs encode information from all the moments of the distributions of a field, they are highly sensitive to non-Gaussianities and have thus been proposed as a powerful cosmological statistic in a number of different studies (see e.g., Springel et al., 1998; Schmalzing & Gorski, 1998; Hikage et al., 2008; Ducout et al., 2013).

We show our results for the V_0, V_1, and V_2 functionals in the top, middle and bottom panels of Figure 4.6, respectively. In general, also in this case we note that any discrepancy between bilinear interpolation (green curve) with respect to the other two methods, NGP and NUFFT (red and orange curves), helps us to disentangle the impact of an additional smoothing introduced by bilinear interpolation, from the impact of post-Born corrections themselves.

Let us recall that, by definition, V_0 is the cumulative PDF. Indeed, the impact of the three ray-tracing schemes can be directly related to what we observed for the PDF earlier (top right panel of Figure 4.4). All of the ray-tracing schemes show qualitatively the same trend, with an initial tiny suppression, followed by a small enhancement, and then by a

stronger suppression. At $\kappa \approx 0.1$, this reaches $\approx 2.5\%$ for the bilinear interpolation, and $\approx 1.2\%$ for the NGP and NUFFT interpolation.

In the case of V_1, at $\kappa \approx -0.028$, we see an enhancement of $\approx 35\%$ for ray-tracing with bilinear interpolation and of $\approx 25\%$ in the case of NGP and NUFFT. With increasing values of κ there is a progressive suppression that, at $\kappa \approx 0.1$, reaches $\approx 4\%$ for bilinear interpolation and $\approx 1\%$ for NGP and NUFFT.

In the case of V_2, the genus statistic, we notice that ray-tracing with bilinear interpolation results in notably different effects: we see an enhancement of $\approx 3.5\%$ at $\kappa \approx -0.01$, followed by a suppression of $\approx 2.5\%$ at $\kappa \approx 0.01$ that then progressively diminishes, and eventually fades completely. For NGP and NUFFT interpolation, the effects are smaller. These are a suppression of $\approx 3\%$ at $\kappa \approx -0.02$, followed by an enhancement of 0.5% in the range $-0.015 \lesssim \kappa \gtrsim 0.04$.

Also in this case, the effects of smoothing by bilinear interpolation dominate the post-Born corrections. In particular, as expected, smoothing will shift the distribution to lower thresholds for the perimeter, while for the genus, it will dampen the amplitude.

4.4 Conclusions and outlook

In this chapter, we present our methodology for computing full-sky ray-traced weak lensing maps, starting from the mass-shell outputs of GADGET-4 and applying our code to a subset of the MillenniumTNG simulation suite. After having qualitatively inspected key WL quantities such as convergence, deflection, shear, and rotation, we test the impact of the Born approximation against three ray-tracing schemes that employ NGP, bilinear, and NUFFT interpolation, respectively. These tests were performed on the power spectrum, as well as on a number of popular higher-order WL statistics.

We confirm, in line with theoretical predictions, that post-Born effects tend to Gaussianise the convergence PDF and consequently impact higher-order statistics as well. Regarding the use of different interpolation approaches in ray-tracing schemes, we interestingly find that although bilinear interpolation is in principle more accurate than NGP, the effective smoothing that this introduces at our grid resolution dominates the post-Born effects, even when using a HEALPix map with the maximum resolution of $N_{\rm side} = 8192$. Additionally, we find that NUFFT interpolation, which is the most accurate method, agrees well with the NGP scheme in the present study. We can explain this by noting that a 1 arcmin smoothing, applied before the computation of all the higher-order statistics, tends to wash out information at the smallest angular scales, where the differences between these two methods are expected to become appreciable. We note that since the accuracy of NGP interpolation strongly depends on the HEALPix resolution, we expect the agreement with NUFFT to be degraded for lower values of $N_{\rm side}$.

We summarize the impact of using a ray-tracing scheme instead of the Born approximation for the different statistics as follows:

- The angular power spectrum is not significantly affected by the Born approximation. Smoothing due the use of bilinear interpolation in a ray-tracing approach suppresses

the power at progressively smaller scales.

- The convergence PDF is slightly Gaussianised by ray-tracing, which enhances the low-κ tail and suppresses the high-κ tail. We find deviations at $\kappa \approx -0.025$ of $\approx 10\%$ when NGP and NUFFT interpolation are used, and of $\approx 4\%$ when bilinear interpolation are used.

- Peaks counts are suppressed, at $\kappa \simeq 0.15$, by $\approx 1.5\%$ for ray-tracing with NGP and NUFFT interpolation and by $\approx 2.5\%$ for bilinear interpolation.

- Minima counts on the other hand are mainly enhanced, at $\kappa \approx -0.025$, by $\approx 15\%$ for NGP and NUFFT interpolation and by $\approx 7\%$ for bilinear interpolation.

- The void abundance and the void profiles are not significantly influenced by the Born approximation. However, smoothing due to bilinear interpolation distorts the void abundance with deviations up to $\approx 40\%$, and it flattens the void profiles with deviations up to $\approx 5\%$.

- The three 2D Minkowski functionals we investigated are affected to different degrees. Most noticeably, V_1 is enhanced at $\kappa \approx -0.028$ by $\approx 35\%$ for ray-tracing with bilinear and by $\approx 25\%$ for ray-tracing with NGP and NUFFT interpolation.

Overall, we find only very subtle consequences due to the use of the Born approximation. However, for higher-order statistics, they become sizable enough that the use of ray-tracing is necessary if exquisite precision is required. The need for interpolation arising in ray-tracing schemes typically introduces the technical problem of additional discreteness effects that can diminish or even defeat the accuracy improvements that ray-tracing in principle offers. Such problems can be overcome by adopting a novel interpolation scheme based on NUFFT. For currently achievable all-sky HEALPix resolutions, we find that low-order NGP interpolation agrees well with the NUFFT scheme, especially when a 1 arcmin smoothing is adopted. On the other end, the bilinear interpolation is found to be unreliable as it introduces sizable smoothing effects. Ultimately, in the limit of infinite resolution, we would expect the three interpolation schemes to agree.

Note that the impact of post-Born corrections will increase with increasing source redshift. For WL surveys, source redshift distributions are smooth functions that vary between $z = 0$ up to approximately $z \approx 3$, peaking at $z \approx 1$. In this work, our source redshift distribution corresponds to a δ-function at $z = 1$, which is roughly the median source redshift of typical Stage-IV WL surveys. Therefore, we expect the results presented here to be indicative of what can be expected for more realistic redshift source distributions.

We conclude that harvesting the accuracy benefits of ray-tracing is ultimately *required* in full-sky WL simulations in order to accurately model higher-order statistics to the percent level.

The methods presented and tested in this work pave the way to several applications in the context of high-fidelity modeling in the era of precision cosmology. One possible development could be to compute, from the simulations used in this work, a detailed and

realistic full-sky galaxy mock catalogue based on the latest version of the semi-analytic galaxy formation code L-GALAXIES (Barrera et al., 2023), which can be then combined with our ray-tracing code to obtain highly accurate predictions for the 3x2pt as well as higher-order statistics. Another possibility consists of using the full-hydro MTNG run to extract the galaxy intrinsic alignment signal (a key contaminant of cosmological WL) from the lightcone (in a similar way to Delgado et al., 2023) and to compare/combine it with the shear signal computed with our ray-tracing code.

Chapter 5

Fully non-linear simulations of galaxy intrinsic alignments for weak lensing with the MillenniumTNG lightcone

The content of this chapter has been submitted to the Monthly Notices of the Royal Astronomical Society and reported here with slight modifications.

Abstract

We present a complete forward model of a realistic weak lensing galaxy catalogue based on the 740 Mpc hydrodynamical MillenniumTNG (MTNG) simulation. Starting with a complete particle and cell lightcone covering one octant of the sky with redshift range $0 < z < 1.5$, we apply a group and subhalo finder to generate the corresponding galaxy catalogue for a fiducial observer. For all galaxies, we compute both their intrinsic and lensing-induced shear. The intrinsic component is derived from the luminosity-weighted inertia tensor of stellar particles, while the extrinsic (gravitational) shear is obtained through full-sky ray-tracing on the same lightcone. This allows us to directly predict the impact of intrinsic alignment (IA) of galaxies on the shear correlation function and popular convergence statistics in a fully non-linear forward model. We find that IA modifies the convergence power spectrum at all angular scales by up to 20%, it significantly impacts the PDF, altering its tails by 10–20%, and distorts peak and minimum counts up to 30%, depending on redshift and scale. We also evaluate the impact of the IA signal on the shear correlation function, finding that, along with a redshift dependence, the signal strongly increases for higher galaxy stellar mass cuts applied to the catalogue. Notably, with the highest stellar mass cut we apply, the intrinsic shear autocorrelation can become comparable to the gravitational shear component on small angular scales. Our results highlight the importance of accurately modeling IA for precision weak lensing cosmology with upcoming Stage IV surveys.

5.1 Introduction

It is well known that galaxies tend to align with the surrounding matter field (Valdes et al., 1983; Miralda-Escude, 1991; Hirata et al., 2007), referred to as galaxy intrinsic alignment (IA, for reviews, see e.g., Joachimi et al., 2015; Kirk et al., 2015; Kiessling et al., 2015; Lamman et al., 2024). Such alignment, aside from being used as a cosmological probe (see e.g., Chisari & Dvorkin, 2013; Schmidt et al., 2015; Akitsu et al., 2021; Kurita & Takada, 2023; Schmidt & Jeong, 2012b; Akitsu et al., 2023; Taruya & Okumura, 2020; Okumura & Taruya, 2023; Xu et al., 2023), directly contaminates the WL signal, by introducing an additional correlation between galaxy shapes and alignments that is independent of WL, where the WL signal itself is extracted from galaxy shape measurements (Joachimi & Bridle, 2010; Zhang, 2010; Troxel & Ishak, 2012).

The degree to which IA contaminates WL measurements is still not well constrained, and efforts to quantify and describe the IA signal have resulted in a range of analytical models that span different approaches and degrees of sophistication. Examples include the *Linear Alignment* model (LA, Catelan et al., 2001; Hirata & Seljak, 2004), *Nonlinear Alignment* model (NLA, Bridle & King, 2007; Joachimi et al., 2011), *Tidal Alignment and Tidal Torquing* model (TATT, Blazek et al., 2019), hybrid Lagrangian models (e.g. HYMALAYA, Maion et al., 2024), effective field theory models (e.g., Vlah et al., 2020, 2021; Bakx et al., 2023; Chen & Kokron, 2024), and models based on the halo model formalism (Schneider & Bridle, 2010; Fortuna et al., 2021). These analytical models can only be incorporated into summary statistics for which analytic models also exist, such as the WL power spectrum. It is generally nontrivial to extend these analytic models to higher-order statistics, where one instead needs to rely on measurements from simulations. Recent strategies to address this problem include the IA infusion approach (Harnois-Déraps et al., 2022), which uses the same mass-shells employed in numerical WL ray-tracing to forward model the IA signature.

The intrinsic alignment of galaxies is a complex phenomenon, which is influenced by a variety of factors ranging from cosmological scales down to sub-galactic scales (see e.g., Troxel & Ishak, 2015), which are highly nonlinear. For this reason, hydrodynamical simulations have emerged as an essential tool to quantify this effect (a non-exhaustive list includes Chisari et al., 2015; Tenneti et al., 2015; Velliscig et al., 2015b; Hilbert et al., 2017; Bate et al., 2020; Bhowmick et al., 2020; Shi et al., 2021; Kurita et al., 2021; Samuroff et al., 2021; Zjupa et al., 2022; Lee et al., 2025). These studies demonstrate that hydrodynamical simulations can meaningfully capture IA, as they incorporate detailed galaxy formation physics and do not assume any relationship between galaxies and the surrounding gravitational field or their host halos.

Recently, Delgado et al. (2023, hereafter D23) used a very large hydrodynamical simulation of galaxy formation, the flagship simulation of the MillenniumTNG (MTNG) project, to measure the projected correlation function of the intrinsic shear of galaxies, and detected IA with the density field at high significance. D23 further detected a significant IA signal for elliptical galaxies assuming the NLA model, a weak IA signal for spirals assuming the TATT model, and a mass-dependent misalignment between central galaxies and their host

dark-matter halos.

Our work significantly extends the analysis conducted by D23 for the MTNG simulation, with a focus on the lightcone output, to produce a realistic shear catalogue which directly captures both the intrinsic shear, as well as the extrinsic (lensing-induced) shear; i.e. the pure WL signal. Such a catalogue, which covers an octant of the sky and spans the redshift range $z = [0, 1.5]$, allows us to directly predict the impact of intrinsic alignments on a range of commonly used WL lensing statistics, in the fully non-linear regime, and without relying on analytic models. The statistics measured here include: shear correlation function, convergence power spectrum, convergence PDF, convergence peaks, and minima.

This chapter is organized as follows. In Section 5.2, we provide some key quantities of the intrinsic alignment formalism (Sec. 5.2.1) and introduce the correlation function (Sec. 5.2.2). In Section 5.3, after describing the methodology used to construct the galaxy catalogue (Sec. 5.3.1), we show our galaxy selection (Sec. 5.3.2), and describe how we compute intrinsic and extrinsic shear (Sec. 5.3.3 and 5.3.4), and generate convergence maps (Sec. 5.3.5). In Section 5.4, we present our main results. Starting with a comparison to theoretical prediction (Sec. 5.4.1), we then investigate the redshift dependence (Sec. 5.4.2) and the mass dependence (Sec. 5.4.3) of IA on WL. We conclude in Section 5.5 with a summary of our findings and an outlook on future applications.

5.2 Theoretical background

In this section, we integrate the theoretical framework presented in Section 2.1 by introducing key quantities related to the intrinsic alignment of galaxies, along with the formalism of the correlation function.

5.2.1 Intrinsic ellipticity of galaxies

In this chapter, we will refer to the gravitationally induced (extrinsic) shear as $\gamma_{\rm G}$, in order to distinguish it from the intrinsic shear $\gamma_{\rm I}$, which we are about to introduce.

The three-dimensional shape of galaxies can be approximated as a triaxial ellipsoid. The projection of such an object onto the celestial sphere (described in detail in Section 5.3.3) results in an ellipse with major axis a, minor axis b, and orientation angle ϕ, defined as East of North. This lets us introduce another spin-2 field, the ellipticity[1]:

$$\epsilon \equiv \frac{a^2 - b^2}{a^2 + b^2} \exp\left(2\mathrm{i}\phi\right), \tag{5.1}$$

which can be converted to the intrinsic shear through:

$$\gamma_{\rm I} = \frac{\epsilon}{2\mathcal{R}}. \tag{5.2}$$

[1]Note that there is more than one possible definition of the ellipticity, for a discussion we refer the interested reader to section 2.2 of Lamman et al. (2024).

Here the responsivity factor $\mathcal{R}$ accounts for the average response of the ellipticity to a given shear. Consistently with D23, in the following we assume $\mathcal{R} = 1$, justified by the assumption that galaxy isophotes are elliptical and the absence of measurement noise (see e.g., Bernstein & Jarvis, 2002). Finally, under the assumption that the gravitational shear is sufficiently small, one can obtain the total (observed) shear $\gamma_{\rm O}$ simply by adding the intrinsic and the (extrinsic) gravitational components:

$$\gamma_{\rm O} \approx \gamma_{\rm I} + \gamma_{\rm G} \,, \tag{5.3}$$

which is the relation employed in this work.

5.2.2 Correlation function

The two-point shear correlation function is the most well studied and widely used WL summary statistic. For two generic shear fileds A and B, it is defined as:

$$\xi_{\pm,AB}(\theta) = \langle \gamma_{A,+}(\boldsymbol{\theta'})\gamma_{B,+}(\boldsymbol{\theta'}+\boldsymbol{\theta})\rangle \pm \langle \gamma_{A,\times}(\boldsymbol{\theta'})\gamma_{B,\times}(\boldsymbol{\theta'}+\boldsymbol{\theta})\rangle \,, \tag{5.4}$$

where γ_+ and $\gamma_\times$ are the tangential and cross components of the shear with respect to the direction connecting a pair of galaxies separated by an angular distance[2] θ. Given the Cartesian shear components γ_1 and γ_2, these projections are defined as:

$$\gamma_+ = -\left(\gamma_1 \cos 2\varphi + \gamma_2 \sin 2\varphi\right) \,, \tag{5.5a}$$
$$\gamma_\times = -\left(-\gamma_1 \sin 2\varphi + \gamma_2 \cos 2\varphi\right) \,, \tag{5.5b}$$

where φ is the polar angle of the separation vector between the two galaxies (for a schematic visualization, see e.g. Figure 2 of D23).

The correlation function is particularly useful for comparing observational data with theoretical models in real space, as it can be directly estimated from galaxy shape measurements. In this work, we compute its GG (gravitational), II (intrinsic), and GI (cross) components.

The Fourier counterpart of the correlation function is the angular power spectrum $C_{AB}(\ell)$, the two are related via the Hankel transforms:

$$\xi_{+,AB}(\theta) = \int_0^\infty \frac{\ell\,\mathrm{d}\ell}{2\pi}\, C_{AB}(\ell)\, J_0(\ell\theta), \qquad \xi_{-,AB}(\theta) = \int_0^\infty \frac{\ell\,\mathrm{d}\ell}{2\pi}\, C_{AB}(\ell)\, J_4(\ell\theta), \tag{5.6}$$

where J_0 and J_4 are the zeroth- and fourth-order Bessel functions, respectively (see e.g., Schneider et al., 2002).

In this study we will focus on the shear correlation function and on the convergence power spectrum. We recall Equation (2.10) to motivate the interchangeability of the convergence and shear power spectrum under the assumption of negligible shear B-modes (see e.g., Kilbinger, 2015).

[2] In the context of the correlation function, θ denotes a scalar separation angle between two objects on the celestial sphere. This should be distinguished form $\boldsymbol{\theta}$, which refers to a two-dimensional position vector on the sky, whose components are θ_1 and θ_2.

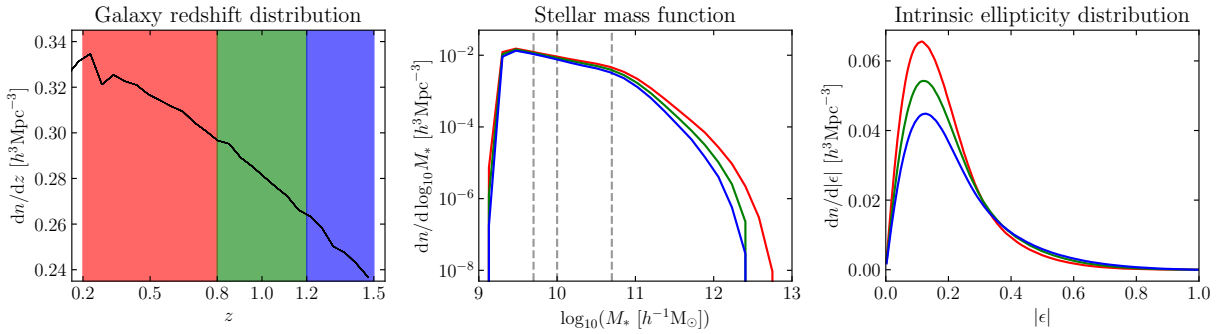

Figure 5.1: The left, center and right panels show the redshift distribution, the mass function and the absolute ellipticity distribution of galaxies in our catalogue, respectively. The shaded regions in the left panel refer to the three redshift bins used in this work and are consistent with the colours adopted in the two rightmost panels. The grey dashed lines in the central panel refer to the minimum stellar mass cuts of $[5\times10^9, 1\times10^{10}, 5\times10^{10}]\ h^{-1}\mathrm{M}_\odot$ applied to the catalogue in Section 5.4.3. We observe that, as expected, the galaxy number density decreases with increasing redshift. We also note that, as the redshift decreases, the mass function grows consistently with hierarchical structure formation, and that the galaxy ellipticities tend to move toward lower values (i.e. rounder shapes).

5.3 Methods

In this work, we use the lightcone and mass-shell output of the flagship full-hydrodynamics run of the MillenniumTNG (MTNG) project, introduced in Section 3.2.1.

5.3.1 Generation of the galaxy catalogue

Our galaxy catalogue is generated by running an updated version of the Friends-of-Friends (FoF) group finding algorithm (Davis et al., 1985) combined with the SUBFIND-HBT substructure finder codes present in GADGET-4. These routines have been specifically optimised for efficiency on lightcones, where the output structure consists of a succession of consecutive redshift slices. In this work, we decided to use the particle lightcone with the combination of sky coverage and redshift depth that best matches the specifications of a stage IV survey. The chosen lightcone corresponds to one octant of the sky (coordinates $x > 0$, $y > 0$, $z > 0$) for redshifts $0 \leq z \leq 1.5$, reaching comoving distance $\approx 3050\,h^{-1}$Mpc (see Section 3.5 of Hernández-Aguayo et al., 2023, for a comprehensive list of the available MTNG lightcones). For this lightcone, the raw particle data amounts to over 540 TB, requiring significant computational resources to process. From this, by means of the FoF algorithm, we identified more than 1.30×10^{10} halos, and, by means of the SUBFIND-HBT algorithm, we identified more than 1.26×10^{10} substructures.

5.3.2 Galaxy selection and redshift distribution

In order to cover a galaxy stellar mass range that is as close as possible to that which is observed with stage IV surveys, we select our galaxies as the subhalos with at least 100 stellar particles and a minimum total mass of $1.0 \times 10^{10}\,\mathrm{M}_\odot$. This results in a galaxy population with a minimum stellar mass of $\approx 1.0 \times 10^{9}\,\mathrm{M}_\odot$, as one can see in Figure 5.1, where we show the stellar mass function of our catalogue in the three redshift bins described in the following paragraph. We point out that the same stellar particle threshold has been applied in Hilbert et al. (2017), and we refer the reader to Chisari et al. (2015) and Velliscig et al. (2015a) for details on measurement errors of ellipticity distributions as a function of particle number.

With the selection described above, the resulting galaxy redshift distribution is shown in the left panel of Figure 5.1. Our catalogue features a total of $\approx 2.10 \times 10^8$ galaxies, corresponding to an angular source density of ≈ 11.31 galaxies per square arcminute. In order to investigate the redshift dependence of the impact of IA on WL observables, we partition our catalogue into three tomographic redshift bins with edges at $z = [0.2, 0.8, 1.2, 1.5]$, highlighted by the shaded regions in the left panel of Figure 5.1. The corresponding comoving distance width for each of the bins is $\Delta\chi \approx [1371, 676, 416]\,h^{-1}\mathrm{Mpc}$. This choice results in each bin containing a similar number of galaxies, and thus gives a constant noise level between different redshift bins.

5.3.3 Computation of intrinsic ellipticity

In numerical simulations, galaxies and haloes are typically represented by an ensemble of N particles. A common way to quantitatively describe the three-dimensional shape of these objects is to consider the inertia tensor I, which sums over all particle distances from the center associated with a given object and is given by the expression:

$$I_{ij} = \frac{1}{W} \sum_{k=1}^{N} w^k x_i^k x_j^k \,, \tag{5.7}$$

where x represents the distance of a given particle from the centre of the object, with the indices i and j running over the three spatial components, $i, j \in (x, y, z)$, and w_k are weight factors (e.g. mass or luminosity of the particles) whose sum is W. We now want to compute the 2D ellipticity of the galaxy as seen on the celestial sphere, defined in Equation (5.1). To do so, we need to project I onto a two-dimensional surface perpendicular to the line of sight $\hat{\boldsymbol{n}}$ at the galaxy angular position $\boldsymbol{\theta}$. Similarly to Tsaprazi et al. (2022), we define an orthonormal basis $(\hat{\boldsymbol{n}}, \hat{\boldsymbol{\theta}}_1, \hat{\boldsymbol{\theta}}_2)$, where

$$\hat{\boldsymbol{\theta}}_1 = \cos\theta_1 \cos\theta_2 \hat{\boldsymbol{x}} + \cos\theta_1 \sin\theta_2 \hat{\boldsymbol{y}} - \sin\theta_1 \hat{\boldsymbol{z}} \,, \tag{5.8a}$$

$$\hat{\boldsymbol{\theta}}_2 = -\sin\theta_2 \hat{\boldsymbol{x}} + \cos\theta_2 \hat{\boldsymbol{y}} \,, \tag{5.8b}$$

with (θ_1, θ_2) being the colatitude and longitude of the galaxy, and $(\hat{\boldsymbol{x}}, \hat{\boldsymbol{y}}, \hat{\boldsymbol{z}})$ is the orthonormal basis of the Cartesian coordinates.

Following Schmidt & Jeong (2012a) and Schmidt et al. (2015) we then define the linear combinations:

$$\boldsymbol{m}_{\pm} \equiv (\hat{\boldsymbol{\theta}}_2 \mp \mathrm{i}\hat{\boldsymbol{\theta}}_1)/\sqrt{2}\,, \tag{5.9}$$

where i is the imaginary unit. This allows us to decompose the inertia tensor into the spin-2 field $I_{\pm} = I_1 \pm \mathrm{i}I_2$ according to

$$I_{\pm} = \sum_{i=1}^{3}\sum_{j=1}^{3} m_{\mp}^{i} m_{\mp}^{j} I_{ij}\,. \tag{5.10}$$

In this way, after having also defined the normalization factor

$$I_{\mathrm{norm}} = \sum_{i=1}^{3}\sum_{j=1}^{3} m_{-}^{i} m_{+}^{j} I_{ij}\,, \tag{5.11}$$

we can write the ellipticity projected onto the sky as:

$$\epsilon = \epsilon_1 \pm \mathrm{i}\epsilon_2 = \frac{I_1 \pm \mathrm{i}I_2}{I_{\mathrm{norm}}}\,. \tag{5.12}$$

In this work, consistent with D23, we will use the V-band luminosity as a weight for the inertia tensor, which leads to the following specialisation of equation (5.7):

$$q_{ij}^{(V)} = \frac{1}{L^{(V)}} \sum_{k}^{N} L^{k,(V)} \left(x^k - \overline{x}^{(V)}\right)_i \left(x^k - \overline{x}^{(V)}\right)_j\,, \tag{5.13}$$

where $L^{k,(V)}$ and $L^{(V)}$ are the V-band luminosity of the k-th stellar particle and of the whole galaxy, respectively; and x^k and $\overline{x}^{(V)}$ are the position vector of the k-th stellar particle and the V-band luminosity weighted centre of the galaxy, respectively.

As a sanity check, in the right panel of Figure 5.1 we show the ellipticity modulus distribution in the three redshift bins we defined in Sec. 5.3.2. We find that both the shape distribution and the redshift evolution of the distribution are qualitatively consistent with similar studies (Samuroff et al., 2021; Chisari et al., 2015; Zhang et al., 2022; Lee et al., 2025), with an increasing fraction of rounder object as the redshift is decreasing. This trend can be mainly interpreted as a consequence of phenomena like dynamical relaxation (see e.g., Lynden-Bell, 1967; Binney & Tremaine, 2008) and mergers (see e.g., Negroponte & White, 1983; Naab & Burkert, 2003), both of which tend to isotropize galaxy shapes over time. We note that the observed trend toward rounder galaxy shapes at lower redshift, while qualitatively consistent with expectations from the aforementioned effects, may be affected by numerical limitations. In particular, the relatively low particle count per galaxy in the simulation used in this work can lead to artificially short relaxation times, potentially exaggerating this effect. A natural extension would be to perform higher-resolution zoom-in simulations of selected galaxies within the MTNG volume to assess how shape distributions evolve with improved resolution.

5.3.4 Computation of galaxy image positions and gravitational shear

To compute the gravitational shear and the image (observed) positions of the galaxies, we start by producing a collection of full-sky shear and deflection HEALPix maps (Górski et al., 2005) using the DORIAN ray-tracing code (Ferlito et al., 2024). We compute these maps for slices with a thickness of $100\,h^{-1}$Mpc, starting at a comoving distance of $100\,h^{-1}$Mpc from the observer ($z \approx 0.03$), up to $3.1\,h^{-1}$Gpc ($z \approx 1.55$). We use a HEALPix tessellation with $N_{\rm side} = 8192$, which yields an angular resolution of 0.43 arcmin.

A deflection map relates the image position of each ray, located at the pixel centre of a regular HEALPix grid, to the respective position on the source plane, where we note that source positions generally do not follow a regular arrangement. We can use the deflection map to compute the image position of galaxies in our catalogue, starting from their source (true) positions. For a given galaxy source position $\boldsymbol{\beta}_{\rm g}$, one can define a triangle whose vertices are neighbouring rays[3] and that contains $\boldsymbol{\beta}_{\rm g}$; once such a triplet of rays is found, one can perform a barycentric interpolation (see e.g. section 21.3 of Press et al., 2007) from the source plane to the image plane to estimate the observed galaxy position $\boldsymbol{\theta}_{\rm g}$ (see e.g. Figure 7 of Hilbert et al., 2009, for a visualization of this interpolation scheme). Operating on the curved sky, the algorithm we implemented for the galaxy image search is similar in many aspects to the one of Becker (2013, we refer the interested reader to section 3.3 of this work for further details). One difference is that our code performs a KD-tree-based neighbour search, which looks for the 30 closest rays on the source plane for each galaxy[4].

For each galaxy, we first compute the image position using the two deflection maps corresponding to the neighbouring source planes that enclose the galaxy's redshift; then we perform a linear interpolation between these two to obtain our final estimate of the image position. We note that galaxies for which multiple image positions are found are excluded from the catalogue, as they are likely subject to strong lensing, and therefore would be excluded in a WL lensing survey.

Once the observed galaxy positions are determined, we apply non-uniform fast Fourier transform (NUFFT) interpolation (Fessler & Sutton, 2003; Barnett et al., 2019; Reinecke et al., 2023; Ferlito et al., 2024) on HEALPix shear maps to compute the gravitational shear at those positions. Again, we evaluate this quantity at the two maps with source redshifts that enclose each galaxy and linearly interpolate the shear values to obtain the final estimate. Compared to the more conventional approaches like nearest-grid-point or bilinear interpolation on the HEALPix grid, NUFFT offers both higher accuracy and efficiency when evaluating the shear at arbitrary positions.

5.3.5 From shear to convergence maps

With the methodology outlined above, we have built a catalogue containing, amongst other quantities, each galaxy's observed angular position, intrinsic shear, and gravitational shear.

[3] Note that the rays have to be neighbours in the image plane.

[4] We found that looking for the $\approx$ 10–20 closest rays already gives convergent results.

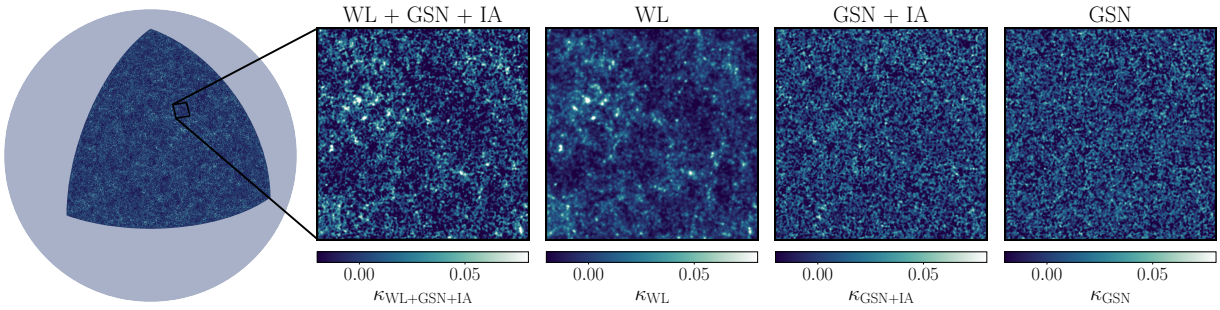

Figure 5.2: *From left to right:* full "WL + GSN + IA" (Weak Lensing + Galaxy Shape Noise + Intrinsic Alignment) map displayed as an octant of the sky with a zoom into a $10 \times 10\,\mathrm{deg}^2$ square patch, followed by zoomed patches of the same area, for the "WL", "GSN + IA", and "GSN" cases. The maps are computed considering source galaxies in our central redshift bin, $0.8 < z < 1.2$. For illustrative purposes we have smoothed the maps using a Gaussian symmetric beam characterised by a standard deviation of 1 arcmin. We see that the IA contribution in the "GSN + IA" panel leads to weak correlations with the WL signal, while the "GSN" panel appears consistent with white noise.

Our aim is now to compute convergence maps on a regular (HEALPix) grid starting from the value of the shear at the observed galaxy position. To perform this transformation we use the relationship between κ and γ in Fourier space (Kaiser & Squires, 1993), known as the Kaiser-Squires transformation. In particular, we first extract the spherical harmonics coefficients $\gamma_{\ell m}$ from the shear map with the `pseudo_analysis_general` routine[5], which is part of the DUCC library (Reinecke, 2020), and then use the relation

$$\kappa_{\ell m} = -\gamma_{\ell m} / \sqrt{(\ell+2)(\ell-1)/(\ell(\ell+1))} \tag{5.14}$$

to obtain the spherical harmonics coefficients of the convergence (we refer the interested reader to Hu, 2000, for a derivation of this relation). We then use the HEALPix `alm2map` routine to compute the convergence map on the regular HEALPix grid.

To directly test the impact of IA on higher-order statistics measured in the κ field, we compute three main types of convergence maps, depending on the shear field we use as input for the above equation. The first one, labelled "WL + GSN + IA", is obtained by using the total shear given by equation (5.3); this field contains the WL signal as well as the galaxies' intrinsic shear contribution, introduced in equation (5.2). By plugging equation (5.1) into equation (5.2), one can see that the intrinsic shear, represented by a complex quantity, can be split into its modulus (i.e. shape), which gives rise to the *galaxy shape noise* component (GSN, see e.g., Kaiser et al., 1995; Bernstein & Jarvis, 2002), and orientation, which contains information about the intrinsic alignment.

The second type of convergence map, labeled "WL + GSN", is obtained by adding the gravitational shear and a modified version of the intrinsic shear field, where for each

[5]This routine can be seen as a generalized version of the HEALPix `alm2map` routine, which accepts as input a generic, non-uniform, distribution of points on the sphere.

galaxy the shape is preserved, but the orientation has been rotated by a random angle. This preserves the shape noise contribution, but erases the intrinsic alignment.

Finally, the third type is obtained by considering only the gravitational shear component, and is referred to as "WL". Additionally, one can compute the "GSN + IA" and "GSN" cases, by using the original intrinsic shear and the intrinsic shear with randomized orientations as inputs respectively.

We note that given that the WL signal is only evaluated at (observed) galaxy positions, the convergence maps generated here also include contamination of the lensing signal from source clustering.

Figure 5.2 shows a visualisation of the different types of convergence maps described above, for the central redshift bin $0.8 < z < 1.2$. For illustrative purposes we have smoothed the maps using a Gaussian symmetric beam characterised by a standard deviation of 1 arcmin. The first panel shows the full "WL + GSN + IA" map displayed as an octant of the sky. Subsequent panels show a zoom into a $10 \times 10\,\mathrm{deg}^2$ square patch, starting with a zoom of the same "WL + GSN + IA" map. We then show zoomed patches of the same area, for the "WL", "GSN + IA", and "GSN" cases. The first zoomed panel ("WL + GSN + IA") clearly depicts a noisy realisation of large-scale-structure features, which can be visually verified by comparing it to the adjacent panel of "WL", where only the true WL signal is displayed. The next panel shows the "GSN + IA" map, where weak correlations with the 'WL" map can be observed. This can be attributed to the IA signal in the "GSN + IA" map, since the IA signal is a direct consequence of the large-scale structure. Finally, the last panel shows the "GSN" map, which is visually consistent with a white noise field.

5.3.6 Computation of WL and IA statistics

Here we outline the numerical procedures and binning specifications used when measuring each of the WL statistics studied in this work. The shear correlation function is computed with the TreeCorr code (Jarvis, 2015), and binned into 40 equally spaced logarithmic bins in the range $\theta \in [1, 400]$ arcmin. The convergence power spectrum is computed using the HEALPix routine `anafast`, and binned into 50 equally spaced logarithmic bins in the range $\ell \in [1, 1.2 \times 10^4]$. Before computing probability distribution functions (PDFs) for convergence, peaks and minima, every convergence map is smoothed with a Gaussian symmetric beam characterised by a standard deviation of 2 arcmin using the HEALPix `smoothing` routine. For the convergence PDF, we bin the pixels into 50 linearly spaced bins in the range $\kappa \in [-0.07, 0.12]$. Peaks and minima are identified as the pixels that are greater or smaller than their 8 neighbours, respectively[6], which are retrieved using the HEALPix `get_all_neighbours` routine. For the peaks, we use 30 linearly spaced bins in the range $\kappa \in [-0.1, 0.2]$, while for the minima we use 25 linearly spaced bins in the range $\kappa \in [-0.07, 0.05]$.

[6]In the HEALPix tessellation, every pixel has 8 neighbours, except for a small minority of pixels, for which it can be 7 or 6.

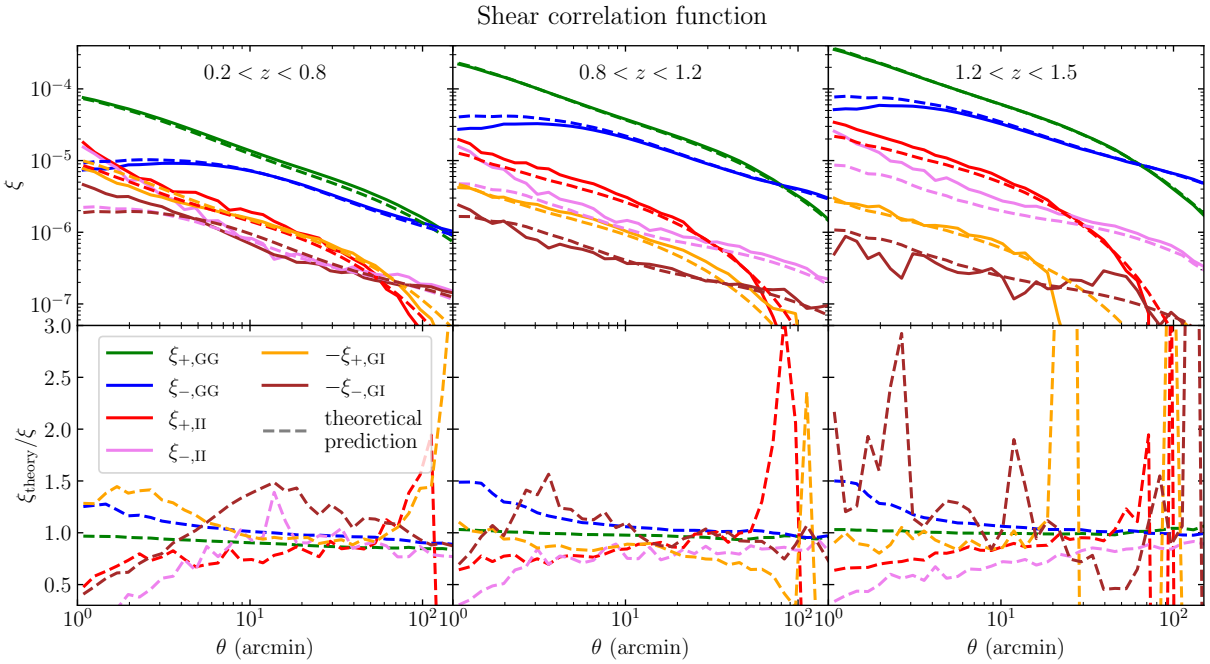

Figure 5.3: Comparison between the shear correlation function as computed on our results and its theoretical prediction, obtained by means of the CCL library (Chisari et al., 2019). Each column refers to a different redshift bin. The top panels show the shear correlation function, while the bottom panels give the ratio of the theoretical prediction over our results. In the case of $\xi_{\rm II}$ and $\xi_{\rm GI}$ we use the Nonlinear Alignment model (NLA) for the theory prediction, which provides good overall agreement with the measured signals, with best-fit alignment amplitudes around $A_1 \approx [2.06, 2.55, 3.52]$ for bins with increasing redshift.

5.4 Results

5.4.1 Comparison to theory

To validate our pipeline, we begin by examining the shear correlation function and compare it with theoretical predictions, as shown in Figure 5.3. We select galaxies from our catalogue that reside in each of our redshift bins, and compute the auto-correlation of the gravitational and intrinsic shear components, labeled "GG" and "II" respectively, as well as the cross-correlation function, labeled "GI". The GI term, as expected, exhibits a negative sign. This anti-correlation arises because the intrinsic shape of (foreground) galaxies tends to align radially with the large-scale gravitational potential, pointing toward overdense regions, while the lensing shear of (background) galaxies is tangential around the same overdense regions.

We produce theoretical predictions for the above quantities with the CCL[7] library (Chisari et al., 2019). To do so, we start by computing the shear E-mode auto and cross

[7]https://github.com/LSSTDESC/CCL

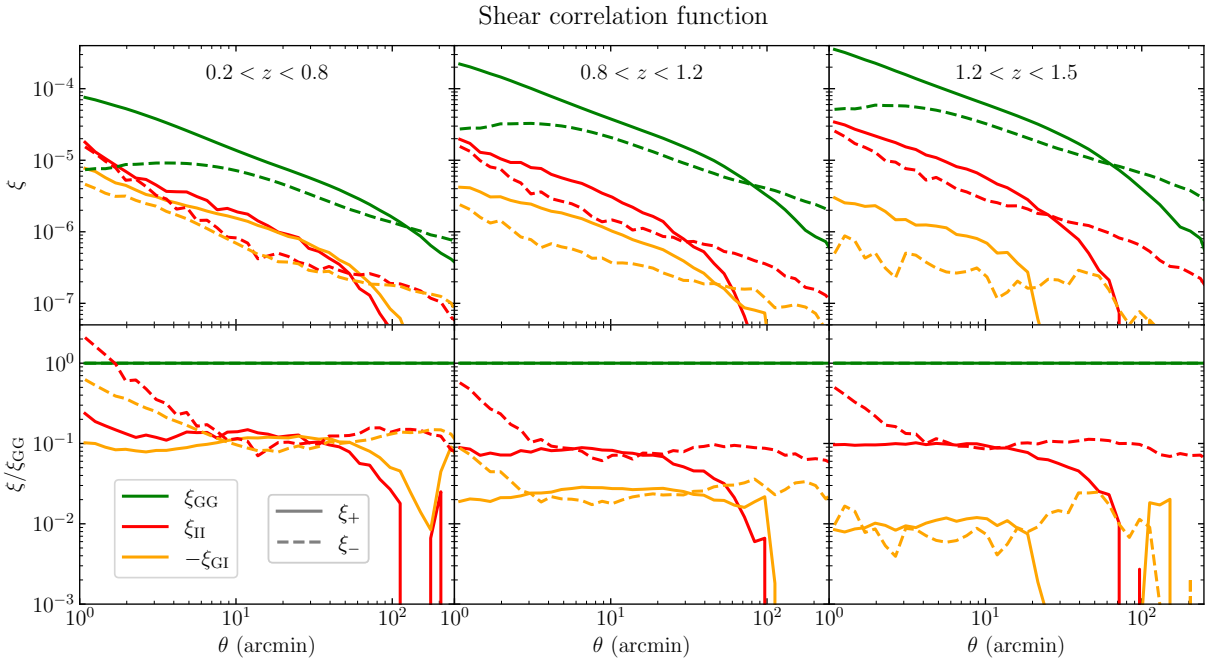

Figure 5.4: Shear auto-correlation of the pure weak lensing component $\xi_{\rm GG}$ (green lines), auto-correlation of the pure intrinsic alignment component $\xi_{\rm II}$ (red lines), and their cross-correlation $\xi_{\rm GI}$ with inverted sign (yellow lines). The solid and dashed lines indicate the ξ_+ and ξ_- statistics, respectively. The top panels show the correlation function, while the bottom panels display the ratio with respect to the auto-correlation $\xi_{\rm GG}$. Each column refers to a different redshift bin. The II and GG signals grow with redshift while maintaining a roughly constant $\xi_{\rm II}/\xi_{\rm GG}$ ratio, whereas the GI signal decreases in relative amplitude, reflecting the redshift evolution of the IA signal.

angular power spectra according to equations (50), (51), and (52) of Lamman et al. (2024). The corresponding formulae require the source redshift distribution as input (shown in Figure 5.1), as well as the 3D matter power spectrum in the redshift range of interest, which in this work is computed with the HALOFIT formula (Takahashi et al., 2012b). In the case of the II and GI power spectra, we employ the NLA model (Bridle & King, 2007), which assumes a linear proportionality between the intrinsic shape of galaxies and the local tidal gravitational field. Although similar to the LA model (Catelan et al., 2001), the NLA model also incorporates the nonlinear evolution of the matter density field. The proportionality is expressed in terms of the A_1 parameter, consistent with the definitions in equation (11) of Samuroff et al. (2023). Once the angular power spectra are computed, these can be converted into correlation functions according to Equation (5.6).

Overall, we observe a qualitatively good agreement between our results and the theoretical predictions in the angular range we investigate. The NLA model provides a reasonably good fit to the data on scales where its assumptions hold: particularly at intermediate and large angular separations. Best-fit values of the alignment amplitude, obtained by minimiz-

ing the root mean square error between the NLA prediction and our data for $\theta \gtrsim 2$ arcmin, are approximately $A_1 \approx [2.06, 2.55, 3.52]$ for the low-, intermediate-, and high-redshift bin respectively.

Figure 5.3 shows that the NLA model agrees with our simulated pipeline to within $\approx 50\%$. While such deviations are expected given the limitations of the NLA model, this large discrepancy serves as motivation for our fully non-linear simulated pipeline. This enables a more accurate characterization of the IA signal and gives us direct access to higher-order statistics measurements that include IA contributions without relying on simplifying assumptions.

5.4.2 Redshift dependence

Having validated our basic results, we now move on to investigate the redshift dependence of the shear correlation function, as well as the convergence angular power spectrum, its PDF, and peaks and minima.

Shear Correlation function

In Figure 5.4, we present the shear correlation functions computed for the three redshift bins investigated in this work. Looking at the gravitational (GG) and intrinsic (II) auto-correlations, we see that, as the redshift increases, both increase in amplitude, maintaining roughly the same ratio of $\xi_{\rm II}/\xi_{\rm GG} \approx 0.1$ at intermediate angular scales; i.e. $\theta \approx 10\,$arcmin, as shown by the red curve in the bottom sub-panels. The redshift evolution of $\xi_{\rm II}$ has been reported in previous numerical studies (see e.g. D23; Chisari et al., 2015; Zjupa et al., 2022), and the increase of its amplitude with redshift can be explained by the following two arguments. First, it is consistent with the theoretical framework in which a lower non-linear disruption of alignments at high redshift is expected (see e.g., Lamman et al., 2024). Second, we recall that, as seen in Section 5.3.2, our three redshift bins are characterised by a decreasing comoving width with redshift. It is important to note that, as the width of the shell increases, regions that are progressively more separated in physical space, and thus less correlated, will be projected together, diluting the overall signal.

Regarding the gravitational-intrinsic (GI) cross-correlation function, we see that the amplitude remains relatively constant for different redshift bins, with the ratio $-\xi_{\rm GI}/\xi_{\rm GG}$ going from ≈ 0.1, to ≈ 0.02, to ≈ 0.008, at low, intermediate and high redshifts respectively. Furthermore, it is interesting to note that the GI signal shows a decreasing trend relative to the II signal with increasing redshift. In particular, in the lowest redshift bin, we find that $\xi_{\rm GI}$ and $\xi_{\rm II}$ have similar amplitude and scale dependence, especially at angular scales larger than ≈ 10 arcmin. This redshift trend can help us understand the substantial redshift evolution of the impact of IA on WL convergence statistics, which we investigate in the next section.

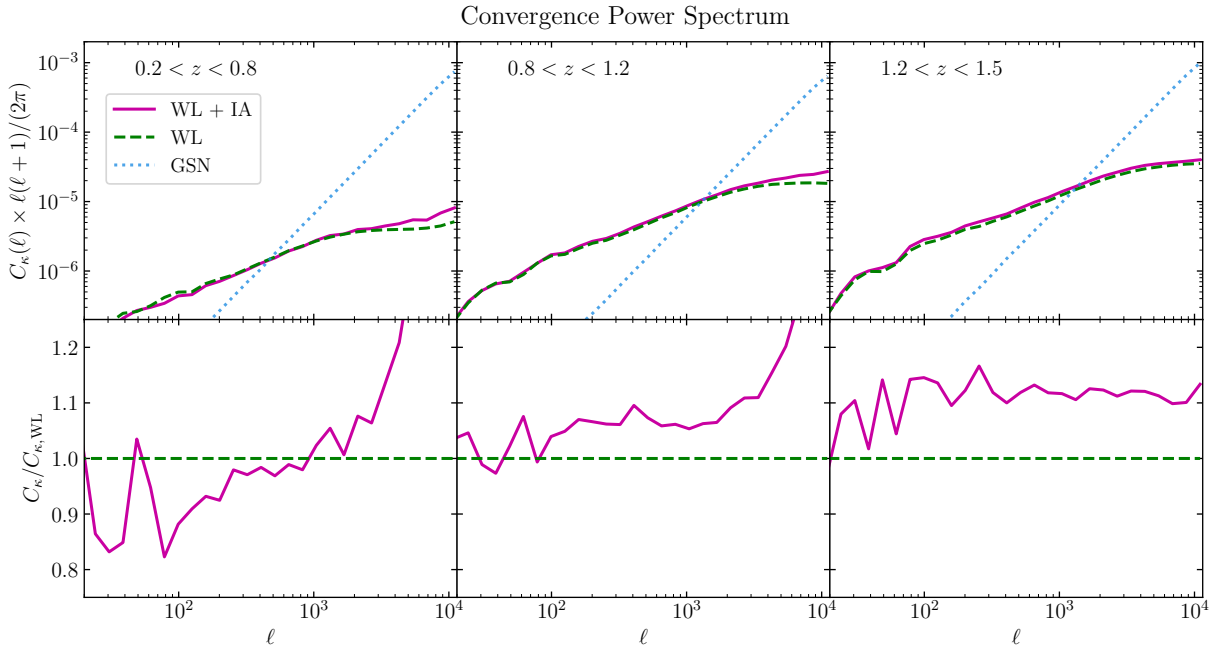

Figure 5.5: Angular power spectrum of convergence maps. Dashed green lines show the pure weak lensing (WL) signal; light blue dotted lines indicate galaxy shape noise (GSN); purple solid lines represent maps including both WL and IA, with GSN subtracted. Bottom sub-panels show ratios relative to the WL case. Each column corresponds to a redshift bin. IA introduces a scale- and redshift-dependent modulation of the WL power spectrum, due to the interplay between negative GI and positive II terms causing suppression at low redshift and large scales, and up to $\sim 20\%$ enhancement at small scales and high redshift.

Convergence power spectrum

In Figure 5.5, we show the convergence power spectrum in the three redshift bins investigated in this work. After computing the convergence maps according to Section 5.3.5, we measure the angular power spectrum for the pure WL signal (green dashed curve), and the GSN signal (blue dotted curve), using the corresponding convergence fields. To obtain the power spectrum of the WL convergence field with the IA signal ("WL + IA", purple solid curve), i.e. no GSN contribution, we first compute the power spectrum of the convergence field corresponding to WL + GSN + IA, and then subtract the GSN power spectrum.

First, we observe that the GSN curve follows a white noise spectrum, as expected (see e.g., Kaiser et al., 1995). We note that the noise component crosses the WL spectrum at $\ell \approx 500$ in the low redshift bin, and at $\ell \approx 1500$ in the two remaining redshift bins. Looking at the ratio between the WL + IA and WL curves, we see that the IA signal has a significant qualitative impact on the WL signal over all redshift bins. At high redshift, we observe a $\approx 10\%$ power enhancement at all scales, which is slightly weaker at the largest angular scales plotted here. At the intermediate redshift, we see a stronger trend in ℓ, which is weaker at large-intermediate scales, giving a $\approx 5\%$ enhancement at

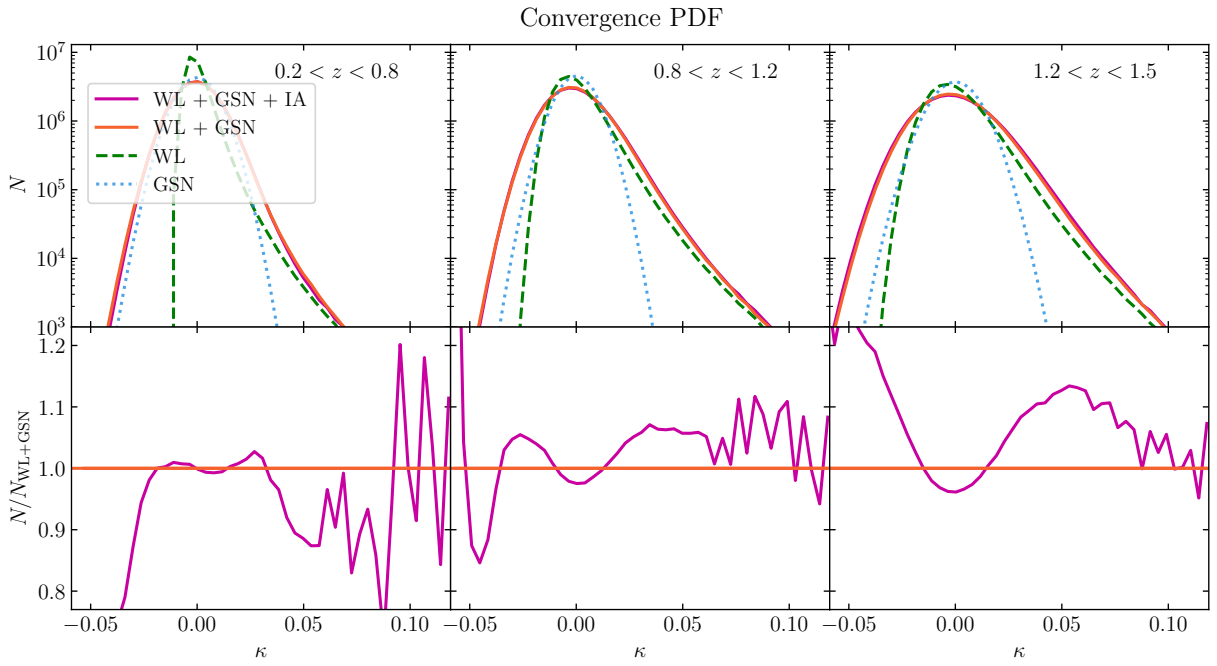

Figure 5.6: PDF of convergence maps; purple solid lines correspond to maps including WL, GSN, and IA; orange solid lines show the same case but with randomized intrinsic orientations; dashed green lines show the pure WL signal; light blue dotted lines indicate the GSN. Bottom sub-panels show ratios with respect to the WL + GSN case. Maps were smoothed with a 2 arcmin Gaussian kernel before PDF computation. Each column corresponds to a redshift bin. IA alters the convergence PDF in a redshift-dependent way that can be partially explained by considering the power spectrum: boosted power at high redshift broadens the PDF, suppression at low redshift narrows it; at intermediate redshift, enhanced small-scale power induces non-Gaussian PDF distortions.

$10^2 \lesssim \ell \lesssim 10^3$, but becoming progressively larger at the smaller angular scales, reaching 20% at $\ell \approx 5000$. Moving to the low redshift bin, we see a $\approx 10\%$ suppression at large scales, then the suppression progressively decreases, with the ratio approaching one at intermediate angular scales ($\ell \approx 900$), which then turns into an enhancement (similar to the intermediate redshift bin), reaching 20% at $\ell \approx 4000$.

The strong redshift dependence observed in the power spectrum can be better understood by comparing it to the shear correlation function in Figure 5.4. In particular, let us start by noting that the WL + IA power spectrum, being the sum of two components, i.e. gravitational and intrinsic, can be expressed as $C_{\kappa,\mathrm{WL+IA}} = C_{\kappa,\mathrm{GG}} + 2C_{\kappa,\mathrm{GI}} + C_{\kappa,\mathrm{II}}$. Additionally, from Figure 5.4, we note that the values of $|\xi_{\mathrm{GI}}|$ and $|\xi_{\mathrm{II}}|$ are roughly comparable, especially at scales larger than 10 arcmin. Finally, we recall that the gravitational and intrinsic shear fields are anti-correlated; i.e. ξ_{GI} is negative (and so is $C_{\kappa,\mathrm{GI}}$). By combining the above information, it becomes clearer that the $C_{\kappa,\mathrm{WL+IA}}/C_{\kappa,\mathrm{WL}}$ ratio is less than one at large-to-intermediate scales in the low redshift bin, which can be explained in terms of the

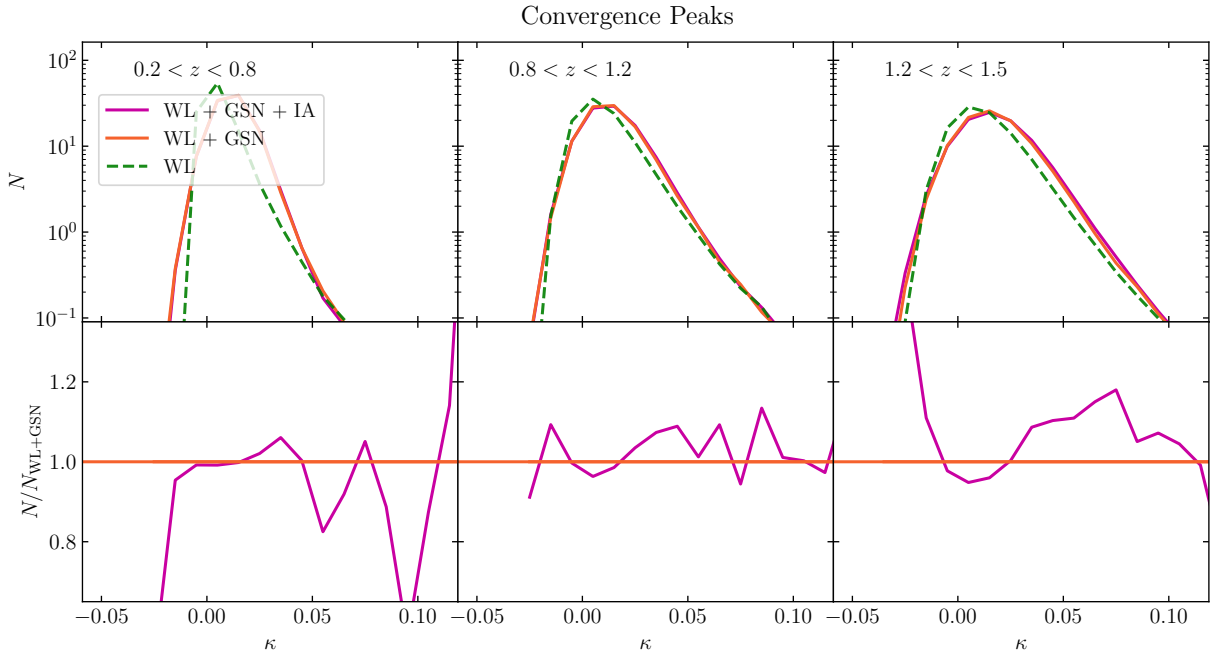

Figure 5.7: Peak counts distribution of convergence maps; the purple solid lines refer to maps containing the total signal comprehensive of WL, intrinsic galaxy shapes (GSN), and orientations (IA); the orange solid lines refer to a version of the previous case where intrinsic ellipticities have been preserved, but intrinsic orientations have been randomized; the dashed green lines refer to the pure weak lensing signal. The maps have been smoothed with a 2 arcmin Gaussian kernel before the computation of the statistic. The top sub-panels show the peak counts, while the bottom sub-panels give the ratio with respect to the WL + GSN case. Each column refers to a different redshift bin. The impact of IA on peak counts mirrors the redshift-dependent trends observed in the convergence PDF (shown in Figure 5.6), with tail suppression at low redshift, enhancement at high redshift, and more complex, small-scale-driven distortions at intermediate redshift.

cross-correlation term (GI) dominating the intrinsic auto-correlation term (II) in this bin. On the other hand, the cross term becomes progressively less important at intermediate and high redshift, which explains the increasing values of $C_{\kappa,\mathrm{WL+IA}}/C_{\kappa,\mathrm{WL}}$ seen in these bins.

Convergence PDF, peaks and minima

In Figure 5.6, we show the convergence PDF for the three redshift bins investigated in this work. First, we note that the PDF of the pure WL convergence field (green dashed curve) shows a significant positive skewness, which arises from nonlinear structure growth (see e.g., Valageas, 2000). In contrast to this, we see that the pure GSN convergence field (blue dotted curve) follows a Gaussian distribution, consistent with white noise. The convergence field that contains both of the components described above, i.e. WL + GSN

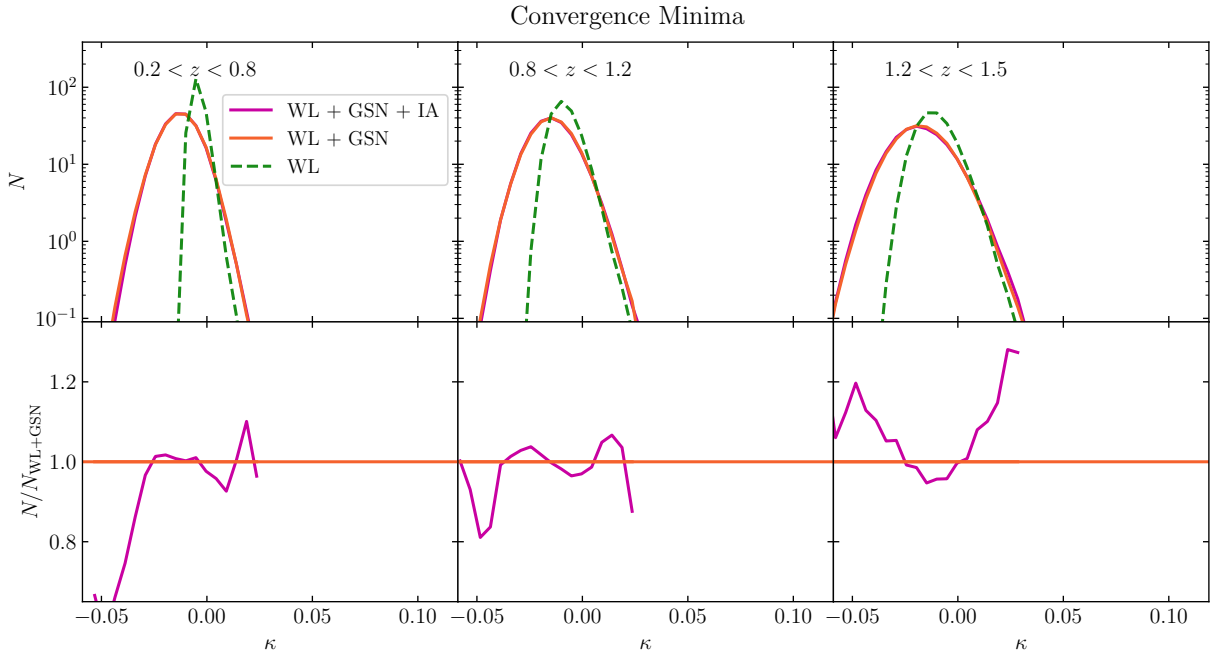

Figure 5.8: Minimum counts distribution of convergence maps; the purple solid lines refer to maps containing the total signal comprehensive of WL, intrinsic galaxy shapes (GSN), and orientations (IA); the orange solid lines refer to a version of the previous case where intrinsic ellipticities have been preserved, but intrinsic orientations have been randomized; the dashed green lines refer to the pure weak lensing signal. The maps have been smoothed with a 2 arcmin Gaussian kernel before the computation of the statistic. The top sub-panels show the minimum counts, while the bottom sub-panels give the ratio with respect to the WL + GSN case. Each column refers to a different redshift bin. The impact of IA on minimum counts mirrors the redshift-dependent trends observed in the convergence PDF (shown in Figure 5.6), with tail suppression at low redshift, enhancement at high redshift, and more complex, small-scale-driven distortions at intermediate redshift.

(orange solid line), is characterised by a PDF that results from the convolution of the PDFs of its individual components. Therefore, as we can see in the top sub-panels, the PDF of the WL + GSN convergence field is broader, less skewed, and has diluted non-Gaussian features with respect to the pure WL convergence PDF.

Let us now investigate the impact of IA on the convergence PDF. To do so we consider the lower sub-panels, where the ratio between the WL + GSN + IA and WL + GSN cases is shown. To ease the interpretation, we now discuss the redshift bins in an order where the underpinning physics of interest increases in complexity, which is high-z, then low-z, followed by intermediate-z. For the high-z bin, we see that the impact of IA leads to a clear broadening of the PDF. This is characterised by an enhancement of the high- and low-κ tail that reaches $\approx 20\%$ and $\approx 13\%$ at $\kappa \approx -0.04$ and $\kappa \approx 0.055$ respectively; and a suppression of the central region, that reaches $\approx 4.5\%$ at $\kappa \approx 0$. To better understand the nature of this broadening, let us notice that, as seen in the previous section, the presence

of IA boosts the convergence power spectrum at all scales in this redshift bin. Therefore, a boost in power will increase the field's variance, resulting in a broader PDF, since the width of the PDF is set by the variance of the field. Moving our attention to the low-redshift bin, and using the same argument given above, the reduction in power leads to a narrowing of the convergence PDF when IA is included. This appears as a suppression of the high- and low-κ tails that reaches $\approx 20\%$ and $\approx 12\%$ at $\kappa \approx -0.03$ and $\kappa \approx 0.055$ respectively, with a distortion of the central region that remains below $\approx 3\%$. Focusing now on the intermediate redshift bin, we observe that IA distorts the PDF in a more complex way, showing intermediate features between the other two redshift bins. Given that the power is enhanced the most at small scales with the inclusion of IA in this redshift bin, we can conclude that the impact from IA that we observe on the PDF is driven by the small scales. Noting that these scales are non-linear, this leads to modifications of the higher-order moments of the convergence field, which manifest as more complex alterations to the shape of the PDF, namely the multiple crossings of $N_{\rm WL+GSN+IA}/N_{\rm WL+GSN} = 1$ at low κ. The impact in this bin is characterised by a suppression of the low-κ tail that reaches $\approx 15\%$ at $\kappa \approx -0.045$, and distortions in the rest of the PDF that reach $\approx 12\%$ at $\kappa \approx 0.08$.

We continue our analysis of the redshift dependent impact of IA on WL convergence statistics by studying peak and minimum counts, shown respectively in Figure 5.7 and Figure 5.8. Looking at the overall picture, we first remind the reader that distortions in the peaks and minima distributions are closely linked to distortions in the convergence PDF, particularly in its tails. Indeed, it can be clearly seen that the impact of IA on both peaks and minima, at each redshift bin, show trends that are qualitatively consistent with the impact on the PDF. We also note that, while the trends are similar to the PDF, the peaks and minima statistics are measured with coarser bins relative to the PDF, as there are far fewer extrema than pixels in a given WL map, which leads to the coarser ratios presented in Figure 5.7 and Figure 5.8 compared to the PDF.

In the case of the peak counts, focusing on the low-redshift bin, we observe that the inclusion of IA leads to a suppression of the tails that reaches $\approx 20\%$ at $\kappa \approx -0.019$, and $\approx 18\%$ at $\kappa \approx 0.055$. Regarding the intermediate redshift bin, we observe that the distribution tends to fluctuate, similar to the PDF, showing an alternation of enhancements and suppressions that never exceed $\approx 13\%$. In the case of the high-redshift bin, we observe an enhancement of the tails that reaches $\approx 30\%$ at $\kappa \approx -0.02$, and $\approx 17\%$ at $\kappa \approx 0.075$.

Finally, in the case of the minimum counts, looking at the low-redshift bin we find a suppression in the low-κ tail that reaches $\approx 30\%$ at $\kappa \approx 0.041$, and fluctuations in the high-κ tail that reach $\approx 10\%$ at $\kappa \approx 0.018$. In the intermediate redshift bin, we observe fluctuations below $\approx 7\%$ over the range $-0.04 \lesssim \kappa \lesssim 0.02$. In the case of the high-redshift bin we observe an enhancement of the tails that reaches $\approx 20\%$ at $\kappa \approx -0.05$, and $\kappa \approx 0.02$.

Before moving on to the next section, we remark that our findings are consistent with a very recent study by Lee et al. (2025), who performed a similar analysis based on the IllustrisTNG project, finding IA to impact the convergence power spectrum, PDF, peaks and minima with comparable magnitude to what is detected in our study. However, we point out that a direct comparison with this study is not possible, since, amongst

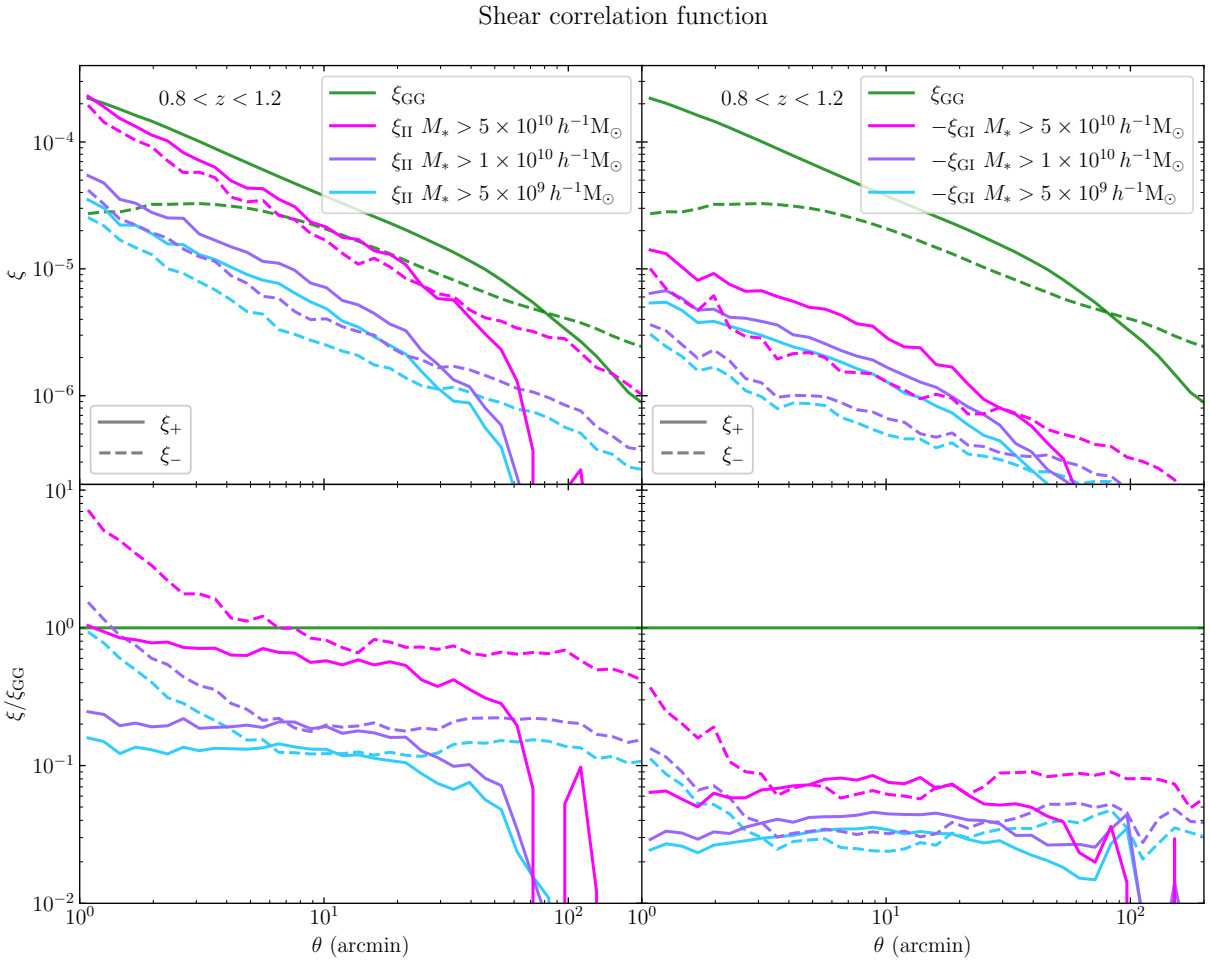

Figure 5.9: *Left (right)*: the light blue, violet and pink curves refer to the auto-correlation of the pure intrinsic alignment component $\xi_{\rm II}$ (cross-correlation between intrinsic and gravitational shear $\xi_{\rm GI}$) for increasingly higher minimum stellar mass thresholds. The green lines refer to the auto-correlation of the gravitational shear $\xi_{\rm GG}$. The top panels give the correlation function, while the bottom panels display the ratio with respect to the auto-correlation $\xi_{\rm GG}$. The shear intrinsic auto- and gravitational-intrinsic cross-correlation amplitudes increase with stellar mass, with a stronger effect on $\xi_{\rm II}$ than on $\xi_{\rm GI}$. The case with the highest minimum stellar mass cut shows IA signals comparable to the WL signal, especially at small angular scales.

other things, their analysis considered the total source population without redshift binning and uses different selection criteria to build the catalogue (e.g. minimum number of star particles). Moreover, our analysis offers improved robustness and sampling of large scale modes as it is based on a box volume that is ≈ 15 times bigger.

5.4.3 Galaxy stellar mass dependence

Having investigated the redshift dependence of the impact of IA on a variety of WL statistics, we conclude our analysis by studying the galaxy stellar mass dependence of the shear intrinsic autocorrelation and the gravitational-intrinsic cross-correlation. To do so, we first select three possible minimum stellar mass thresholds $M_{\rm min} = [5 \times 10^9, 1 \times 10^{10}, 5 \times 10^{10}]\ h^{-1}{\rm M}_\odot$ (indicated by the grey dashed lines in the central panel of Figure 5.1) and apply them to our catalogue. Successively, we compute $\xi_{\rm II}$ and $\xi_{\rm GI}$ in our central redshift bin and present it in Figure 5.9, where the left and right sub-panels refer to $\xi_{\rm II}$ and $\xi_{\rm GI}$, and increasing minimum stellar mass cuts are represented by the light blue, violet, and pink curves, respectively. For a direct comparison with the WL signal, we also include $\xi_{\rm GG}$ in all panels, represented by the green curves.

By looking at $\xi_{\rm II}$ and $\xi_{\rm GI}$, we notice that both quantities experience a nearly scale-independent increase in amplitude with increasing stellar mass thresholds. To quantify such an increase in the theoretical context, we have performed a fit of the NLA model to our results, finding best matches with $A_1 = [3.31, 4.07, 7.93]$ for $M_{\rm min} = [5\times10^9, 1\times10^{10}, 5\times10^{10}]\ h^{-1}{\rm M}_\odot$. This trend is qualitatively consistent with observations (see e.g., Joachimi et al., 2013; Singh et al., 2015; Samuroff et al., 2023) and previous simulation results (see e.g. D23; Chisari et al., 2015; Hilbert et al., 2017; Zjupa et al., 2022), indicating that more massive galaxies, which are often of early-type and reside in denser environments, are more coherently aligned with the surrounding large-scale structure, thereby amplifying the intrinsic alignment signals.

Focusing on the lower sub-panels, it becomes clearer that the mass dependence has a stronger impact on the amplitude of $\xi_{\rm II}$ than on that of $\xi_{\rm GI}$. This behavior can be directly explained in the context of the NLA model, by noting that it predicts $\xi_{\rm II} \propto A_1^2$ and $\xi_{\rm GI} \propto A_1$. We observe that, considering the lowest and highest mass cuts, and looking at intermediate angular scales, $\xi_{\rm II}/\xi_{\rm GG}$ changes from ≈ 0.12 to ≈ 0.65, while $-\xi_{\rm GI}/\xi_{\rm GG}$ goes from ≈ 0.03 to ≈ 0.07. Notably, we find that a mass cut of $5 \times 10^{10}\, h^{-1}{\rm M}_\odot$ boosts the amplitude of $\xi_{\rm II}$ to a level that is of the same order of magnitude as $\xi_{\rm GG}$. Interestingly, we see that $\xi_{-,\rm II}$ dominates $\xi_{-,\rm GG}$ at all angular scales smaller than ≈ 7 arcmin, with $\xi_{-,\rm II}/\xi_{-,\rm GG}$ reaching 170% at the arcmin scale.

The strong stellar mass dependence of the IA signal highlighted above has important implications for interpreting our results throughout the study. As stated in the previous paragraph, a higher mass cut will boost $\xi_{\rm II}$ quadratically and $\xi_{\rm GI}$ linearly, leading the II component to increasingly dominate over the GI component. In the light of the discussions in Section 5.4.2, we expect the effects of higher mass cuts on convergence statistics to be qualitatively similar to the ones observed in the high-z bin of this study, where the II component dominates over the GI component the most.

5.5 Conclusions and outlook

In this chapter, we have presented a fully non-linear and self-consistent forward model to study the impact of intrinsic alignments (IA) on weak lensing (WL), based on the flagship 740 Mpc full-hydro simulation of the MillenniumTNG project. Starting from the particle lightcone covering an octant of the sky in the redshift range $z = [0, 1.5]$, we have identified galaxies with the SUBFIND halo and galaxy finder, and we simultaneously computed both the intrinsic and gravitationally induced (extrinsic) shear signals for each galaxy. The intrinsic shear component is computed from the luminosity-weighted inertia tensor of stellar particles. The extrinsic (gravitational) shear is extracted via full-sky ray-tracing on the same simulation using the DORIAN code (i.e., without invoking the Born approximation). This allowed us to directly evaluate the impact of IA on a range of WL observables, including shear correlation functions, convergence power spectra, and higher-order statistics such as the convergence PDF, peak, and minimum counts. All of these quantities where studied for three different redshift bins, with edges at $z = [0.2, 0.8, 1.2, 1.5]$.

To validate our pipeline, we compared the measured shear correlation functions with theoretical predictions derived using the Nonlinear Alignment model (NLA) for IA. We found good qualitative agreement across the redshift bins and angular scales considered, with the best fit obtained for an alignment amplitude of $A_1 \approx [2.06, 2.55, 3.52]$ for the low-, intermediate-, and high-redshift bin respectively.

We analysed the redshift evolution of the shear correlation functions and found that both the gravitational and intrinsic auto-correlations ($\xi_{\rm GG}$ and $\xi_{\rm II}$ respectively) increase in amplitude with redshift, while maintaining a roughly constant ratio of $\xi_{\rm II}/\xi_{\rm GG} \approx 0.1$ at intermediate angular scales ($\theta \approx 10\,\text{arcmin}$). This redshift evolution of $\xi_{\rm II}$ is consistent with reduced non-linear disruption of alignments at high redshift and the narrower comoving width of the redshift bins, which reduces signal dilution. In contrast, the gravitational-intrinsic cross-correlation $\xi_{\rm GI}$ shows a strong decline in relative amplitude, with $-\xi_{\rm GI}/\xi_{\rm GG}$ decreasing from ≈ 0.1 to ≈ 0.008 from low to high redshift, indicating a diminishing role of the GI term at higher redshift.

We then focused on WL convergence statistics and computed these both in the presence and absence of IA. In the case of the convergence power spectrum, we found that the IA signal introduces a notable modification to the WL power spectrum, with redshift- and scale-dependent behavior: a $\sim 10\%$ enhancement at high redshift, a scale-dependent increase peaking at $\sim 20\%$ at small scales at intermediate redshift, and a transition from $\sim 10\%$ suppression at large scales to $\sim 20\%$ enhancement at small scales at low redshift. This complex trend is attributed to the interplay between the gravitational-intrinsic (GI) and intrinsic-intrinsic (II) components, where the GI term dominates at low redshift, leading to suppression, while its influence diminishes with redshift, allowing the II contribution to enhance the signal at higher redshifts.

We examined the redshift-dependent impact of IA on the convergence PDF, peak, and minimum statistics. At high redshift, IA induces a broadening of the PDF, with tail enhancements up to $\approx 20\%$ and $\approx 13\%$ at $\kappa \approx -0.04$ and $\kappa \approx 0.055$, respectively, and a central suppression of $\approx 4.5\%$, consistent with increased power on small scales. Conversely,

at low redshift, the reduced power leads to a narrowing of the PDF, with tail suppressions of $\approx 20\%$ and $\approx 12\%$. These distortions propagate to peak and minimum counts, which mirror the PDF trends: in the low-redshift bin, peak and minimum tails are suppressed by up to $\approx$ 20–30%, while in the high-redshift bin, enhancements reach $\approx 30\%$ for peaks and $\approx 20\%$ for minima; intermediate redshift bins show alternating enhancements and suppressions below $\approx 13\%$.

We further examined the dependence of IA on galaxy stellar mass by applying three increasing minimum stellar mass thresholds and computing the corresponding shear intrinsic and cross-correlations in the central redshift bin. We find that both $\xi_{\rm II}$ and $\xi_{\rm GI}$ increase nearly uniformly across scales with stellar mass, consistent with the expectation that more massive galaxies exhibit stronger alignment with the large-scale structure. Notably, $\xi_{\rm II}$ shows a stronger sensitivity to mass, with its amplitude reaching levels comparable to $\xi_{\rm GG}$ for the most massive galaxies, and even dominating $\xi_{-,\rm GG}$ at scales below ≈ 7 arcminutes.

The results obtained here can also be viewed as an illustration of the power of the new methodology we have explored in this study, namely to study a seamless lightcone obtained directly from a large-volume cosmological hydrodynamical simulation of galaxy formation. This approach is free of many approximations made in more conventional analysis and thus offers the prospect of improved quantitative accuracy and reliability. Looking ahead, future extensions of this work could involve a more detailed exploration of the IA signal and its impact on WL as a function of galaxy morphology, colour, or environment, as well as the influence of different shape estimators on the measured alignment. Furthermore, the framework developed in this work can be used to explore the impact of intrinsic alignments on other observables, including galaxy-galaxy lensing. The galaxy catalogue and associated shear measurements produced in this work will be soon publicly released, providing a valuable resource for a wider range of cosmological and astrophysical studies.

Chapter 6

Summary and outlook

The phenomenon of weak gravitational lensing (WL) refers to the subtle and coherent shear of the images of distant galaxies due to the deflection of light by large-scale structure along the line of sight. WL stands as one of the most powerful probes in modern cosmology, and as the next generation of WL cosmological surveys enters an era of high precision, the need for accurate theoretical modeling and numerical predictions has become essential. In this thesis, I addressed this challenge by performing and analyzing a series of high-fidelity WL simulations based on the MillenniumTNG (MTNG) project, a suite of state-of-the-art cosmological galaxy formation simulations. In this final chapter, I will summarize the findings of this thesis and outline some of the possible future developments.

6.1 Summary of Results

In Chapter 3, by comparing full-physics hydrodynamical simulations with their dark-matter-only counterparts, I quantified the impact of baryonic physics and massive neutrinos on key WL observables, including the convergence power spectrum, probability distribution function (PDF), peaks, and minima. I found that baryons suppress the convergence power spectrum by up to $\approx 15\%$ at $\ell \gtrsim 10^3$, while massive neutrinos with $\sum m_\nu = 0.3$ eV produce a suppression of $\sim 20\%$ at similar scales. Moreover, I found that both baryons and massive neutrinos distort the convergence PDF, and peak and minimum counts with similar magnitude. Encouragingly, my findings are in close agreement with other state-of-the-art simulations, reinforcing the reliability of high-precision WL numerical experiments.

In Chapter 4, I tested the validity of the Born approximation, commonly adopted in WL simulations, by developing DORIAN, a novel full-sky ray-tracing code. I applied this code on the mass-shell outputs from the two largest simulations in the MTNG suite, each spanning 3000 Mpc. I focused on all the aforementioned WL statistics, as well as WL voids, and Minkowski functionals. My results showed that while the Born approximation closely matches full ray-tracing at the power spectrum level, several higher-order statistics exhibit percent-level deviations, underscoring the importance of ray-tracing for high-precision studies. I found that interpolation schemes can significantly affect ray-tracing

accuracy when reaching the arcmin resolution. To address this, I incorporated and studied nonuniform fast Fourier transform (NUFFT), a novel interpolation technique, along with standard methods like nearest grid point and bilinear interpolation.

In Chapter 5, I addressed the intrinsic alignment (IA) of galaxies, a key astrophysical contaminant in WL. To do so, I generated a high-fidelity mock galaxy catalogue based on the seamless lightcone output of the MTNG full-hydro run, spanning over the redshift range $0 < z < 1.5$. For each galaxy, I computed both intrinsic and lensing-induced shear: the intrinsic component was derived from the luminosity-weighted stellar moment of inertia tensor, while the gravitational shear was obtained by running DORIAN on the same lightcone. This enabled a fully non-linear forward prediction of IA effects on WL. I found that IA alters the convergence power spectrum by up to 20% across all angular scales, modifies the convergence PDF tails by 10–20%, and distorts peak and minimum counts by as much as 30%, depending on redshift and smoothing scale. Examining the shear correlation function, I observed that the IA contribution increases significantly with stellar mass cuts, and at the highest mass threshold, the intrinsic shear autocorrelation can reach the gravitational signal on small angular scales.

Overall, the findings of this thesis highlight the critical need for accurate modeling of both physical and numerical systematics in WL analyses. The quantified effects of baryonic physics, massive neutrinos, and intrinsic alignments highlight that omitting these components could lead to significant biases in key WL observables, potentially compromising cosmological inference from future high-precision surveys. Furthermore, the limitations of the Born approximation and the sensitivity to interpolation methods at high resolutions stress the necessity of adopting full ray-tracing techniques in WL simulations.

6.2 Outlook and Future Developments

The results presented in this thesis have highlighted the importance of accurate modeling of a variety of physical and numerical effects in weak lensing (WL) studies. However, there remain several promising directions for further investigation.

An immediate and natural extension of this work consists in expanding the WL framework presented here by including a broader set of WL statistics. While the focus of this thesis was placed mainly on the convergence power spectrum, PDF, peak, and minimum counts, other higher-order statistics, such as the WL voids and Minkowski functionals, on which I tested only the impact of the Born approximation, as well as the bispectrum, trispectrum, and wavelet-based decompositions, offer complementary insights into the non-Gaussian component of the lensing signal and are particularly sensitive to small-scale physics. Quantifying the impact of baryonic physics, massive neutrinos, and IA on these additional statistics would help us in having a more complete and panoramic overview of the impact of those physical systematics.

In the context of baryonic effects, it would be valuable to study the impact on WL statistics of variations in sub-grid model parameters, such as those governing AGN feedback, star formation, and galactic winds. Additionally, testing different implementations

of these models can help quantify the uncertainties associated with numerical choices in hydrodynamical simulations.

Regarding the intrinsic alignments of galaxies, further progress could consist of exploring different galaxy shape estimators, such as the reduced inertia tensor or iterative prescriptions, as well as investigating how the IA signal varies across galaxy populations distinguished by type, luminosity, color, or environment. A better understanding of these dependencies will help improve the current IA theoretical modeling, potentially providing more robust cosmological analyses.

Beyond the ones studied in this thesis, other physical and observational WL systematics certainly merit further investigation. Examples include the uncertainty in source redshift distributions as well as the clustering of source galaxies, which can bias WL measurements if unaccounted for. Incorporating these systematics into simulated WL maps will be fundamental for producing realistic forecasts, e.g. in the context of likelihood analyses. Related to this, a key step forward would be to extend the framework presented here to construct end-to-end simulated WL surveys that incorporate instrumental effects such as point-spread function convolution, noise, and masking. This would significantly push forward the degree of realism of WL numerical modeling.

Looking ahead, the cross-correlation of WL with different astrophysical signals is increasing in popularity. Such a technique not only helps to mitigate survey-specific systematics but also breaks cosmological parameter degeneracies and offers deeper insights into the nature of the dark sector. Therefore, providing high-fidelity numerical predictions of cross-correlation between WL and complementary observables, such as galaxy clustering, X-ray, and thermal Sunyaev–Zel'dovich signals, or even the gravitational wave background, represents a crucial step toward multi-probe cosmology.

Another exciting and vast domain to explore is the numerical simulation of the WL signal in alternative cosmological models beyond ΛCDM, such as those involving modified gravity, interacting dark energy, or early dark energy scenarios. These models often predict enhanced or suppressed structure formation on certain scales, and their signatures may be significantly peculiar and recognizable in higher-order WL statistics.

In conclusion, the work presented in this thesis provides a foundational step in the growing effort to improve the modeling of WL for upcoming cosmological surveys. By combining the MTNG suite of state-of-the-art cosmological galaxy formation simulations with advanced WL numerical methodology, I have investigated several key physical and numerical effects that impact WL statistics. While significant progress has been made, the results also highlight areas where further development is needed. As observational data continue to improve in redshift depth, sky coverage, and angular resolution, additional work will be essential for maximizing their scientific return. The methods and results presented here aim to support this ongoing process.

Appendix A

Impact of different smoothing scales and resolutions

As mentioned in Section 3.2.5, before computing the PDF, peak counts, and minima counts, the convergence maps are smoothed with a Gaussian kernel with a standard deviation of 1 arcmin. Here we assess how varying the smoothing scale impacts our results from Section 3.3.1. In Figure A.1 we show the measurements of the PDF (top row), peak counts (center row), and minimum counts (bottom row) for two additional cases, with smoothing scales of 0.5 (left column) and 2 (right column) arcmin. To ease the comparison, we also reproduce the measurements of these statistics with 1 arcmin smoothing from Figure 3.4 (center column).

We observe that, for all three summary statistics, varying the resolution gives the same qualitative behaviour for the smoothing scales considered here. Quantitatively, we find that when the smoothing scale is smaller, the distortion of the statistics induced by lower angular and mass resolution is greater. The agreement between the dashed and solid green lines is consistent for all smoothing scales, indicating that the conclusions from Section 3.3.1 do not depend on the choice of smoothing scale.

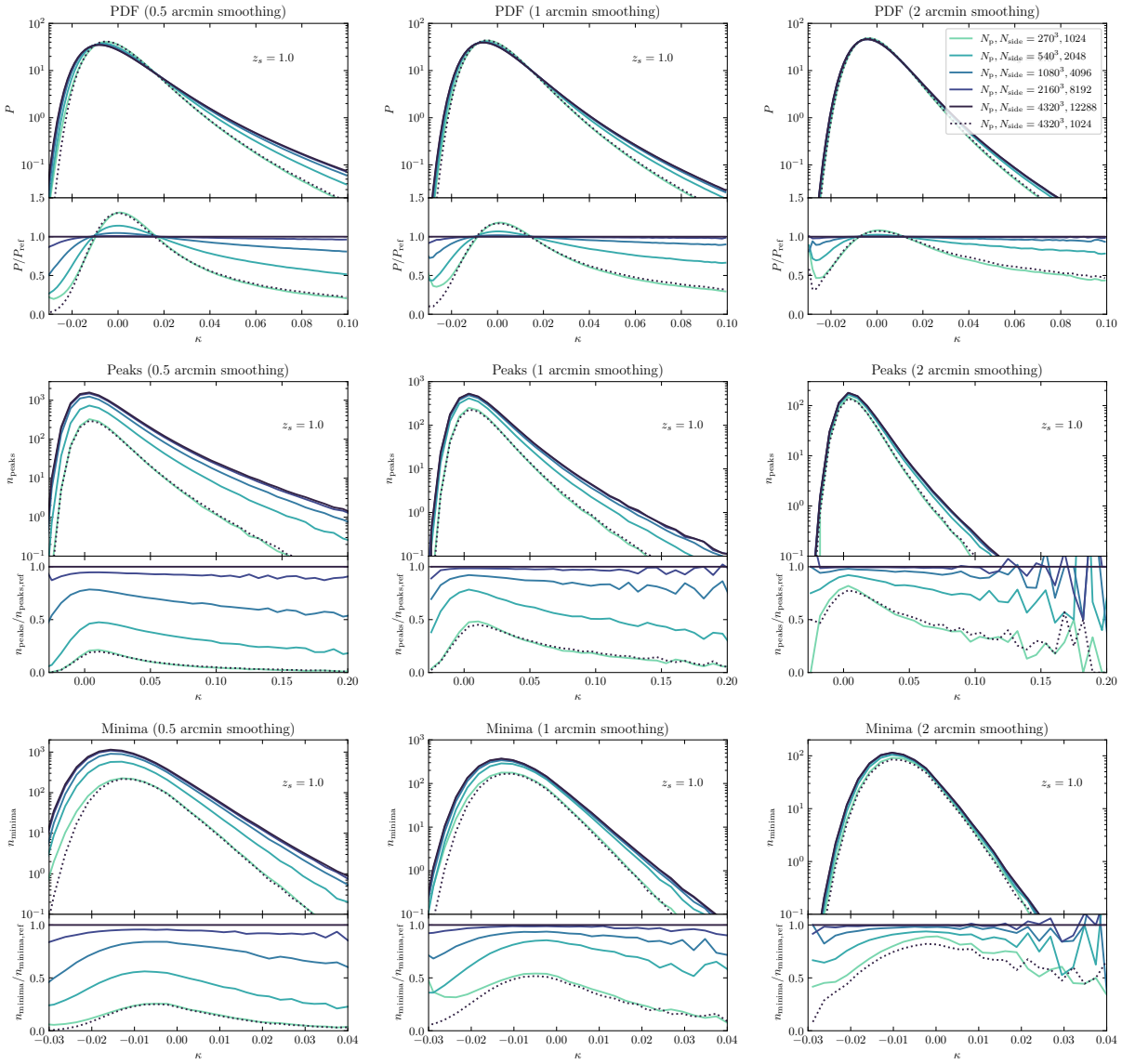

Figure A.1: WL convergence PDF (top row), peak counts (center row), and minimum counts (bottom row); computed in the case of 0.5 (left column), 1 (center column), and 2 (right column) arcmin smoothing. All the observables are computed on the B realization of the MTNG740-DM runs, taking $z_s = 1.0$. The solid lines indicate the mean of 1195 $5 \times 5\,\mathrm{deg}^2$ square maps with increasing darkness representing increasing resolution both in mass and N_{side}. The dotted line refers to the case with the highest mass resolution but down-sampled to $N_{\mathrm{side}} = 1024$. In each lower sub-panel, we show the ratio with respect to the reference case with $N_{\mathrm{part}} = 4320^3$ and $N_{\mathrm{side}} = 12288$ (noted with the subscript "ref").

Appendix B

Impact of bilinear interpolation

In the present work, one of our ray-tracing setups features bilinear interpolation on HEALPix maps, which introduces a smoothing that progressively suppresses the power on small scales. This also narrows the PDF of the convergence, as well as the peaks and minima count distributions.

In the case of a field like the convergence, in which values can vary drastically from pixel to pixel, interpolating on points that are far from pixel centers introduces a significantly

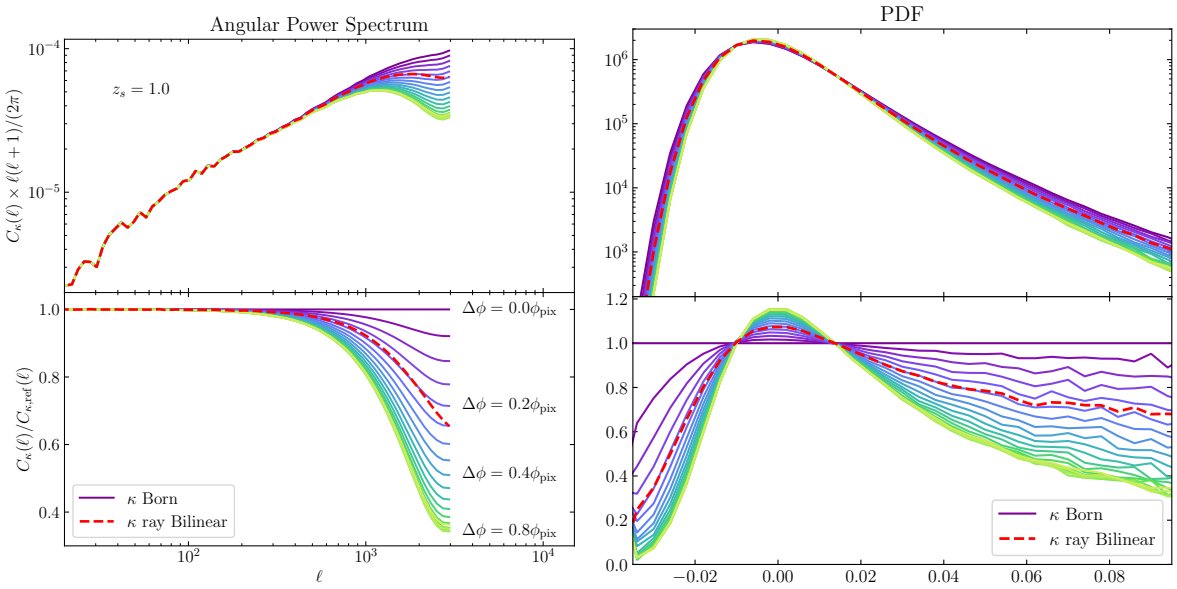

Figure B.1: *Left panel:* angular power spectrum; *right panel*: PDF of the convergence field. These observables are computed for a fiducial source redshift of $z_\mathrm{s} = 1.0$. The solid lines indicate maps that were computed by interpolating from a convergence map in the Born approximation, but using a grid whose pixel centers were shifted longitudinally by an angle $\Delta\phi$, which was systematically varied from 0 to the pixel size ϕ_pix, as labeled. The red dashed line indicates convergence maps computed with ray-tracing and bilinear interpolation, for comparison.

stronger smoothing with respect to points close to pixel centers. To better quantify this effect we performed the following numerical test. We start with a convergence map, based on a HEALPix grid with $N_{\rm side} = 1024$. We then computed a new map by performing a bilinear interpolation on the original map where we effectively rotated the underlying HEALPix grid along the equator by $\Delta\phi$, a fraction of the pixel angular size $\phi_{\rm pix}$. By repeating the above operation with increasing values of $\Delta\phi$, we interpolated on angular positions that are progressively and coherently farther away from the pixel centers. In the left and right panels of Figure B.1, we show the resulting power spectra and the PDF of the convergence maps that have been rotated and interpolated according to the above procedure.

In our ray-tracing scheme, all the rays start from an observed angular position that coincides with the pixel centers, but as these are propagated from plane to plane, their angular positions will be displaced at every step. We therefore expect the overall smoothing effect of bilinear interpolation for each ray and for each lens plane to correspond to an effective smoothing over an intermediate angular offset from the pixel centers. This is exactly what is observed in both panels of Figure B.1, where the line referring to ray-tracing with bilinear interpolation lies consistently within the set of lines indicating increasing values of $\Delta\phi$, closely sticking to the line with $\Delta\phi = 0.2\phi_{\rm pix}$.

Bibliography

Abbott, T., Aguena, M., Alarcon, A., Allam, S., Alves, O., Amon, A., Andrade-Oliveira, F., Annis, J., Avila, S., Bacon, D., Baxter, E., Bechtol, K., Becker, M., Bernstein, G., Bhargava, S., Birrer, S., Blazek, J., Brandao-Souza, A., Bridle, S., Brooks, D., Buckley-Geer, E., Burke, D., Camacho, H., Campos, A., Rosell, A. C., Kind, M. C., Carretero, J., Castander, F., Cawthon, R., Chang, C., Chen, A., Chen, R., Choi, A., Conselice, C., Cordero, J., Costanzi, M., Crocce, M., da Costa, L., da Silva Pereira, M., Davis, C., Davis, T., Vicente, J. D., DeRose, J., Desai, S., Valentino, E. D., Diehl, H., Dietrich, J., Dodelson, S., Doel, P., Doux, C., Drlica-Wagner, A., Eckert, K., Eifler, T., Elsner, F., Elvin-Poole, J., Everett, S., Evrard, A., Fang, X., Farahi, A., Fernandez, E., Ferrero, I., Ferté, A., Fosalba, P., Friedrich, O., Frieman, J., García-Bellido, J., Gatti, M., Gaztanaga, E., Gerdes, D., Giannantonio, T., Giannini, G., Gruen, D., Gruendl, R., Gschwend, J., Gutierrez, G., Harrison, I., Hartley, W., Herner, K., Hinton, S., Hollowood, D., Honscheid, K., Hoyle, B., Huff, E., Huterer, D., Jain, B., James, D., Jarvis, M., Jeffrey, N., Jeltema, T., Kovacs, A., Krause, E., Kron, R., Kuehn, K., Kuropatkin, N., Lahav, O., Leget, P.-F., Lemos, P., Liddle, A., Lidman, C., Lima, M., Lin, H., MacCrann, N., Maia, M., Marshall, J., Martini, P., McCullough, J., Melchior, P., Mena-Fernández, J., Menanteau, F., Miquel, R., Mohr, J., Morgan, R., Muir, J., Myles, J., Nadathur, S., Navarro-Alsina, A., Nichol, R., Ogando, R., Omori, Y., Palmese, A., Pandey, S., Park, Y., Paz-Chinchón, F., Petravick, D., Pieres, A., Malagón, A. P., Porredon, A., Prat, J., Raveri, M., Rodriguez-Monroy, M., Rollins, R., Romer, A., Roodman, A., Rosenfeld, R., Ross, A., Rykoff, E., Samuroff, S., Sánchez, C., Sanchez, E., Sanchez, J., Cid, D. S., Scarpine, V., Schubnell, M., Scolnic, D., Secco, L., Serrano, S., Sevilla-Noarbe, I., Sheldon, E., Shin, T., Smith, M., Soares-Santos, M., Suchyta, E., Swanson, M., Tabbutt, M., Tarle, G., Thomas, D., To, C., Troja, A., Troxel, M., Tucker, D., Tutusaus, I., Varga, T., Walker, A., Weaverdyck, N., Wechsler, R., Weller, J., Yanny, B., Yin, B., Zhang, Y., and, J. Z. (2022), *Dark Energy Survey Year 3 results: Cosmological constraints from galaxy clustering and weak lensing*, Physical Review D, 105(2)

Abbott, T. M. C., Abdalla, F. B., Alarcon, A., Aleksić, J., Allam, S., Allen, S., Amara, A., Annis, J., Asorey, J., Avila, S., Bacon, D., Balbinot, E., Banerji, M., Banik, N., Barkhouse, W., Baumer, M., Baxter, E., Bechtol, K., Becker, M. R., Benoit-Lévy, A., Benson, B. A., Bernstein, G. M., Bertin, E., Blazek, J., Bridle, S. L., Brooks, D., Brout, D., Buckley-Geer, E., Burke, D. L., Busha, M. T., Campos, A., Capozzi, D., Carnero

Rosell, A., Carrasco Kind, M., Carretero, J., Castander, F. J., Cawthon, R., Chang, C., Chen, N., Childress, M., Choi, A., Conselice, C., Crittenden, R., Crocce, M., Cunha, C. E., D'Andrea, C. B., da Costa, L. N., Das, R., Davis, T. M., Davis, C., De Vicente, J., DePoy, D. L., DeRose, J., Desai, S., Diehl, H. T., Dietrich, J. P., Dodelson, S., Doel, P., Drlica-Wagner, A., Eifler, T. F., Elliott, A. E., Elsner, F., Elvin-Poole, J., Estrada, J., Evrard, A. E., Fang, Y., Fernandez, E., Ferté, A., Finley, D. A., Flaugher, B., Fosalba, P., Friedrich, O., Frieman, J., García-Bellido, J., Garcia-Fernandez, M., Gatti, M., Gaztanaga, E., Gerdes, D. W., Giannantonio, T., Gill, M. S. S., Glazebrook, K., Goldstein, D. A., Gruen, D., Gruendl, R. A., Gschwend, J., Gutierrez, G., Hamilton, S., Hartley, W. G., Hinton, S. R., Honscheid, K., Hoyle, B., Huterer, D., Jain, B., James, D. J., Jarvis, M., Jeltema, T., Johnson, M. D., Johnson, M. W. G., Kacprzak, T., Kent, S., Kim, A. G., King, A., Kirk, D., Kokron, N., Kovacs, A., Krause, E., Krawiec, C., Kremin, A., Kuehn, K., Kuhlmann, S., Kuropatkin, N., Lacasa, F., Lahav, O., Li, T. S., Liddle, A. R., Lidman, C., Lima, M., Lin, H., MacCrann, N., Maia, M. A. G., Makler, M., Manera, M., March, M., Marshall, J. L., Martini, P., McMahon, R. G., Melchior, P., Menanteau, F., Miquel, R., Miranda, V., Mudd, D., Muir, J., Möller, A., Neilsen, E., Nichol, R. C., Nord, B., Nugent, P., Ogando, R. L. C., Palmese, A., Peacock, J., Peiris, H. V., Peoples, J., Percival, W. J., Petravick, D., Plazas, A. A., Porredon, A., Prat, J., Pujol, A., Rau, M. M., Refregier, A., Ricker, P. M., Roe, N., Rollins, R. P., Romer, A. K., Roodman, A., Rosenfeld, R., Ross, A. J., Rozo, E., Rykoff, E. S., Sako, M., Salvador, A. I., Samuroff, S., Sánchez, C., Sanchez, E., Santiago, B., Scarpine, V., Schindler, R., Scolnic, D., Secco, L. F., Serrano, S., Sevilla-Noarbe, I., Sheldon, E., Smith, R. C., Smith, M., Smith, J., Soares-Santos, M., Sobreira, F., Suchyta, E., Tarle, G., Thomas, D., Troxel, M. A., Tucker, D. L., Tucker, B. E., Uddin, S. A., Varga, T. N., Vielzeuf, P., Vikram, V., Vivas, A. K., Walker, A. R., Wang, M., Wechsler, R. H., Weller, J., Wester, W., Wolf, R. C., Yanny, B., Yuan, F., Zenteno, A., Zhang, B., Zhang, Y., Zuntz, J., Dark Energy Survey Collaboration (2018), *Dark Energy Survey year 1 results: Cosmological constraints from galaxy clustering and weak lensing*, Phys. Rev. D, 98(4), 043526

Adamek, J., Angulo, R. E., Arnold, C., Baldi, M., Biagetti, M., Bose, B., Carbone, C., Castro, T., Dakin, J., Dolag, K., Elbers, W., Fidler, C., Giocoli, C., Hannestad, S., Hassani, F., Hernández-Aguayo, C., Koyama, K., Li, B., Mauland, R., Monaco, P., Moretti, C., Mota, D. F., Partmann, C., Parimbelli, G., Potter, D., Schneider, A., Schulz, S., Smith, R. E., Springel, V., Stadel, J., Tram, T., Viel, M., Villaescusa-Navarro, F., Winther, H. A., Wright, B. S., Zennaro, M., Aghanim, N., Amendola, L., Auricchio, N., Bonino, D., Branchini, E., Brescia, M., Camera, S., Capobianco, V., Cardone, V. F., Carretero, J., Castander, F. J., Castellano, M., Cavuoti, S., Cimatti, A., Cledassou, R., Congedo, G., Conversi, L., Copin, Y., Da Silva, A., Degaudenzi, H., Douspis, M., Dubath, F., Duncan, C. A. J., Dupac, X., Dusini, S., Farrens, S., Ferriol, S., Fosalba, P., Frailis, M., Franceschi, E., Galeotta, S., Garilli, B., Gillard, W., Gillis, B., Grazian, A., Haugan, S. V., Holmes, W., Hornstrup, A., Jahnke, K., Kermiche, S., Kiessling, A., Kilbinger, M., Kitching, T., Kunz, M., Kurki-Suonio, H., Lilje, P. B., Lloro, I., Mansutti,

O., Marggraf, O., Marulli, F., Massey, R., Medinaceli, E., Meneghetti, M., Meylan, G., Moresco, M., Moscardini, L., Munari, E., Niemi, S. M., Padilla, C., Paltani, S., Pasian, F., Pedersen, K., Percival, W. J., Pettorino, V., Polenta, G., Poncet, M., Popa, L. A., Raison, F., Rebolo, R., Renzi, A., Rhodes, J., Riccio, G., Romelli, E., Roncarelli, M., Saglia, R., Sapone, D., Sartoris, B., Schneider, P., Schrabback, T., Secroun, A., Seidel, G., Sirignano, C., Sirri, G., Stanco, L., Starck, J. L., Tallada-Crespí, P., Taylor, A. N., Tereno, I., Toledo-Moreo, R., Torradeflot, F., Tutusaus, I., Valenziano, L., Vassallo, T., Wang, Y., Weller, J., Zacchei, A., Zamorani, G., Zoubian, J., Fabbian, G., Scottez, V. (2022), *Euclid: Modelling massive neutrinos in cosmology – a code comparison*, arXiv e-prints, arXiv:2211.12457

Aihara, H., AlSayyad, Y., Ando, M., Armstrong, R., Bosch, J., Egami, E., Furusawa, H., Furusawa, J., Harasawa, S., Harikane, Y., Hsieh, B.-C., Ikeda, H., Ito, K., Iwata, I., Kodama, T., Koike, M., Kokubo, M., Komiyama, Y., Li, X., Liang, Y., Lin, Y.-T., Lupton, R. H., Lust, N. B., MacArthur, L. A., Mawatari, K., Mineo, S., Miyatake, H., Miyazaki, S., More, S., Morishima, T., Murayama, H., Nakajima, K., Nakata, F., Nishizawa, A. J., Oguri, M., Okabe, N., Okura, Y., Ono, Y., Osato, K., Ouchi, M., Pan, Y.-C., Malagón, A. A. P., Price, P. A., Reed, S. L., Rykoff, E. S., Shibuya, T., Simunovic, M., Strauss, M. A., Sugimori, K., Suto, Y., Suzuki, N., Takada, M., Takagi, Y., Takata, T., Takita, S., Tanaka, M., Tang, S., Taranu, D. S., Terai, T., Toba, Y., Turner, E. L., Uchiyama, H., Vijarnwannaluk, B., Waters, C. Z., Yamada, Y., Yamamoto, N., Yamashita, T. (2022), *Third data release of the Hyper Suprime-Cam Subaru Strategic Program*, PASJ, 74(2), 247

Akitsu, K., Kurita, T., Nishimichi, T., Takada, M., Tanaka, S. (2021), *Imprint of anisotropic primordial non-Gaussianity on halo intrinsic alignments in simulations*, Phys. Rev. D, 103(8), 083508

Akitsu, K., Li, Y., Okumura, T. (2023), *Gravitational wave fossils in nonlinear regime: Halo tidal bias and intrinsic alignments from gravitational wave separate universe simulations*, Phys. Rev. D, 107(6), 063531

Amendola, L., , Appleby, S., Avgoustidis, A., Bacon, D., Baker, T., Baldi, M., Bartolo, N., Blanchard, A., Bonvin, C., Borgani, S., Branchini, E., Burrage, C., Camera, S., Carbone, C., Casarini, L., Cropper, M., de Rham, C., Dietrich, J. P., Porto, C. D., Durrer, R., Ealet, A., Ferreira, P. G., Finelli, F., García-Bellido, J., Giannantonio, T., Guzzo, L., Heavens, A., Heisenberg, L., Heymans, C., Hoekstra, H., Hollenstein, L., Holmes, R., Hwang, Z., Jahnke, K., Kitching, T. D., Koivisto, T., Kunz, M., Vacca, G. L., Linder, E., March, M., Marra, V., Martins, C., Majerotto, E., Markovic, D., Marsh, D., Marulli, F., Massey, R., Mellier, Y., Montanari, F., Mota, D. F., Nunes, N. J., Percival, W., Pettorino, V., Porciani, C., Quercellini, C., Read, J., Rinaldi, M., Sapone, D., Sawicki, I., Scaramella, R., Skordis, C., Simpson, F., Taylor, A., Thomas, S., Trotta, R., Verde, L., Vernizzi, F., Vollmer, A., Wang, Y., Weller, J., Zlosnik, T. (2018), *Cosmology and fundamental physics with the Euclid satellite*, Living Reviews in Relativity, 21(1)

Angulo, R. E., Pontzen, A. (2016), *Cosmological N-body simulations with suppressed variance*, MNRAS, 462(1), L1

Bacon, D. J., Refregier, A. R., Ellis, R. S. (2000), *Detection of weak gravitational lensing by large-scale structure*, MNRAS, 318(2), 625

Bakx, T., Kurita, T., Elisa Chisari, N., Vlah, Z., Schmidt, F. (2023), *Effective field theory of intrinsic alignments at one loop order: a comparison to dark matter simulations*, J. Cosmology Astropart. Phys., 2023(10), 005

Barnett, A. H., Magland, J., af Klinteberg, L. (2019), *A Parallel Nonuniform Fast Fourier Transform Library Based on an "Exponential of Semicircle" Kernel*, SIAM Journal on Scientific Computing, 41(5), C479

Barreira, A., Llinares, C., Bose, S., Li, B. (2016), *RAY-RAMSES: a code for ray tracing on the fly in N-body simulations*, J. Cosmology Astropart. Phys., 2016(05), 001

Barrera, M., et al. (2022), *The MillenniumTNG Project: Semi-analytic galaxy formation models on the past lightcone*, ArXiv e-prints

Barrera, M., Springel, V., White, S. D. M., Hernández-Aguayo, C., Hernquist, L., Frenk, C., Pakmor, R., Ferlito, F., Hadzhiyska, B., Delgado, A. M., Kannan, R., Bose, S. (2023), *The MillenniumTNG Project: semi-analytic galaxy formation models on the past lightcone*, MNRAS, 525(4), 6312

Bartelmann, M., Schneider, P. (2001), *Weak gravitational lensing*, Physics Reports, 340(4-5), 291

Barthelemy, A., Codis, S., Bernardeau, F. (2020), *Post-Born corrections to the one-point statistics of (CMB) lensing convergence obtained via large deviation theory*, MNRAS, 494(3), 3368

Bate, J., Chisari, N. E., Codis, S., Martin, G., Dubois, Y., Devriendt, J., Pichon, C., Slyz, A. (2020), *When galaxies align: intrinsic alignments of the progenitors of elliptical galaxies in the Horizon-AGN simulation*, MNRAS, 491(3), 4057

Beaulieu, J. P., Bennett, D. P., Fouqué, P., Williams, A., Dominik, M., Jørgensen, U. G., Kubas, D., Cassan, A., Coutures, C., Greenhill, J., Hill, K., Menzies, J., Sackett, P. D., Albrow, M., Brillant, S., Caldwell, J. A. R., Calitz, J. J., Cook, K. H., Corrales, E., Desort, M., Dieters, S., Dominis, D., Donatowicz, J., Hoffman, M., Kane, S., Marquette, J. B., Martin, R., Meintjes, P., Pollard, K., Sahu, K., Vinter, C., Wambsganss, J., Woller, K., Horne, K., Steele, I., Bramich, D. M., Burgdorf, M., Snodgrass, C., Bode, M., Udalski, A., Szymański, M. K., Kubiak, M., Więckowski, T., Pietrzyński, G., Soszyński, I., Szewczyk, O., Wyrzykowski, Ł., Paczyński, B., Abe, F., Bond, I. A., Britton, T. R., Gilmore, A. C., Hearnshaw, J. B., Itow, Y., Kamiya, K., Kilmartin, P. M., Korpela, A. V., Masuda, K., Matsubara, Y., Motomura, M., Muraki, Y., Nakamura, S., Okada,

C., Ohnishi, K., Rattenbury, N. J., Sako, T., Sato, S., Sasaki, M., Sekiguchi, T., Sullivan, D. J., Tristram, P. J., Yock, P. C. M., Yoshioka, T. (2006), *Discovery of a cool planet of 5.5 Earth masses through gravitational microlensing*, Nature, 439(7075), 437

Bechtol, K., Sevilla-Noarbe, I., Drlica-Wagner, A., Yanny, B., Gruendl, R. A., Sheldon, E., Rykoff, E. S., De Vicente, J., Adamow, M., Anbajagane, D., Becker, M. R., Bernstein, G. M., Carnero Rosell, A., Gschwend, J., Gorsuch, M., Hartley, W. G., Jarvis, M., Jeltema, T., Kron, R., Manning, T. A., O'Donnell, J., Pieres, A., Rodríguez-Monroy, M., Sanchez Cid, D., Tabbutt, M., Toribio San Cipriano, L., Tucker, D. L., Weaverdyck, N., Yamamoto, M., Abbott, T. M. C., Aguena, M., Alarcón, A., Allam, S., Amon, A., Andrade-Oliveira, F., Avila, S., Bernardinelli, P. H., Bertin, E., Blazek, J., Brooks, D., Burke, D. L., Carretero, J., Castander, F. J., Cawthon, R., Chang, C., Choi, A., Conselice, C., Costanzi, M., Crocce, M., da Costa, L. N., Davis, T. M., Desai, S., Diehl, H. T., Dodelson, S., Doel, P., Doux, C., Ferté, A., Flaugher, B., Fosalba, P., Frieman, J., García-Bellido, J., Gatti, M., Gaztanaga, E., Giannini, G., Gruen, D., Gutierrez, G., Herner, K., Hinton, S. R., Hollowood, D. L., Honscheid, K., Huterer, D., Jeffrey, N., Krause, E., Kuehn, K., Lahav, O., Lee, S., Lidman, C., Lima, M., Lin, H., Marshall, J. L., Mena-Fernández, J., Miquel, R., Mohr, J. J., Muir, J., Myles, J., Ogando, R. L. C., Palmese, A., Plazas Malagón, A. A., Porredon, A., Prat, J., Raveri, M., Romer, A. K., Roodman, A., Samuroff, S., Sanchez, E., Scarpine, V., Smith, M., Soares-Santos, M., Suchyta, E., Tarle, G., Troxel, M. A., Vikram, V., Walker, A. R., Weller, J., Wiseman, P., Zhang, Y. (2025), *Dark Energy Survey Year 6 Results: Photometric Data Set for Cosmology*, arXiv e-prints, arXiv:2501.05739

Becker, M. R. (2013), *CALCLENS: weak lensing simulations for large-area sky surveys and second-order effects in cosmic shear power spectra*, MNRAS, 435(1), 115

Bernardeau, F. (1998), *The effects of source clustering on weak lensing statistics*, A&A, 338, 375

Bernstein, G. M., Jarvis, M. (2002), *Shapes and Shears, Stars and Smears: Optimal Measurements for Weak Lensing*, AJ, 123(2), 583

Bhowmick, A. K., Chen, Y., Tenneti, A., Di Matteo, T., Mandelbaum, R. (2020), *The evolution of galaxy intrinsic alignments in the MassiveBlackII universe*, MNRAS, 491(3), 4116

Binney, J., Tremaine, S. (2008), *Galactic Dynamics: Second Edition*, Princeton University Press, Princeton, NJ

Blandford, R., Narayan, R. (1986), *Fermat's Principle, Caustics, and the Classification of Gravitational Lens Images*, ApJ, 310, 568

Blas, D., Lesgourgues, J., Tram, T. (2011), *The Cosmic Linear Anisotropy Solving System (CLASS). Part II: Approximation schemes*, Journal of Cosmology and Astroparticle Physics, 2011(07), 034

Blazek, J. A., MacCrann, N., Troxel, M. A., Fang, X. (2019), *Beyond linear galaxy alignments*, Phys. Rev. D, 100(10), 103506

Bond, I. A., Udalski, A., Jaroszyński, M., Rattenbury, N. J., Paczyński, B., Soszyński, I., Wyrzykowski, L., Szymański, M. K., Kubiak, M., Szewczyk, O., Żebruń, K., Pietrzyński, G., Abe, F., Bennett, D. P., Eguchi, S., Furuta, Y., Hearnshaw, J. B., Kamiya, K., Kilmartin, P. M., Kurata, Y., Masuda, K., Matsubara, Y., Muraki, Y., Noda, S., Okajima, K., Sako, T., Sekiguchi, T., Sullivan, D. J., Sumi, T., Tristram, P. J., Yanagisawa, T., Yock, P. C. M., OGLE Collaboration (2004), *OGLE 2003-BLG-235/MOA 2003-BLG-53: A Planetary Microlensing Event*, ApJ, 606(2), L155

Boschetti, R., Vielzeuf, P., Cousinou, M.-C., Escoffier, S., Jullo, E. (2023), *Towards cosmology with Void Lensing: how to find voids sensitive to weak-lensing and numerically interpret them*, arXiv e-prints, arXiv:2311.14586

Bose, S., et al. (2022), *The MillenniumTNG Project: The large-scale clustering of galaxies*, ArXiv e-prints

Boyle, A., Uhlemann, C., Friedrich, O., Barthelemy, A., Codis, S., Bernardeau, F., Giocoli, C., Baldi, M. (2021), *Nuw CDM cosmology from the weak-lensing convergence PDF*, MNRAS, 505(2), 2886

Brainerd, T. G., Blandford, R. D., Smail, I. (1996), *Weak Gravitational Lensing by Galaxies*, ApJ, 466, 623

Bridle, S., King, L. (2007), *Dark energy constraints from cosmic shear power spectra: impact of intrinsic alignments on photometric redshift requirements*, New Journal of Physics, 9(12), 444

Broxterman, J. C., Schaller, M., Schaye, J., Hoekstra, H., Kuijken, K., Helly, J. C., Kugel, R., Braspenning, J., Elbers, W., Frenk, C. S., Kwan, J., McCarthy, I. G., Salcido, J., van Daalen, M. P., Vandenbroucke, B. (2024), *The FLAMINGO project: baryonic impact on weak gravitational lensing convergence peak counts*, MNRAS, 529(3), 2309

Cai, Y.-C., Bernstein, G. (2012), *Combining weak-lensing tomography and spectroscopic redshift surveys*, MNRAS, 422(2), 1045

Carones, A., CarrónDuque, J., Marinucci, D., Migliaccio, M., Vittorio, N. (2024), *Minkowski functionals of CMB polarization intensity with PYNKOWSKI: theory and application to Planck and future data*, MNRAS, 527(1), 756

Castro, P. G., Heavens, A. F., Kitching, T. D. (2005), *Weak lensing analysis in three dimensions*, Phys. Rev. D, 72(2), 023516

Catelan, P., Kamionkowski, M., Blandford, R. D. (2001), *Intrinsic and extrinsic galaxy alignment*, MNRAS, 320(1), L7

Chen, S.-F., Kokron, N. (2024), *A Lagrangian theory for galaxy shape statistics*, J. Cosmology Astropart. Phys., 2024(1), 027

Chisari, N., Codis, S., Laigle, C., Dubois, Y., Pichon, C., Devriendt, J., Slyz, A., Miller, L., Gavazzi, R., Benabed, K. (2015), *Intrinsic alignments of galaxies in the Horizon-AGN cosmological hydrodynamical simulation*, MNRAS, 454(3), 2736

Chisari, N. E., Alonso, D., Krause, E., Leonard, C. D., Bull, P., Neveu, J., Villarreal, A. S., Singh, S., McClintock, T., Ellison, J., Du, Z., Zuntz, J., Mead, A., Joudaki, S., Lorenz, C. S., Tröster, T., Sanchez, J., Lanusse, F., Ishak, M., Hlozek, R., Blazek, J., Campagne, J.-E., Almoubayyed, H., Eifler, T., Kirby, M., Kirkby, D., Plaszczynski, S., Slosar, A., Vrastil, M., Wagoner, E. L., LSST Dark Energy Science Collaboration (2019), *Core Cosmology Library: Precision Cosmological Predictions for LSST*, ApJS, 242(1), 2

Chisari, N. E., Dvorkin, C. (2013), *Cosmological information in the intrinsic alignments of luminous red galaxies*, J. Cosmology Astropart. Phys., 2013(12), 029

Clowe, D., Bradač, M., Gonzalez, A. H., Markevitch, M., Randall, S. W., Jones, C., Zaritsky, D. (2006), *A Direct Empirical Proof of the Existence of Dark Matter*, ApJ, 648(2), L109

Contreras, S., et al. (2022), *The MillenniumTNG Project: Inferring cosmology from galaxy clustering with accelerated N-body scaling and subhalo abundance matching*, ArXiv e-prints

Conway, J. H., Guy, R. K. (1996), *The Book of Numbers*, Copernicus New York, NY

Cooray, A., Hu, W. (2002), *Second-Order Corrections to Weak Lensing by Large-Scale Structure*, ApJ, 574(1), 19

Cooray, A. R. (1999), *Weighing neutrinos: weak lensing approach*, A&A, 348, 31

Coulton, W. R., Liu, J., McCarthy, I. G., Osato, K. (2020), *Weak lensing minima and peaks: Cosmological constraints and the impact of baryons*, MNRAS, 495(3), 2531

Dalcin, L., Fang, Y.-L. L. (2021), *mpi4py: Status Update After 12 Years of Development*, Computing in Science & Engineering, 23(4), 47

Das, S., Bode, P. (2008), *A Large Sky Simulation of the Gravitational Lensing of the Cosmic Microwave Background*, ApJ, 682(1), 1

Davies, C. T., Cautun, M., Giblin, B., Li, B., Harnois-Déraps, J., Cai, Y.-C. (2021), *Constraining cosmology with weak lensing voids*, MNRAS, 507(2), 2267

Davies, C. T., Cautun, M., Giblin, B., Li, B., Harnois-Déraps, J., Cai, Y.-C. (2022), *Cosmological forecasts with the clustering of weak lensing peaks*, MNRAS, 513(4), 4729

Davies, C. T., Cautun, M., Li, B. (2018), *Weak lensing by voids in weak lensing maps*, MNRAS, 480(1), L101

Davies, C. T., Cautun, M., Li, B. (2019), *The self-similarity of weak lensing peaks*, MNRAS, 488(4), 5833

Davis, M., Efstathiou, G., Frenk, C. S., White, S. D. M. (1985), *The evolution of large-scale structure in a universe dominated by cold dark matter*, ApJ, 292, 371

Delgado, A. M., et al. (2023), *The MillenniumTNG Project: Intrinsic alignments of galaxies and halos*, ArXiv e-prints

Delgado, A. M., Hadzhiyska, B., Bose, S., Springel, V., Hernquist, L., Barrera, M., Pakmor, R., Ferlito, F., Kannan, R., Hernández-Aguayo, C., White, S. D. M., Frenk, C. (2023), *The MillenniumTNG project: intrinsic alignments of galaxies and haloes*, MNRAS, 523(4), 5899

Ducout, A., Bouchet, F. R., Colombi, S., Pogosyan, D., Prunet, S. (2013), *Non-Gaussianity and Minkowski functionals: forecasts for Planck*, MNRAS, 429(3), 2104

Dyson, F. J. (1998), *Critical Problems in Physics.*, American Journal of Physics, 66(9), 837

Dyson, F. W., Eddington, A. S., Davidson, C. (1920), *A Determination of the Deflection of Light by the Sun's Gravitational Field, from Observations Made at the Total Eclipse of May 29, 1919*, Philosophical Transactions of the Royal Society of London Series A, 220, 291

Eddington, A. S. (1920), *Space, time and gravitation. an outline of the general relativity theory*, Cambridge University Press

Einstein, A. (1915), *Zur allgemeinen Relativitätstheorie*, Sitzungsberichte der Königlich Preussischen Akademie der Wissenschaften, 778–786

Einstein, A. (1936), *Lens-Like Action of a Star by the Deviation of Light in the Gravitational Field*, Science, 84(2188), 506

Elbers, W., Frenk, C. S., Jenkins, A., Li, B., Pascoli, S. (2021), *An optimal non-linear method for simulating relic neutrinos*, MNRAS, 507(2), 2614

Euclid Collaboration, Aussel, H., Tereno, I., Schirmer, M., Alguero, G., Altieri, B., Balbinot, E., de Boer, T., Casenove, P., Corcho-Caballero, P., Furusawa, H., Furusawa, J., Hudson, M. J., Jahnke, K., Libet, G., Macias-Perez, J., Masoumzadeh, N., Mohr, J. J., Odier, J., Scott, D., Vassallo, T., Verdoes Kleijn, G., Zacchei, A., Aghanim, N., Amara, A., Andreon, S., Auricchio, N., Awan, S., Azzollini, R., Baccigalupi, C., Baldi, M., Balestra, A., Bardelli, S., Basset, A., Battaglia, P., Belikov, A. N., Bender, R., Biviano, A., Bonchi, A., Bonino, D., Branchini, E., Brescia, M., Brinchmann, J., Camera, S.,

Cañas-Herrera, G., Capobianco, V., Carbone, C., Cardone, V. F., Carretero, J., Casas, S., Castander, F. J., Castellano, M., Castignani, G., Cavuoti, S., Chambers, K. C., Cimatti, A., Colodro-Conde, C., Congedo, G., Conselice, C. J., Conversi, L., Copin, Y., Courbin, F., Courtois, H. M., Cropper, M., Cuby, J. G., Da Silva, A., da Silva, R., Degaudenzi, H., de Jong, J. T. A., De Lucia, G., Di Giorgio, A. M., Dinis, J., Dolding, C., Dole, H., Douspis, M., Dubath, F., Duncan, C. A. J., Dupac, X., Dusini, S., Ealet, A., Escoffier, S., Fabricius, M., Farina, M., Farinelli, R., Faustini, F., Ferriol, S., Fotopoulou, S., Fourmanoit, N., Frailis, M., Franceschi, E., Franzetti, P., Galeotta, S., George, K., Gillard, W., Gillis, B., Giocoli, C., Gómez-Alvarez, P., Gracia-Carpio, J., Granett, B. R., Grazian, A., Grupp, F., Guzzo, L., Gwyn, S., Haugan, S. V. H., Herent, O., Hoar, J., Hoekstra, H., Holliman, M. S., Holmes, W., Hook, I. M., Hormuth, F., Hornstrup, A., Hudelot, P., Ilić, S., Jhabvala, M., Joachimi, B., Keihänen, E., Kermiche, S., Kiessling, A., Kubik, B., Kuijken, K., Kümmel, M., Kunz, M., Kurki-Suonio, H., Lahav, O., Le Boulc'h, Q., Le Brun, A. M. C., Le Mignant, D., Liebing, P., Ligori, S., Lilje, P. B., Lindholm, V., Lloro, I., Mainetti, G., Maino, D., Maiorano, E., Mansutti, O., Marcin, S., Marggraf, O., Markovic, K., Martinelli, M., Martinet, N., Marulli, F., Massey, R., Maurogordato, S., McCracken, H. J., Medinaceli, E., Mei, S., Melchior, M., Mellier, Y., Meneghetti, M., Merlin, E., Meylan, G., Mora, A., Moresco, M., Morris, P. W., Moscardini, L., Mourre, S., Nakajima, R., Neissner, C., Nichol, R. C., Niemi, S. M., Nightingale, J. W., Nutma, T., Padilla, C., Paltani, S., Pasian, F., Peacock, J. A., Pedersen, K., Percival, W. J., Pettorino, V., Pires, S., Polenta, G., Pollack, J. E., Poncet, M., Popa, L. A., Pozzetti, L., Racca, G. D., Raison, F., Rebolo, R., Renzi, A., Rhodes, J., Riccio, G., Rix, H. W., Romelli, E., Roncarelli, M., Rossetti, E., Rusholme, B., Saglia, R., Sakr, Z., Sánchez, A. G., Sapone, D., Sartoris, B., Sauvage, M., Schewtschenko, J. A., Schneider, P., Scodeggio, M., Secroun, A., Sefusatti, E., Seidel, G. (2025), *Euclid Quick Data Release (Q1) – Data release overview*, arXiv e-prints, arXiv:2503.15302

Fabbian, G., Calabrese, M., Carbone, C. (2018), *CMB weak-lensing beyond the Born approximation: a numerical approach*, J. Cosmology Astropart. Phys., 2018(02), 050

Fabbian, G., Lewis, A., Beck, D. (2019), *CMB lensing reconstruction biases in cross-correlation with large-scale structure probes*, J. Cosmology Astropart. Phys., 2019(10), 057

Ferlito, F., Davies, C. T., Springel, V., Reinecke, M., Greco, A., Delgado, A. M., White, S. D. M., Hernández-Aguayo, C., Bose, S., Hernquist, L. (2024), *Ray-tracing versus Born approximation in full-sky weak lensing simulations of the MillenniumTNG project*, MNRAS, 533(3), 3209

Ferlito, F., Springel, V., Davies, C. T., Hernández-Aguayo, C., Pakmor, R., Barrera, M., White, S. D. M., Delgado, A. M., Hadzhiyska, B., Hernquist, L., Kannan, R., Bose, S., Frenk, C. (2023), *The MillenniumTNG Project: the impact of baryons and massive neutrinos on high-resolution weak gravitational lensing convergence maps*, MNRAS, 524(4), 5591

Fessler, J. A., Sutton, B. P. (2003), *Nonuniform fast fourier transforms using min-max interpolation*, IEEE Transactions on Signal Processing, 51(2), 560

Fong, M., Choi, M., Catlett, V., Lee, B., Peel, A., Bowyer, R., King, L. J., McCarthy, I. G. (2019), *The impact of baryonic physics and massive neutrinos on weak lensing peak statistics*, MNRAS, 488(3), 3340

Fortuna, M. C., Hoekstra, H., Joachimi, B., Johnston, H., Chisari, N. E., Georgiou, C., Mahony, C. (2021), *The halo model as a versatile tool to predict intrinsic alignments*, MNRAS, 501(2), 2983

Frittelli, S., Kling, T. P. (2011), *Accuracy of the thin-lens approximation in strong lensing by smoothly truncated dark matter haloes*, MNRAS, 415(4), 3599

Górski, K. M., Hivon, E., Banday, A. J., Wandelt, B. D., Hansen, F. K., Reinecke, M., Bartelmann, M. (2005), *HEALPix: A Framework for High-Resolution Discretization and Fast Analysis of Data Distributed on the Sphere*, ApJ, 622(2), 759

Gouin, C., Gavazzi, R., Pichon, C., Dubois, Y., Laigle, C., Chisari, N. E., Codis, S., Devriendt, J., Peirani, S. (2019), *Weak lensing in the Horizon-AGN simulation lightcone*, A&A, 626, A72

Grewal, N., Zuntz, J., Tröster, T., Amon, A. (2022), *Minkowski Functionals in Joint Galaxy Clustering & Weak Lensing Analyses*, The Open Journal of Astrophysics, 5(1), 13

Hadzhiyska, B., et al. (2022a), *The MillenniumTNG Project: An improved two-halo model for the galaxy-halo connection of red and blue galaxies*, ArXiv e-prints

Hadzhiyska, B., et al. (2022b), *The MillenniumTNG Project: Refining the one-halo model of red and blue galaxies at different redshifts*, ArXiv e-prints

Hadzhiyska, B., Yuan, S., Blake, C., Eisenstein, D. J., Aguilar, J., Ahlen, S., Brooks, D., Claybaugh, T., de la Macorra, A., Doel, P., Emas, N., Forero-Romero, J. E., Garcia-Quintero, C., Ishak, M., Joudaki, S., Jullo, E., Kehoe, R., Kisner, T., Kremin, A., Krolewski, A., Landriau, M., Lange, J. U., Manera, M., Miquel, R., Nie, J., Poppett, C., Porredon, A., Rossi, G., Ruggeri, R., Saulder, C., Schubnell, M., Tarlé, G., Weaver, B. A., Xhakaj, E., Zhou, Z. (2023), *Synthetic light-cone catalogues of modern redshift and weak lensing surveys waith ABACUSSUMMIT*, MNRAS, 525(3), 4367

Hadzhiyska, B., Yuan, S., Blake, C., Eisenstein, D. J., Aguilar, J. N., Ahlen, S., Brooks, D., Claybaugh, T., de la Macorra, A., Doel, P., Emas, N. P. A., Forero-Romero, J. E., Garcia-Quintero, C., Ishak, M., Joudaki, S., Jullo, E., Kehoe, R., Kisner, T., Kremin, A., Krolewski, A., Landriau, M., Lange, J. U., Manera, M., Miquel, R., Nie, J., Poppett, C., Porredon, A., Rossi, G., Ruggeri, R., Saulder, C., Schubnell, M., Tarlé, G., Weaver, B. A., Xhakaj, E., Zhou, Z. (2023), *Synthetic light cone catalogues of modern redshift and weak lensing surveys with AbacusSummit*

Halder, A., Barreira, A., Gong, Z., Seitz, S., Friedrich, O. (2023), *The integrated 3-point correlation function of cosmic shear*, in *American Astronomical Society Meeting Abstracts*, volume 241 of *American Astronomical Society Meeting Abstracts*, 244.05

Harnois-Déraps, J., Giblin, B., Joachimi, B. (2019), *Cosmic shear covariance matrix in wCDM: Cosmology matters*, A&A, 631, A160

Harnois-Déraps, J., Martinet, N., Reischke, R. (2022), *Cosmic shear beyond 2-point statistics: Accounting for galaxy intrinsic alignment with projected tidal fields*, MNRAS, 509(3), 3868

Heavens, A., Refregier, A., Heymans, C. (2000), *Intrinsic correlation of galaxy shapes: implications for weak lensing measurements*, MNRAS, 319(2), 649

Hernández-Aguayo, C., Springel, V., Pakmor, R., Barrera, M., Ferlito, F., White, S. D. M., Hernquist, L., Hadzhiyska, B., Delgado, A. M., Kannan, R., Bose, S., Frenk, C. (2022), *The MillenniumTNG Project: High-precision predictions for matter clustering and halo statistics*, arXiv e-prints, arXiv:2210.10059

Hernández-Aguayo, C., Springel, V., Pakmor, R., Barrera, M., Ferlito, F., White, S. D. M., Hernquist, L., Hadzhiyska, B., Delgado, A. M., Kannan, R., Bose, S., Frenk, C. (2023), *The MillenniumTNG Project: high-precision predictions for matter clustering and halo statistics*, MNRAS, 524(2), 2556

Hernández-Aguayo, C., Springel, V., Bose, S., Frenk, C., Jenkins, A., Barrera, M., Ferlito, F., Pakmor, R., White, S. D. M., Hernquist, L., Delgado, A. M., Kannan, R., Hadzhiyska, B. (2024), *The MillenniumTNG Project: Impact of massive neutrinos on the cosmic large-scale structure and the distribution of galaxies*, arxiv

Heymans, C., Tröster, T., Asgari, M., Blake, C., Hildebrandt, H., Joachimi, B., Kuijken, K., Lin, C.-A., Sá nchez, A. G., van den Busch, J. L., Wright, A. H., Amon, A., Bilicki, M., de Jong, J., Crocce, M., Dvornik, A., Erben, T., Fortuna, M. C., Getman, F., Giblin, B., Glazebrook, K., Hoekstra, H., Joudaki, S., Kannawadi, A., Köhlinger, F., Lidman, C., Miller, L., Napolitano, N. R., Parkinson, D., Schneider, P., Shan, H., Valentijn, E. A., Kleijn, G. V., Wolf, C. (2021), *KiDS-1000 Cosmology: Multi-probe weak gravitational lensing and spectroscopic galaxy clustering constraints*, A&A, 646, A140

Hikage, C., Coles, P., Grossi, M., Moscardini, L., Dolag, K., Branchini, E., Matarrese, S. (2008), *The effect of primordial non-Gaussianity on the topology of large-scale structure*, MNRAS, 385(3), 1613

Hikage, C., Oguri, M., Hamana, T., More, S., Mandelbaum, R., Takada, M., Köhlinger, F., Miyatake, H., Nishizawa, A. J., Aihara, H., Armstrong, R., Bosch, J., Coupon, J., Ducout, A., Ho, P., Hsieh, B.-C., Komiyama, Y., Lanusse, F., Leauthaud, A., Lupton, R. H., Medezinski, E., Mineo, S., Miyama, S., Miyazaki, S., Murata, R., Murayama, H., Shirasaki, M., Sifón, C., Simet, M., Speagle, J., Spergel, D. N., Strauss, M. A.,

Sugiyama, N., Tanaka, M., Utsumi, Y., Wang, S.-Y., Yamada, Y. (2019), *Cosmology from cosmic shear power spectra with Subaru Hyper Suprime-Cam first-year data*, PASJ, 71(2), 43

Hilbert, S., Barreira, A., Fabbian, G., Fosalba, P., Giocoli, C., Bose, S., Calabrese, M., Carbone, C., Davies, C. T., Li, B., Llinares, C., Monaco, P. (2020), *The accuracy of weak lensing simulations*, MNRAS, 493(1), 305

Hilbert, S., Hartlap, J., White, S. D. M., Schneider, P. (2009), *Ray-tracing through the Millennium Simulation: Born corrections and lens-lens coupling in cosmic shear and galaxy-galaxy lensing*, A&A, 499(1), 31

Hilbert, S., Xu, D., Schneider, P., Springel, V., Vogelsberger, M., Hernquist, L. (2017), *Intrinsic alignments of galaxies in the Illustris simulation*, MNRAS, 468(1), 790

Hildebrandt, H., van den Busch, J. L., Wright, A. H., Blake, C., Joachimi, B., Kuijken, K., Tröster, T., Asgari, M., Bilicki, M., de Jong, J. T. A., Dvornik, A., Erben, T., Getman, F., Giblin, B., Heymans, C., Kannawadi, A., Lin, C. A., Shan, H. Y. (2021), *KiDS-1000 catalogue: Redshift distributions and their calibration*, A&A, 647, A124

Hildebrandt, H., Viola, M., Heymans, C., Joudaki, S., Kuijken, K., Blake, C., Erben, T., Joachimi, B., Klaes, D., Miller, L., Morrison, C. B., Nakajima, R., Kleijn, G. V., Amon, A., Choi, A., Covone, G., de Jong, J. T. A., Dvornik, A., Conti, I. F., Grado, A., Harnois-Dé raps, J., Herbonnet, R., Hoekstra, H., Köhlinger, F., McFarland, J., Mead, A., Merten, J., Napolitano, N., Peacock, J. A., Radovich, M., Schneider, P., Simon, P., Valentijn, E. A., van den Busch, J. L., van Uitert, E., Waerbeke, L. V. (2016), *KiDS-450: cosmological parameter constraints from tomographic weak gravitational lensing*, MNRAS, 465(2), 1454

Hirata, C. M., Mandelbaum, R., Ishak, M., Seljak, U., Nichol, R., Pimbblet, K. A., Ross, N. P., Wake, D. (2007), *Intrinsic galaxy alignments from the 2SLAQ and SDSS surveys: luminosity and redshift scalings and implications for weak lensing surveys*, MNRAS, 381(3), 1197

Hirata, C. M., Seljak, U. (2004), *Intrinsic alignment-lensing interference as a contaminant of cosmic shear*, Phys. Rev. D, 70(6), 063526

Hivon, E., Hansen, F. K., Banday, A. J. (1999), *The healpix primer*, astro-ph, 9905275

Hoekstra, H., Jain, B. (2008), *Weak Gravitational Lensing and Its Cosmological Applications*, Annual Review of Nuclear and Particle Science, 58(1), 99

Hu, W. (2000), *Weak lensing of the CMB: A harmonic approach*, Phys. Rev. D, 62(4), 043007

Huff, E., Mandelbaum, R. (2017), *Metacalibration: Direct Self-Calibration of Biases in Shear Measurement*, arXiv e-prints, arXiv:1702.02600

Irwin, M. J., Webster, R. L., Hewett, P. C., Corrigan, R. T., Jedrzejewski, R. I. (1989), *Photometric Variations in the Q2237+0305 System: First Detection of a Microlensing Event*, AJ, 98, 1989

Jain, B., Seljak, U., White, S. (2000), *Ray-tracing Simulations of Weak Lensing by Large-Scale Structure*, ApJ, 530(2), 547

Jarvis, M. (2015), *TreeCorr: Two-point correlation functions*, Astrophysics Source Code Library, record ascl:1508.007

Jing, Y. P., Zhang, P., Lin, W. P., Gao, L., Springel, V. (2006), *The Influence of Baryons on the Clustering of Matter and Weak-Lensing Surveys*, ApJ, 640(2), L119

Joachimi, B., Bridle, S. L. (2010), *Simultaneous measurement of cosmology and intrinsic alignments using joint cosmic shear and galaxy number density correlations*, A&A, 523, A1

Joachimi, B., Cacciato, M., Kitching, T. D., Leonard, A., Mandelbaum, R., Schäfer, B. M., Sifón, C., Hoekstra, H., Kiessling, A., Kirk, D., Rassat, A. (2015), *Galaxy Alignments: An Overview*, Space Sci. Rev., 193(1-4), 1

Joachimi, B., Mandelbaum, R., Abdalla, F. B., Bridle, S. L. (2011), *Constraints on intrinsic alignment contamination of weak lensing surveys using the MegaZ-LRG sample*, A&A, 527, A26

Joachimi, B., Semboloni, E., Hilbert, S., Bett, P. E., Hartlap, J., Hoekstra, H., Schneider, P. (2013), *Intrinsic galaxy shapes and alignments - II. Modelling the intrinsic alignment contamination of weak lensing surveys*, MNRAS, 436(1), 819

Kaiser, N. (1992), *Weak Gravitational Lensing of Distant Galaxies*, ApJ, 388, 272

Kaiser, N., Squires, G. (1993), *Mapping the Dark Matter with Weak Gravitational Lensing*, ApJ, 404, 441

Kaiser, N., Squires, G., Broadhurst, T. (1995), *A Method for Weak Lensing Observations*, ApJ, 449, 460

Kaiser, N., Wilson, G., Luppino, G. A. (2000), *Large-Scale Cosmic Shear Measurements*, arXiv e-prints, astro–ph/0003338

Kannan, R., et al. (2022), *The MilleniumTNG Project: The galaxy population at $z \geq 8$*, ArXiv e-prints

Kiessling, A., Cacciato, M., Joachimi, B., Kirk, D., Kitching, T. D., Leonard, A., Mandelbaum, R., Schäfer, B. M., Sifón, C., Brown, M. L., Rassat, A. (2015), *Galaxy Alignments: Theory, Modelling & Simulations*, Space Sci. Rev., 193(1-4), 67

Kilbinger, M. (2015), *Cosmology with cosmic shear observations: a review*, Reports on Progress in Physics, 78(8), 086901

Kirk, D., Brown, M. L., Hoekstra, H., Joachimi, B., Kitching, T. D., Mandelbaum, R., Sifón, C., Cacciato, M., Choi, A., Kiessling, A., Leonard, A., Rassat, A., Schäfer, B. M. (2015), *Galaxy Alignments: Observations and Impact on Cosmology*, Space Sci. Rev., 193(1-4), 139

Kitching, T. D., Heavens, A. F., Verde, L., Serra, P., Melchiorri, A. (2008), *Finding evidence for massive neutrinos using 3D weak lensing*, Phys. Rev. D, 77(10), 103008

Kurita, T., Takada, M. (2023), *Constraints on anisotropic primordial non-Gaussianity from intrinsic alignments of SDSS-III BOSS galaxies*, Phys. Rev. D, 108(8), 083533

Kurita, T., Takada, M., Nishimichi, T., Takahashi, R., Osato, K., Kobayashi, Y. (2021), *Power spectrum of halo intrinsic alignments in simulations*, MNRAS, 501(1), 833

Lamman, C., Tsaprazi, E., Shi, J., Šarčević, N. N., Pyne, S., Legnani, E., Ferreira, T. (2024), *The IA Guide: A Breakdown of Intrinsic Alignment Formalisms*, The Open Journal of Astrophysics, 7, 14

Lee, M. E., Haiman, Z., Pandey, S., Genel, S. (2025), *The effect of intrinsic alignments on weak lensing statistics in hydrodynamical simulations*, arXiv e-prints, arXiv:2504.12460

Lemos, P., Challinor, A., Efstathiou, G. (2017), *The effect of Limber and flat-sky approximations on galaxy weak lensing*, J. Cosmology Astropart. Phys., 2017(5), 014

Lesgourgues, J., Pastor, S. (2006), *Massive neutrinos and cosmology*, Physics Reports, 429(6), 307

Liaudat, T. I., Starck, J.-L., Kilbinger, M. (2023), *Point spread function modelling for astronomical telescopes: a review focused on weak gravitational lensing studies*, Frontiers in Astronomy and Space Sciences, 10, 1158213

Limber, D. N. (1953), *The Analysis of Counts of the Extragalactic Nebulae in Terms of a Fluctuating Density Field.*, ApJ, 117, 134

Liu, J., Bird, S., Matilla, J. M. Z., Hill, J. C., Haiman, Z., Madhavacheril, M. S., Petri, A., Spergel, D. N. (2018), *MassiveNuS: cosmological massive neutrino simulations*, J. Cosmology Astropart. Phys., 2018(03), 049

Liu, J., Haiman, Z. (2016), *Origin of weak lensing convergence peaks*, Physical Review D, 94(4)

Liu, J., Madhavacheril, M. S. (2019), *Constraining neutrino mass with the tomographic weak lensing one-point probability distribution function and power spectrum*, Physical Review D, 99(8), 083508

Lodge, O. J. (1919), *Gravitation and Light*, Nature, 104(2614), 354

LoVerde, M., Afshordi, N. (2008), *Extended Limber approximation*, Phys. Rev. D, 78, 123506

LSST Science Collaboration, Abell, P. A., Allison, J., Anderson, S. F., Andrew, J. R., Angel, J. R. P., Armus, L., Arnett, D., Asztalos, S. J., Axelrod, T. S., Bailey, S., Ballantyne, D. R., Bankert, J. R., Barkhouse, W. A., Barr, J. D., Barrientos, L. F., Barth, A. J., Bartlett, J. G., Becker, A. C., Becla, J., Beers, T. C., Bernstein, J. P., Biswas, R., Blanton, M. R., Bloom, J. S., Bochanski, J. J., Boeshaar, P., Borne, K. D., Bradac, M., Brandt, W. N., Bridge, C. R., Brown, M. E., Brunner, R. J., Bullock, J. S., Burgasser, A. J., Burge, J. H., Burke, D. L., Cargile, P. A., Chandrasekharan, S., Chartas, G., Chesley, S. R., Chu, Y.-H., Cinabro, D., Claire, M. W., Claver, C. F., Clowe, D., Connolly, A. J., Cook, K. H., Cooke, J., Cooray, A., Covey, K. R., Culliton, C. S., de Jong, R., de Vries, W. H., Debattista, V. P., Delgado, F., Dell'Antonio, I. P., Dhital, S., Di Stefano, R., Dickinson, M., Dilday, B., Djorgovski, S. G., Dobler, G., Donalek, C., Dubois-Felsmann, G., Durech, J., Eliasdottir, A., Eracleous, M., Eyer, L., Falco, E. E., Fan, X., Fassnacht, C. D., Ferguson, H. C., Fernandez, Y. R., Fields, B. D., Finkbeiner, D., Figueroa, E. E., Fox, D. B., Francke, H., Frank, J. S., Frieman, J., Fromenteau, S., Furqan, M., Galaz, G., Gal-Yam, A., Garnavich, P., Gawiser, E., Geary, J., Gee, P., Gibson, R. R., Gilmore, K., Grace, E. A., Green, R. F., Gressler, W. J., Grillmair, C. J., Habib, S., Haggerty, J. S., Hamuy, M., Harris, A. W., Hawley, S. L., Heavens, A. F., Hebb, L., Henry, T. J., Hileman, E., Hilton, E. J., Hoadley, K., Holberg, J. B., Holman, M. J., Howell, S. B., Infante, L., Ivezic, Z., Jacoby, S. H., Jain, B., R, Jedicke, Jee, M. J., Garrett Jernigan, J., Jha, S. W., Johnston, K. V., Jones, R. L., Juric, M., Kaasalainen, M., Styliani, Kafka, Kahn, S. M., Kaib, N. A., Kalirai, J., Kantor, J., Kasliwal, M. M., Keeton, C. R., Kessler, R., Knezevic, Z., Kowalski, A., Krabbendam, V. L., Krughoff, K. S., Kulkarni, S., Kuhlman, S., Lacy, M., Lepine, S., Liang, M., Lien, A., Lira, P., Long, K. S., Lorenz, S., Lotz, J. M., Lupton, R. H., Lutz, J., Macri, L. M., Mahabal, A. A., Mandelbaum, R., Marshall, P., May, M., McGehee, P. M., Meadows, B. T., Meert, A., Milani, A., Miller, C. J., Miller, M., Mills, D., Minniti, D., Monet, D., Mukadam, A. S., Nakar, E., Neill, D. R., Newman, J. A., Nikolaev, S., Nordby, M., O'Connor, P., Oguri, M., Oliver, J., Olivier, S. S., Olsen, J. K., Olsen, K., Olszewski, E. W., Oluseyi, H., Padilla, N. D., Parker, A., Pepper, J., Peterson, J. R., Petry, C., Pinto, P. A., Pizagno, J. L., Popescu, B., Prsa, A., Radcka, V., Raddick, M. J., Rasmussen, A., Rau, A., Rho, J., Rhoads, J. E., Richards, G. T., Ridgway, S. T., Robertson, B. E., Roskar, R., Saha, A., Sarajedini, A., Scannapieco, E., Schalk, T., Schindler, R., Schmidt, S. (2009), *LSST Science Book, Version 2.0*, arXiv e-prints, arXiv:0912.0201

Lynden-Bell, D. (1967), *Statistical mechanics of violent relaxation in stellar systems*, MNRAS, 136, 101

Lynds, R., Petrosian, V. (1986), *Giant Luminous Arcs in Galaxy Clusters*, in *Bulletin of the American Astronomical Society*, volume 18, 1014

Maion, F., Angulo, R. E., Bakx, T., Chisari, N. E., Kurita, T., Pellejero-Ibáñez, M. (2024), *HYMALAIA: a hybrid lagrangian model for intrinsic alignments*, MNRAS, 531(2), 2684

Mandelbaum, R. (2018), *Weak Lensing for Precision Cosmology*, ARA&A, 56(1), 393

Mandelbaum, R., Seljak, U., Hirata, C. M., Bardelli, S., Bolzonella, M., Bongiorno, A., Carollo, M., Contini, T., Cunha, C. E., Garilli, B., Iovino, A., Kampczyk, P., Kneib, J. P., Knobel, C., Koo, D. C., Lamareille, F., Le Fèvre, O., Le Borgne, J. F., Lilly, S. J., Maier, C., Mainieri, V., Mignoli, M., Newman, J. A., Oesch, P. A., Perez-Montero, E., Ricciardelli, E., Scodeggio, M., Silverman, J., Tasca, L. (2008), *Precision photometric redshift calibration for galaxy-galaxy weak lensing*, MNRAS, 386(2), 781

Marinacci, F., Vogelsberger, M., Pakmor, R., Torrey, P., Springel, V., Hernquist, L., Nelson, D., Weinberger, R., Pillepich, A., Naiman, J., Genel, S. (2018), *First results from the IllustrisTNG simulations: radio haloes and magnetic fields*, MNRAS, 480(4), 5113

Marques, G. A., Liu, J., Shirasaki, M., Thiele, L., Grandón, D., Huffenberger, K. M., Cheng, S., Harnois-Déraps, J., Osato, K., Coulton, W. R. (2024), *Cosmology from weak lensing peaks and minima with Subaru Hyper Suprime-Cam Survey first-year data*, MNRAS, 528(3), 4513

Martinet, N., Harnois-Déraps, J., Jullo, E., Schneider, P. (2021), *Probing dark energy with tomographic weak-lensing aperture mass statistics*, A&A, 646, A62

Martinet, N., Schneider, P., Hildebrandt, H., Shan, H., Asgari, M., Dietrich, J. P., Harnois-Déraps, J., Erben, T., Grado, A., Heymans, C., Hoekstra, H., Klaes, D., Kuijken, K., Merten, J., Nakajima, R. (2018), *KiDS-450: cosmological constraints from weak-lensing peak statistics - II: Inference from shear peaks using N-body simulations*, MNRAS, 474(1), 712

Miller, L., Kitching, T. D., Heymans, C., Heavens, A. F., van Waerbeke, L. (2007), *Bayesian galaxy shape measurement for weak lensing surveys - I. Methodology and a fast-fitting algorithm*, MNRAS, 382(1), 315

Miralda-Escude, J. (1991), *The Correlation Function of Galaxy Ellipticities Produced by Gravitational Lensing*, ApJ, 380, 1

Mroz, P., Poleski, R. (2023), *Exoplanet Occurrence Rates from Microlensing Surveys*, arXiv e-prints, arXiv:2310.07502

Munshi, D., Lee, H., Dvorkin, C., McEwen, J. D. (2022), *Weak lensing trispectrum and Kurt-spectra*, J. Cosmology Astropart. Phys., 2022(11), 020

Naab, T., Burkert, A. (2003), *Statistical Properties of Collisionless Equal- and Unequal-Mass Merger Remnants of Disk Galaxies*, ApJ, 597(2), 893

Naiman, J. P., Pillepich, A., Springel, V., Ramirez-Ruiz, E., Torrey, P., Vogelsberger, M., Pakmor, R., Nelson, D., Marinacci, F., Hernquist, L., Weinberger, R., Genel, S. (2018), *First results from the IllustrisTNG simulations: a tale of two elements - chemical evolution of magnesium and europium*, MNRAS, 477(1), 1206

Negroponte, J., White, S. D. M. (1983), *Simulations of mergers between disc-halo galaxies.*, MNRAS, 205, 1009

Nelson, D., Pillepich, A., Springel, V., Pakmor, R., Weinberger, R., Genel, S., Torrey, P., Vogelsberger, M., Marinacci, F., Hernquist, L. (2019), *First results from the TNG50 simulation: galactic outflows driven by supernovae and black hole feedback*, MNRAS, 490(3), 3234

Nelson, D., Pillepich, A., Springel, V., Weinberger, R., Hernquist, L., Pakmor, R., Genel, S., Torrey, P., Vogelsberger, M., Kauffmann, G., Marinacci, F., Naiman, J. (2018), *First results from the IllustrisTNG simulations: the galaxy colour bimodality*, MNRAS, 475(1), 624

Nelson, D., Springel, V., Pillepich, A., Rodriguez-Gomez, V., Torrey, P., Genel, S., Vogelsberger, M., Pakmor, R., Marinacci, F., Weinberger, R., Kelley, L., Lovell, M., Diemer, B., Hernquist, L. (2019), *The IllustrisTNG simulations: public data release*, Computational Astrophysics and Cosmology, 6(1), 2

Newton, I. (1704), *Opticks: or, A Treatise of the Reflections, Refractions, Inflexions and Colours of Light*, Sam. Smith and Benj. Walford, London, First edition

Okumura, T., Taruya, A. (2023), *First Constraints on Growth Rate from Redshift-Space Ellipticity Correlations of SDSS Galaxies at* $0.16 < z < 0.70$, arXiv e-prints, arXiv:2301.06273

Osato, K., Liu, J., Haiman, Z. (2021), *κTNG: effect of baryonic processes on weak lensing with IllustrisTNG simulations*, MNRAS, 502(4), 5593

Pakmor, R., et al. (2022), *The MillenniumTNG Project: The hydrodynamical full physics simulation and a first look at its galaxy clusters*, ArXiv e-prints

Parsi Mood, M., Firouzjaee, J. T., Mansouri, R. (2013), *Exact general relativistic lensing versus thin lens approximation: the crucial role of the void*, arXiv e-prints, arXiv:1304.5062

Paulin-Henriksson, S., Refregier, A., Amara, A. (2009), *Optimal point spread function modeling for weak lensing: complexity and sparsity*, A&A, 500(2), 647

Penzias, A. A., Wilson, R. W. (1965), *A Measurement of Excess Antenna Temperature at 4080 Mc/s.*, ApJ, 142, 419

Perlmutter, S., Aldering, G., Goldhaber, G., Knop, R. A., Nugent, P., Castro, P. G., Deustua, S., Fabbro, S., Goobar, A., Groom, D. E., Hook, I. M., Kim, A. G., Kim, M. Y., Lee, J. C., Nunes, N. J., Pain, R., Pennypacker, C. R., Quimby, R., Lidman, C., Ellis, R. S., Irwin, M., McMahon, R. G., Ruiz-Lapuente, P., Walton, N., Schaefer, B., Boyle, B. J., Filippenko, A. V., Matheson, T., Fruchter, A. S., Panagia, N., Newberg, H. J. M., Couch, W. J., Project, T. S. C. (1999), *Measurements of* Ω *and* Λ *from 42 High-Redshift Supernovae*, ApJ, 517(2), 565

Petri, A. (2016), *Mocking the weak lensing universe: The LensTools Python computing package*, Astronomy and Computing, 17, 73

Petri, A., Haiman, Z., May, M. (2017), *Validity of the Born approximation for beyond Gaussian weak lensing observables*, Phys. Rev. D, 95(12), 123503

Pillepich, A., et al. (2018), *Simulating Galaxy Formation with the IllustrisTNG Model*, MNRAS, 473(3), 4077

Pillepich, A., Nelson, D., Hernquist, L., Springel, V., Pakmor, R., Torrey, P., tng Weinberger, R., Genel, S., Naiman, J. P., Marinacci, F., Vogelsberger, M. (2018), *First results from the IllustrisTNG simulations: the stellar mass content of groups and clusters of galaxies*, MNRAS, 475(1), 648

Pillepich, A., Nelson, D., Springel, V., Pakmor, R., Torrey, P., Weinberger, R., Vogelsberger, M., Marinacci, F., Genel, S., van der Wel, A., Hernquist, L. (2019), *First results from the TNG50 simulation: the evolution of stellar and gaseous discs across cosmic time*, MNRAS, 490(3), 3196

Planck Collaboration (2016), *Planck 2015 results. XIII. Cosmological parameters*, A&A, 594, A13

Planck Collaboration, Aghanim, N., Akrami, Y., Ashdown, M., Aumont, J., Baccigalupi, C., Ballardini, M., Banday, A. J., Barreiro, R. B., Bartolo, N., Basak, S., Battye, R., Benabed, K., Bernard, J. P., Bersanelli, M., Bielewicz, P., Bock, J. J., Bond, J. R., Borrill, J., Bouchet, F. R., Boulanger, F., Bucher, M., Burigana, C., Butler, R. C., Calabrese, E., Cardoso, J. F., Carron, J., Challinor, A., Chiang, H. C., Chluba, J., Colombo, L. P. L., Combet, C., Contreras, D., Crill, B. P., Cuttaia, F., de Bernardis, P., de Zotti, G., Delabrouille, J., Delouis, J. M., Di Valentino, E., Diego, J. M., Doré, O., Douspis, M., Ducout, A., Dupac, X., Dusini, S., Efstathiou, G., Elsner, F., Enßlin, T. A., Eriksen, H. K., Fantaye, Y., Farhang, M., Fergusson, J., Fernandez-Cobos, R., Finelli, F., Forastieri, F., Frailis, M., Fraisse, A. A., Franceschi, E., Frolov, A., Galeotta, S., Galli, S., Ganga, K., Génova-Santos, R. T., Gerbino, M., Ghosh, T., González-Nuevo, J., Górski, K. M., Gratton, S., Gruppuso, A., Gudmundsson, J. E., Hamann,

J., Handley, W., Hansen, F. K., Herranz, D., Hildebrandt, S. R., Hivon, E., Huang, Z., Jaffe, A. H., Jones, W. C., Karakci, A., Keihänen, E., Keskitalo, R., Kiiveri, K., Kim, J., Kisner, T. S., Knox, L., Krachmalnicoff, N., Kunz, M., Kurki-Suonio, H., Lagache, G., Lamarre, J. M., Lasenby, A., Lattanzi, M., Lawrence, C. R., Le Jeune, M., Lemos, P., Lesgourgues, J., Levrier, F., Lewis, A., Liguori, M., Lilje, P. B., Lilley, M., Lindholm, V., López-Caniego, M., Lubin, P. M., Ma, Y. Z., Macías-Pérez, J. F., Maggio, G., Maino, D., Mandolesi, N., Mangilli, A., Marcos-Caballero, A., Maris, M., Martin, P. G., Martinelli, M., Martínez-González, E., Matarrese, S., Mauri, N., McEwen, J. D., Meinhold, P. R., Melchiorri, A., Mennella, A., Migliaccio, M., Millea, M., Mitra, S., Miville-Deschênes, M. A., Molinari, D., Montier, L., Morgante, G., Moss, A., Natoli, P., Nørgaard-Nielsen, H. U., Pagano, L., Paoletti, D., Partridge, B., Patanchon, G., Peiris, H. V., Perrotta, F., Pettorino, V., Piacentini, F., Polastri, L., Polenta, G., Puget, J. L., Rachen, J. P., Reinecke, M., Remazeilles, M., Renzi, A., Rocha, G., Rosset, C., Roudier, G., Rubiño-Martín, J. A., Ruiz-Granados, B., Salvati, L., Sandri, M., Savelainen, M., Scott, D., Shellard, E. P. S., Sirignano, C., Sirri, G., Spencer, L. D., Sunyaev, R., Suur-Uski, A. S., Tauber, J. A., Tavagnacco, D., Tenti, M., Toffolatti, L., Tomasi, M., Trombetti, T., Valenziano, L., Valiviita, J., Van Tent, B., Vibert, L., Vielva, P., Villa, F., Vittorio, N., Wandelt, B. D., Wehus, I. K., White, M., White, S. D. M., Zacchei, A., Zonca, A. (2020), *Planck 2018 results. VI. Cosmological parameters*, A&A, 641, A6

Prat, J., Bacon, D. (2025), *Weak Gravitational Lensing*

Press, W., Teukolsky, S., Vetterling, W., Flannery, B. (2007), *Numerical Recipes: The Art of Scientific Computing*, Cambridge University Press, third edition

Reinecke, M. (2020), *DUCC: Distinctly Useful Code Collection*, Astrophysics Source Code Library, record ascl:2008.023

Reinecke, M., Belkner, S., Carron, J. (2023), *Improved cosmic microwave background (de-)lensing using general spherical harmonic transforms*, A&A, 678, A165

Riess, A. G., Casertano, S., Yuan, W., Bowers, J. B., Macri, L., Zinn, J. C., Scolnic, D. (2021), *Cosmic Distances Calibrated to 1% Precision with Gaia EDR3 Parallaxes and Hubble Space Telescope Photometry of 75 Milky Way Cepheids Confirm Tension with* ΛCDM, ApJ, 908(1), L6

Riess, A. G., Casertano, S., Yuan, W., Macri, L. M., Scolnic, D. (2019), *Large Magellanic Cloud Cepheid Standards Provide a 1% Foundation for the Determination of the Hubble Constant and Stronger Evidence for Physics beyond* ΛCDM, ApJ, 876(1), 85

Riess, A. G., Filippenko, A. V., Challis, P., Clocchiatti, A., Diercks, A., Garnavich, P. M., Gilliland, R. L., Hogan, C. J., Jha, S., Kirshner, R. P., Leibundgut, B., Phillips, M. M., Reiss, D., Schmidt, B. P., Schommer, R. A., Smith, R. C., Spyromilio, J., Stubbs, C., Suntzeff, N. B., Tonry, J. (1998), *Observational Evidence from Supernovae for an Accelerating Universe and a Cosmological Constant*, AJ, 116(3), 1009

Riess, A. G., Yuan, W., Macri, L. M., Scolnic, D., Brout, D., Casertano, S., Jones, D. O., Murakami, Y., Anand, G. S., Breuval, L., Brink, T. G., Filippenko, A. V., Hoffmann, S., Jha, S. W., D'arcy Kenworthy, W., Mackenty, J., Stahl, B. E., Zheng, W. (2022), *A Comprehensive Measurement of the Local Value of the Hubble Constant with 1 km s^{-1} Mpc^{-1} Uncertainty from the Hubble Space Telescope and the SH0ES Team*, ApJ, 934(1), L7

Rizzato, M., Benabed, K., Bernardeau, F., Lacasa, F. (2019), *Tomographic weak lensing bispectrum: a thorough analysis towards the next generation of galaxy surveys*, MNRAS, 490(4), 4688

Rowe, B. (2010), *Improving PSF modelling for weak gravitational lensing using new methods in model selection*, MNRAS, 404(1), 350

Rubin, V. C., Ford, Jr., W. K., Thonnard, N. (1980), *Rotational properties of 21 SC galaxies with a large range of luminosities and radii, from NGC 4605 (R=4kpc) to UGC 2885 (R=122kpc).*, ApJ, 238, 471

Samuroff, S., Mandelbaum, R., Blazek, J. (2021), *Advances in constraining intrinsic alignment models with hydrodynamic simulations*, MNRAS, 508(1), 637

Samuroff, S., Mandelbaum, R., Blazek, J., Campos, A., MacCrann, N., Zacharegkas, G., Amon, A., Prat, J., Singh, S., Elvin-Poole, J., Ross, A. J., Alarcon, A., Baxter, E., Bechtol, K., Becker, M. R., Bernstein, G. M., Rosell, A. C., Kind, M. C., Cawthon, R., Chang, C., Chen, R., Choi, A., Crocce, M., Davis, C., DeRose, J., Dodelson, S., Doux, C., Drlica-Wagner, A., Eckert, K., Everett, S., Ferté, A., Gatti, M., Giannini, G., Gruen, D., Gruendl, R. A., Harrison, I., Herner, K., Huff, E. M., Jarvis, M., Kuropatkin, N., Leget, P. F., Lemos, P., McCullough, J., Myles, J., Navarro-Alsina, A., Pandey, S., Porredon, A., Raveri, M., Rodriguez-Monroy, M., Rollins, R. P., Roodman, A., Rossi, G., Rykoff, E. S., Sánchez, C., Secco, L. F., Sevilla-Noarbe, I., Sheldon, E., Shin, T., Troxel, M. A., Tutusaus, I., Weaverdyck, N., Yanny, B., Yin, B., Zhang, Y., Zuntz, J., Aguena, M., Alves, O., Annis, J., Bacon, D., Bertin, E., Bocquet, S., Brooks, D., Burke, D. L., Carretero, J., Costanzi, M., da Costa, L. N., Pereira, M. E. S., De Vicente, J., Desai, S., Diehl, H. T., Dietrich, J. P., Doel, P., Ferrero, I., Flaugher, B., Frieman, J., García-Bellido, J., Hinton, S. R., Hollowood, D. L., Honscheid, K., James, D. J., Kuehn, K., Lahav, O., Marshall, J. L., Melchior, P., Mena-Fernández, J., Menanteau, F., Miquel, R., Newman, J., Palmese, A., Pieres, A., Malagón, A. A. P., Sanchez, E., Scarpine, V., Smith, M., Suchyta, E., Swanson, M. E. C., Tarle, G., To, C., DES Collaboration (2023), *The Dark Energy Survey Year 3 and eBOSS: constraining galaxy intrinsic alignments across luminosity and colour space*, MNRAS, 524(2), 2195

Schmalzing, J., Gorski, K. M. (1998), *Minkowski functionals used in the morphological analysis of cosmic microwave background anisotropy maps*, MNRAS, 297(2), 355

Schmidt, F., Chisari, N. E., Dvorkin, C. (2015), *Imprint of inflation on galaxy shape correlations*, J. Cosmology Astropart. Phys., 2015(10), 032

Schmidt, F., Jeong, D. (2012a), *Cosmic rulers*, Phys. Rev. D, 86(8), 083527

Schmidt, F., Jeong, D. (2012b), *Large-scale structure with gravitational waves. II. Shear*, Phys. Rev. D, 86(8), 083513

Schneider, M. D., Bridle, S. (2010), *A halo model for intrinsic alignments of galaxy ellipticities*, MNRAS, 402(4), 2127

Schneider, P., Ehlers, J., Falco, E. E. (1992), *Gravitational Lenses*, Springer New York

Schneider, P., Er, X. (2008), *Weak lensing goes bananas: what flexion really measures*, A&A, 485(2), 363

Schneider, P., van Waerbeke, L., Kilbinger, M., Mellier, Y. (2002), *Analysis of two-point statistics of cosmic shear. I. Estimators and covariances*, A&A, 396, 1

Schutt, T., Jarvis, M., Roodman, A., Amon, A., Becker, M. R., Gruendl, R. A., Yamamoto, M., Bechtol, K., Bernstein, G. M., Gatti, M., Rykoff, E. S., Sheldon, E., Troxel, M. A., Abbott, T. M. C., Aguena, M., Andrade-Oliveira, F., Brooks, D., Rosell, A. C., Carretero, J., Chang, C., Choi, A., Crocce, M., da Costa, L. N., Davis, T. M., De Vicente, J., Desai, S., Diehl, H. T., Doel, P., Ferté, A., Frieman, J., García-Bellido, J., Gaztanaga, E., Gruen, D., Gutierrez, G., Hinton, S. R., Hollowood, D. L., Honscheid, K., Kuehn, K., Lahav, O., Lee, S., Lima, M., Marshall, J. L., Mena-Fernández, J., Miquel, R., Mohr, J. J., Myles, J., Ogando, R. L. C., Pieres, A., Malagón, A. A. P., Porredon, A., Samuroff, S., Sanchez, E., Cid, D. S., Sevilla-Noarbe, I., Smith, M., Suchyta, E., Tarle, G., Vikram, V., Walker, A. R., Weaverdyck, N. (2025), *Dark Energy Survey Year 6 Results: Point-Spread Function Modeling*, The Open Journal of Astrophysics, 8, 26

Semboloni, E., Hoekstra, H., Schaye, J., van Daalen, M. P., McCarthy, I. G. (2011), *Quantifying the effect of baryon physics on weak lensing tomography*, MNRAS, 417(3), 2020

Shi, J., Kurita, T., Takada, M., Osato, K., Kobayashi, Y., Nishimichi, T. (2021), *Power spectrum of intrinsic alignments of galaxies in IllustrisTNG*, J. Cosmology Astropart. Phys., 2021(3), 030

Singh, S., Mandelbaum, R., More, S. (2015), *Intrinsic alignments of SDSS-III BOSS LOWZ sample galaxies*, MNRAS, 450(2), 2195

Soucail, G., Mellier, Y., Fort, B., Hammer, F., Mathez, G. (1987), *Further data on the blue ring-like structure in A 370.*, A&A, 184, L7

Springel, V., Pakmor, R., Pillepich, A., Weinberger, R., Nelson, D., Hernquist, L., Vogelsberger, M., Genel, S., Torrey, P., Marinacci, F., Naiman, J. (2018), *First results from the IllustrisTNG simulations: matter and galaxy clustering*, MNRAS, 475(1), 676

Springel, V., Pakmor, R., Zier, O., Reinecke, M. (2021), *Simulating cosmic structure formation with the gadget-4 code*, MNRAS, 506(2), 2871–2949

Springel, V., White, S. D. M., Colberg, J. M., Couchman, H. M. P., Efstathiou, G. P., Frenk, C. S., Jenkins, A. R., Pearce, F. R., Nelson, A. H., Peacock, J. A., Thomas, P. A. (1998), *Genus statistics of the Virgo N-body simulations and the 1.2-Jy redshift survey*, MNRAS, 298(4), 1169

Springel, V., White, S. D. M., Jenkins, A., Frenk, C. S., Yoshida, N., Gao, L., Navarro, J., Thacker, R., Croton, D., Helly, J., Peacock, J. A., Cole, S., Thomas, P., Couchman, H., Evrard, A., Colberg, J., Pearce, F. (2005), *Simulations of the formation, evolution and clustering of galaxies and quasars*, Nature, 435(7042), 629

Sugiyama, S., Miyatake, H., More, S., Li, X., Shirasaki, M., Takada, M., Kobayashi, Y., Takahashi, R., Nishimichi, T., Nishizawa, A. J., Rau, M. M., Zhang, T., Dalal, R., Mandelbaum, R., Strauss, M. A., Hamana, T., Oguri, M., Osato, K., Kannawadi, A., Hsieh, B.-C., Luo, W., Armstrong, R., Bosch, J., Komiyama, Y., Lupton, R. H., Lust, N. B., Miyazaki, S., Murayama, H., Okura, Y., Price, P. A., Tait, P. J., Tanaka, M., Wang, S.-Y. (2023), *Hyper Suprime-Cam Year 3 results: Cosmology from galaxy clustering and weak lensing with HSC and SDSS using the minimal bias model*, Phys. Rev. D, 108(12), 123521

Swinbank, R., Purser, R. J. (2006), *Fibonacci grids: A novel approach to global modelling*, Quarterly Journal of the Royal Meteorological Society, 132

Takada, M., Jain, B. (2003), *Three-point correlations in weak lensing surveys: model predictions and applications*, MNRAS, 344(3), 857

Takahashi, R., Hamana, T., Shirasaki, M., Namikawa, T., Nishimichi, T., Osato, K., Shiroyama, K. (2017), *Full-sky Gravitational Lensing Simulation for Large-area Galaxy Surveys and Cosmic Microwave Background Experiments*, ApJ, 850(1), 24

Takahashi, R., Sato, M., Nishimichi, T., Taruya, A., Oguri, M. (2012a), *Revising the Halofit Model for the Nonlinear Matter Power Spectrum*, ApJ, 761, 152

Takahashi, R., Sato, M., Nishimichi, T., Taruya, A., Oguri, M. (2012b), *Revising the Halofit Model for the Nonlinear Matter Power Spectrum*, ApJ, 761, 152

Tanaka, M., Coupon, J., Hsieh, B.-C., Mineo, S., Nishizawa, A. J., Speagle, J., Furusawa, H., Miyazaki, S., Murayama, H. (2018), *Photometric redshifts for Hyper Suprime-Cam Subaru Strategic Program Data Release 1*, PASJ, 70, S9

Taruya, A., Okumura, T. (2020), *Improving Geometric and Dynamical Constraints on Cosmology with Intrinsic Alignments of Galaxies*, The Astrophysical Journal, 891(2), L42

Tenneti, A., Singh, S., Mandelbaum, R., di Matteo, T., Feng, Y., Khandai, N. (2015), *Intrinsic alignments of galaxies in the MassiveBlack-II simulation: analysis of two-point statistics*, MNRAS, 448(4), 3522

Tisserand, P., Le Guillou, L., Afonso, C., Albert, J. N., Andersen, J., Ansari, R., Aubourg, É., Bareyre, P., Beaulieu, J. P., Charlot, X., Coutures, C., Ferlet, R., Fouqué, P., Glicenstein, J. F., Goldman, B., Gould, A., Graff, D., Gros, M., Haissinski, J., Hamadache, C., de Kat, J., Lasserre, T., Lesquoy, É., Loup, C., Magneville, C., Marquette, J. B., Maurice, É., Maury, A., Milsztajn, A., Moniez, M., Palanque-Delabrouille, N., Perdereau, O., Rahal, Y. R., Rich, J., Spiro, M., Vidal-Madjar, A., Vigroux, L., Zylberajch, S., EROS-2 Collaboration (2007), *Limits on the Macho content of the Galactic Halo from the EROS-2 Survey of the Magellanic Clouds*, A&A, 469(2), 387

Troxel, M. A., Ishak, M. (2012), *Self-calibration technique for three-point intrinsic alignment correlations in weak lensing surveys*, MNRAS, 419(2), 1804

Troxel, M. A., Ishak, M. (2015), *The intrinsic alignment of galaxies and its impact on weak gravitational lensing in an era of precision cosmology*, Phys. Rep., 558, 1

Tsaprazi, E., Nguyen, N.-M., Jasche, J., Schmidt, F., Lavaux, G. (2022), *Field-level inference of galaxy intrinsic alignment from the SDSS-III BOSS survey*, J. Cosmology Astropart. Phys., 2022(8), 003

Tyson, J. A., Valdes, F., Wenk, R. A. (1990), *Detection of Systematic Gravitational Lens Galaxy Image Alignments: Mapping Dark Matter in Galaxy Clusters*, ApJ, 349, L1

Valageas, P. (2000), *Statistical properties of the convergence due to weak gravitational lensing by non-linear structures*, A&A, 356, 771

Valdes, F., Tyson, J. A., Jarvis, J. F. (1983), *Alignment of faint galaxy images : cosmological distortion and rotation.*, ApJ, 271, 431

Van Waerbeke, L., Mellier, Y., Erben, T., Cuillandre, J. C., Bernardeau, F., Maoli, R., Bertin, E., McCracken, H. J., Le Fèvre, O., Fort, B., Dantel-Fort, M., Jain, B., Schneider, P. (2000), *Detection of correlated galaxy ellipticities from CFHT data: first evidence for gravitational lensing by large-scale structures*, A&A, 358, 30

Vanderriest, C., Schneider, J., Herpe, G., Chevreton, M., Moles, M., Wlerick, G. (1989), *The value of the time delay delta T (A,B) for the 'double' quasar 0957+561 from optical photometric monitoring.*, A&A, 215, 1

Varshalovich, D. A., Moskalev, A. N., Khersonskii, V. K. (1988), *Quantum Theory of Angular Momentum*, World Scientific, Singapore

Velliscig, M., Cacciato, M., Schaye, J., Crain, R. A., Bower, R. G., van Daalen, M. P., Dalla Vecchia, C., Frenk, C. S., Furlong, M., McCarthy, I. G., Schaller, M., Theuns, T.

(2015a), *The alignment and shape of dark matter, stellar, and hot gas distributions in the EAGLE and cosmo-OWLS simulations*, MNRAS, 453(1), 721

Velliscig, M., Cacciato, M., Schaye, J., Hoekstra, H., Bower, R. G., Crain, R. A., van Daalen, M. P., Furlong, M., McCarthy, I. G., Schaller, M., Theuns, T. (2015b), *Intrinsic alignments of galaxies in the EAGLE and cosmo-OWLS simulations*, MNRAS, 454(3), 3328

Vlah, Z., Chisari, N. E., Schmidt, F. (2020), *An EFT description of galaxy intrinsic alignments*, J. Cosmology Astropart. Phys., 2020(1), 025

Vlah, Z., Chisari, N. E., Schmidt, F. (2021), *Galaxy shape statistics in the effective field theory*, J. Cosmology Astropart. Phys., 2021(5), 061

Walsh, D., Carswell, R. F., Weymann, R. J. (1979), *0957+561 A, B: twin quasistellar objects or gravitational lens?*, Nature, 279, 381

Weinberg, S. (1989), *The cosmological constant problem*, Reviews of Modern Physics, 61(1), 1

Weinberger, R., Springel, V., Hernquist, L., Pillepich, A., Marinacci, F., Pakmor, R., Nelson, D., Genel, S., Vogelsberger, M., Naiman, J., Torrey, P. (2017), *Simulating galaxy formation with black hole driven thermal and kinetic feedback*, MNRAS, 465(3), 3291

Weymann, R. J., Latham, D., Angel, J. R. P., Green, R. F., Liebert, J. W., Turnshek, D. A., Turnshek, D. E., Tyson, J. A. (1980), *The triple QSO PG1115 + 08: another probable gravitational lens*, Nature, 285(5767), 641

White, M. (2004), *Baryons and weak lensing power spectra*, Astroparticle Physics, 22(2), 211

White, M., van Waerbeke, L., Mackey, J. (2002), *Completeness in Weak-Lensing Searches for Clusters*, ApJ, 575(2), 640

Wong, Y. Y. (2011), *Neutrino Mass in Cosmology: Status and Prospects*, Annual Review of Nuclear and Particle Science, 61(1), 69

Wright, A. H., Kuijken, K., Hildebrandt, H., Radovich, M., Bilicki, M., Dvornik, A., Getman, F., Heymans, C., Hoekstra, H., Li, S.-S., Miller, L., Napolitano, N. R., Xia, Q., Asgari, M., Brescia, M., Buddelmeijer, H., Burger, P., Castignani, G., Cavuoti, S., de Jong, J., Edge, A., Giblin, B., Giocoli, C., Harnois-Déraps, J., Jalan, P., Joachimi, B., John William, A., Joudaki, S., Kannawadi, A., Kaur, G., La Barbera, F., Linke, L., Mahony, C., Maturi, M., Moscardini, L., Nakoneczny, S. J., Paolillo, M., Porth, L., Puddu, E., Reischke, R., Schneider, P., Sereno, M., Shan, H., Sifón, C., Stölzner, B., Tröster, T., Valentijn, E., van den Busch, J. L., Verdoes Kleijn, G., Wittje, A., Yan, Z., Yao, J., Yoon, M., Zhang, Y.-H. (2024), *The fifth data release of the Kilo Degree Survey:*

Multi-epoch optical/NIR imaging covering wide and legacy-calibration fields, A&A, 686, A170

Xu, K., Jing, Y. P., Zhao, G.-B., Cuesta, A. J. (2023), *Evidence for baryon acoustic oscillations from galaxy-ellipticity correlations.*, Nature Astronomy, 7, 1259

Yang, X., Kratochvil, J. M., Huffenberger, K., Haiman, Z., May, M. (2013), *Baryon impact on weak lensing peaks and power spectrum: Low-bias statistics and self-calibration in future surveys*, Phys. Rev. D, 87(2), 023511

Yang, X., Kratochvil, J. M., Wang, S., Lim, E. A., Haiman, Z., May, M. (2011), *Cosmological information in weak lensing peaks*, Physical Review D, 84(4)

Zhang, J., Wuyts, S., Witten, C., Avery, C. R., Hao, L., Sharma, R., Shen, J., Toshikawa, J., Villforth, C. (2022), *3D intrinsic shapes of quiescent galaxies in observations and simulations*, MNRAS, 513(4), 4814

Zhang, P. (2010), *A proposal on the galaxy intrinsic alignment self-calibration in weak lensing surveys*, MNRAS, 406(1), L95

Zhang, T., Rau, M. M., Mandelbaum, R., Li, X., Moews, B. (2023), *Photometric redshift uncertainties in weak gravitational lensing shear analysis: models and marginalization*, MNRAS, 518(1), 709

Zhou, A. J., Li, Y., Dodelson, S., Mandelbaum, R., Zhang, Y., Li, X., Fabbian, G. (2024), *A Hamiltonian, post-Born, three-dimensional, on-the-fly ray tracing algorithm for gravitational lensing*

Zjupa, J., Schäfer, B. M., Hahn, O. (2022), *Intrinsic alignments in IllustrisTNG and their implications for weak lensing: Tidal shearing and tidal torquing mechanisms put to the test*, MNRAS, 514(2), 2049

Zorrilla Matilla, J. M., Waterval, S., Haiman, Z. (2020), *Optimizing Simulation Parameters for Weak Lensing Analyses Involving Non-Gaussian Observables*, AJ, 159(6), 284

Zuntz, J., Kacprzak, T., Voigt, L., Hirsch, M., Rowe, B., Bridle, S. (2014), *IM3SHAPE: Maximum likelihood galaxy shear measurement code for cosmic gravitational lensing*, Astrophysics Source Code Library, record ascl:1409.013

Zwicky, F. (1933), *Die Rotverschiebung von extragalaktischen Nebeln*, Helvetica Physica Acta, 6, 110

Zwicky, F. (1937a), *Nebulae as Gravitational Lenses*, Physical Review, 51(4), 290

Zwicky, F. (1937b), *On the Probability of Detecting Nebulae Which Act as Gravitational Lenses*, Physical Review, 51(8), 679

Acknowledgements

Questo dottorato mi ha fatto crescere molto, probabilmente è stata l'esperienza che più mi ha trasformato in un adulto. E durante questa crescita, questo cambiamento, questa maturazione, sia scientifica che personale, sono state presenti, e in più occasioni fondamentali, delle persone speciali, che qui colgo l'occasione per ringraziare.

Desidero esprimere innanzitutto un sentito e profondo ringraziamento al Prof. Volker Springel. Oltre a essere un illustre astrofisico, di cui ho avuto il privilegio di essere allievo, si è rivelato fin da subito una persona straordinaria: paziente, sensibile, sempre disposto ad ascoltare, insegnare, e guidare con grande attenzione e dedizione. A lui va la mia più sincera gratitudine.

Un grande ringraziamento va al mio collaboratore Chris. Anche lui mi ha insegnato tanto, sia nell'ambito dell'astrofisica, sia nell'affrontare il dottorato con il giusto equilibrio tra ambizione e svago. In questi anni Chris è diventato uno dei miei amici piu' cari, e lo ringrazio per tutte le risate, le feste, e le avventure che abbiamo collezionato.

Voglio ringraziare i tanti ricercatori con cui ho avuto il piacere e la fortuna di collaborare, tra cui: Toshiki Kurita, Martin Reinecke, Alessandro Greco, Ana Maria Delgado, Enrico Garaldi, Simon White, Lars Hernquist, Ken Osato, e Naoki Yoshida. Grazie a tutti voi, e a tutti gli altri che mi scuso per aver dimenticato. Ringrazio anche le segretarie di MPA, le quali sono state di prezioso supporto per me e per tutti gli altri studenti.

Un ringraziamento unico va alla mia mamma Silvana, a cui questa tesi ho scelto di dedicare. Tu che non hai mai, neanche per un istante, smesso di credere in me, e che hai sempre saputo, anche ben prima che lo sapessi io, che sarei diventato un astrofisico. Non sara' mai abbastanza la gratitudine per averci cresciuto, sia me che Anna, all'insegna del pensiero critico, e del rispetto e dell'amore per l'arte, per la scienza, e per la cultura.

Un altro ringraziamento speciale va a mio papà Salvatore, per gli amici Totò. Grazie per avere insegnato a me e Anna a non arrenderci di fronte alle difficoltà. Grazie per avermi chiamato (quasi) ogni sera in questi quattro anni, senza mai scordarti di infondere sia a me che a Soumya tanta energia e coraggio. La tua creatività, la tua personalità, e la tua filosofia di vita mi hanno inequivocabilmente ispirato e sono parte integrante della persona, e dello "scienziato", che sono oggi.

Ringrazio di cuore mia sorella Anna, che c'è sempre stata e sempre ci sarà. Grazie per avermi aiutato nel momento del bisogno, per essere venuta qui a Monaco, non solo per bere tanta birra assieme, ma anche e soprattutto per esserti presa cura di me dopo l'operazione. Sono tanto fiero di te, che in parallelo a questo mio traguardo ne hai appena raggiunto un

altro, altrettanto importante. E adesso che tante strade ci si aprono davanti, sono sicuro che entrambi sceglieremo quella giusta.

Un grazie pieno di dolcezza va a mio fratello Flavio. Sei nato poco prima che cominciassi il dottorato, e adesso che sono giunto alla fine, tu sei già un piccolo ometto, appassionato di biologia, sia marina che terrestre. Grazie per avere riempito di tenerezza e gioia tantissime giornate. Un grazie anche alla sua mamma Roberta e alla zia Sabrina, che mi hanno supportato con tanto affetto.

Ringrazio di cuore la nonna Maria e la zia Rosetta. Anche loro hanno ispirato e insegnato tanto sia a me, che al resto della famiglia. Grazie per aver gioito dei nostri traguardi come fossero i vostri, per averci dato la carica e tutto l'affetto di cui i nipoti hanno bisogno. Grazie ai miei splendidi cugini-fratelli Eleonora, Elisa, e Giorgio. Grazie a voi per tutto il supporto, l' affetto, e per avermi regalato tanta allegria e risate, nei momenti in cui ne avevo bisogno. Altrettante grazie vanno a cugino Angelo, cugina Stefania, e alla piccolissima Selene.

Un grazie dal profondo del mio cuore va al nonno Stefano, alla zia Gabriella e allo zio Mario. Che non hanno mai smesso di brillare, di darmi la carica, di ispirarmi, di motivarmi e di farmi puntare alle stelle, anche da lassù. Grazie a tutte le altre stelle nel cielo compresi Guiduccio e lo zio Marcello. Voglio dedicare anche a voi questo traguardo.

Voglio ringraziare i miei amici siciliani. Grazie innanzitutto a Sergio, per aver reso indimenticabile e pieno di gioia e divertimento ogni mio ritorno in Sicilia. Tornare a casa significa anche tornare da te, e non ci sono parole che bastino per esprimere il mio affetto e la mia gratitudine. Un ringraziamento fraterno va alla mia amica Carolina. Grazie per tutte le chiacchierate al telefono, per avermi fatto sfogare, per avermi pazientemente ascoltato, tenuto compagnia, e dato ottimi consigli. Grazie ai miei amici storici Antonio e Alex, anche se distanti geograficamente, in tutti questi anni siete stati fonte inesauribile di risate, affetto, svago, e goliardia. Grazie a Salvo M. per i tanti e importanti caffè che abbiamo preso. Mi hai aiutato a sviluppare una visione più critica del mondo e in più occasioni a prendere la scelta giusta. Grazie anche agli splendidi Matteo M., Alessandro F., Salvo P., Alessandro C., e Giuseppe.

Voglio ringraziare tutti i Maestri che mi hanno insegnato le scienze, permettendomi di arrivare fino a qui. In particolare, in ordine cronologico: la Maestra Paola, il Prof. Carollo, la Prof. Manicastri, il Prof. Grimaudo, e, ultimo ma non meno importante, il Prof. Marco Baldi, che ringrazio particolarmente per avermi incoraggiato a fare domanda per il dottorato e per avermi fornito le competenze necessarie ad accedere a questo progetto.

Voglio ringraziare i miei amici "bolognesi". Grazie ad Alessandro Ciocchetti, per avere contribuito sostanzialmente alla mia crescita personale e culturale. Sei un fratello per me, e lo sarai per sempre. Grazie anche a te per la pazienza con cui mi hai ascoltato e dato consigli nei momenti critici. Grazie per non avermi mai fatto giacere sugli allori e avermi sempre spronato a migliorarmi. Grazie anche a Giulia e a Paki. Un ringraziamento molto importante va a Nicolò. Averti avuto come compagno di banco all'università è stata forse la più grande fortuna in ambito scientifico che abbia avuto. Se ho portato a termine questo traguardo è senza dubbio anche grazie a tutte le preziose e stimolanti conversazioni, scientifiche e non, che abbiamo avuto. Continui sempre a ispirarmi. Ringraziamenti "giganti"

vanno a Haydée e Leo, per aver continuato ad accogliermi con affetto tutte le volte che sono tornato a Bologna. Se quest'ultima è per me come una seconda casa, lo devo soprattutto a voi due. Grazie anche ad Alina, Saverio, e Maria Caterina.

Ringrazio gli amici, vecchi e nuovi, che hanno fatto parte della mia vita qui a Monaco. Grazie a Nicola, per gli amici Toska, che considero come un fratello maggiore. Sei stato fondamentale durante questo percorso. Mi hai aiutato più di quanto immagini a superare le difficoltà, a crescere, ad affrontare la vita con leggerezza. Grazie per tutta la musica che abbiamo suonato, e per tutta la spensieratezza che mi hai regalato. Grazie a Matteo E., che, oltre ad essere un amico fedele e un collega brillante, mi ha assistito nel momento del bisogno. Ti sarò sempre grato, e sono lieto che siamo riusciti a realizzare insieme quello che era il nostro sogno già da bambini. Grazie a James, Sophia, Emre, Riccardo, Francesco, Antonia, Bob, e Jed. Avere distanti alcuni di voi in questo ultimo anno di dottorato mi ha fatto capire e apprezzare ancor di più quanto siate stati fondamentali, disponibili e preziosi, sia per me che per Soumya, nella nostra vita a Monaco.

Ringrazio tutti i meravigliosi amici e colleghi con i quali ho trascorso il mio tempo a MPA. In particolare ringrazio Matteo G. e Hitesh per le tantissime partite a biliardino e le altrettante risate. Grazie a Miha, per avermi aperto la porta di MPA, ma anche la porta della common room, dove stavamo già bevendo una birra a pochi minuti dal mio primo ingresso. Ringrazio i miei compagni di ufficio Mrinal, Beatriz e Simon, per aver reso piacevole la quotidianità nel nostro ufficio, condividendo gioie e dispiaceri. Grazie anche a tutti gli altri, non meno importanti, tra cui Raph, Eve, Lazaros, Stavroula, Benedetta, Laura, Anna G., Anshuman, Sam, Abinaya, Aniket, Daniela, David, Zsofi, Julian, Arghyadeep, Gesa, Silvia, Teresa, Christian, e tutti quelli che sto dimenticando.

Dulcis in fundo, immensa gratitudine va a Soumya. Sei il tesoro piu' prezioso che abbia trovato durante questo percorso. Sin dall'inizio non hai esitato a starmi accanto e supportarmi, nonostante le mie precarie condizioni di salute, e nonostante il tuo dottorato, altrettanto impegnativo, da portare avanti. Questi anni ci hanno unito, ci hanno fatto crescere entrambi, tanto, e insieme. Un grazie anche ai tuoi genitori Chitra auntie e Shreeram uncle, Tati, a tua sorella Kashmira, e a tuo cognato Varun, che mi hanno fatto sentire amato e accolto come a casa, anche quando ero dall'altra parte del mondo. Soumya, grazie per la carica esplosiva di energia, felicità, e monelleria che sprigioni ogni giorno, spero non finisca mai.